# CRYSTALLIZATION OF ALUMINUM TRIHYDROXIDE: EVOLUTION OF THE MORPHOLOGY

by

Rémy Dumortier

A thesis submitted to the Faculty of Graduate
Studies and Research in partial fulfillment
of the requirements for the degree of
Master of Engineering

Department of Chemical Engineering
McGill University
Montreal, Canada

0-612-70227-8

# ABSTRACT

The bauxite, a mineral rich ore, is an important source of metallic aluminum in industry. The Bayer process, developed in 1888, involves the extraction of alumina ($Al_2O_3$) from bauxite. One of the key stage of Bayer process is the crystallization of aluminum trihydroxide ($Al(OH)_3$), an intermediate product from which alumina is obtained by dehydration. Crystallization behavior and the morphology of aluminum trihydroxide depend strongly on the reactor temperature, the supersaturation defined by the concentration ratio of soluble $[Al_2O_3]/[Na_2O]$, noted as A/C ratio, and the presence of impurities. This crystallization behavior of aluminum trihydroxide was examined at various temperatures, initial concentration ratios of $[Al_2O_3]/[Na_2O]$ and concentrations of titanium oxide and ferric oxide as impurities. The X-ray diffraction analysis showed that only gibbsite, a polymorph of $Al(OH)_3$, was produced at the end of all the experiments. An increase in the temperature, as well as an increase of the initial A/C ratio, resulted in an augmentation of the slurry density and the particle size distribution. The Scanning Electron Microscope (SEM) images of aluminum trihydroxide crystals revealed that the presence of titanium oxide favored the production of the small single crystals minimizing agglomeration. In the case of ferric oxide, the agglomerates were formed but showed a decrease of the average diameter as compared with the crystals formed without any impurities. Zeta-potential and settling velocity of aluminum trihydroxide in the presence and absence of impurities were also measured.

# RESUME

Le bauxite, un riche minerai, est une source importante d'aluminium dans l'industrie. Le procédé Bayer, développé en 1888, permet d'extraire l'alumina du bauxite. Une des étapes importantes de ce procédé est la cristallisation du trihydroxide d'aluminium ($Al(OH)_3$), un produit intermédiaire à partir duquel on produit l'alumina par déshydratation. L'évolution de la cristallisation et de la morphologie d'$Al(OH)_3$ dependent fortement de la température du réacteur, la supersaturation définie par le rapport des concentrations soluble de [$Al_2O_3$] et de [$Na_2O$], noté A/C, et de la présence d'impuretés dans la solution. Dans ce mémoire, l'évolution de la cristallisation d' $Al(OH)_3$ a été étudiée à différentes températures, différents rapports des concentrations initiales de [$Al_2O_3$] soluble et [$Na_2O$] soluble et différentes concentrations en impuretés (oxide de titanium et oxide de fer). L'analyse par diffraction des rayons X a montré que seul le gibbsite, un polymorphe de $Al(OH)_3$, a été produit à la fin de toutes les expériences réalisées. Une élévation de la température, de même qu'une augmentation du rapport des concentrations initiales A/C, ont conduit à une augmentation de la densité des particules dans la solution et du volume moyen des cristaux. Les images des cristaux d'$Al(OH)_3$ prises avec un microscope à balayage électronique ont révélé que la présence d'oxide de titanium minimise l'agglomération et favorise la formation de simples cristaux. Dans le cas de l'oxide de fer, les cristaux d'$Al(OH)_3$ aggloméraient mais le diamètre moyen diminuait comparé au cas sans impuretés. Le potentiel zêta et la vitesse de sédimentation d'$Al(OH)_3$, en présence et absence d'impuretés, ont été aussi mesurés.

# ACKNOWLEDGEMENTS

I would like to take this opportunity to express my sincere gratitude to my research supervisor, Professor D. Berk for his guidance and advice during the course of this project. I would like to thank him furthermore for his financial support that permitted me to achieve this master.

I wish to thank also the following people who contributed to the work presented in this thesis:

- To Mr. L. Cusmich, Mr. F. Caporuscio, Mr A. Gagnon and the personnel of the Machine shop for their professional response and work.
- To my fellow students Younok, Isabelle, Fujing and all my friends from Chemical Engineering for their assistance and for making Montreal an enjoyable place to live.
- To Gail Risto from Alcan International Ltd. and Kaiser Aluminum & chemical Corporation for supplying some $Al(OH)_3$ and information on their plant.
- To the department of Chemical Engineering of McGill University for the financial support received in the form of a teaching position. I profit of the occasion to thank the Professor M. Weber with whom I had a lot of pleasure to work.

Finally I would like to express my deepest thankfulness to my parents and the rest of my family for their support and their love. They always encourage me to go over the difficulties and help me in my desire of knowledge even if I had to live far away, in another country.

# DEDICATION

To my parents…..

# TABLE OF CONTENTS

# LIST OF THE FIGURES

# LIST OF THE TABLES

# NOMENCLATURE

A: Alumina concentration, expressed as g/L $Al_2O_3$, abbreviated as g/L A.

C: Caustic concentration (sodium hydroxide plus sodium aluminate), expressed as g/L $Na_2O$, abbreviated g/L C.

A/C: Alumina / Caustic ratio, using above units.

Alumina supersaturation: Concentration above equilibrium solubility, expressed as A/C ratio.

R: Alumina/ Caustic ratio at any time, using above unit.

$R_{eq}$: Equilibrium Alumina/ Caustic ratio, using above unit.

S: Supersaturation of the solution corresponding to the ratio $R/R_{eq}$.

T: Temperature in °C.

$\sigma$: Specific surface free energy. It represents the work spent to create reversibly and isothermally a unit area of a new surface.

CSD: Crystal Size Distribution.

AA: Atomic Absorption.

Ppm: Part per million.

LOI: Weight loss due to heating from 110 to 1100°C.

V/V: Volume / Volume.

2-D nucleus: Two- dimensional nucleus.

# Chapter 1

# INTRODUCTION

Aluminum is the third most commonly found element in the earth's crust, which consists of 9% aluminum. It is found prevalently in rocks and minerals such as clay where it is combined with the oxides of silicon. The properties of metallic aluminum depend to some extent on its purity. This may vary from the ordinary aluminum at 99.2% purity to super-purity aluminum at 99.99% or higher purity (Varley, 1970). High purity aluminum is soft and lacks strength, but its alloys, containing a small amount of other elements have high strength to weight ratios. Depending on their properties, aluminum compounds have been used in various applications for over 4000 years (Evans, 1996).

The characteristics of aluminum are well known. Its main properties are its low-density (2700 kg/m$^3$), good reflectivity, and electrical and thermal conductivity. It is also protected from the atmospheric corrosion by a thin oxide film resulting from the instantaneous reaction of aluminum with oxygen (Varley, 1970). Due to its desirable physical, chemical, and metallurgical properties, aluminum is the most widely used non-ferrous metal. For example, due to its high conductivity, aluminum is used in electrical transmission lines, and, due to its low density, in aeronautics along with other light metals.

Aluminum does not occur in the metallic state because of its strong affinity to oxygen. Thus, bauxite, a mineral rich in aluminum oxide (alumina), is the most important source of the aluminum metal. The Bayer process, which was discovered in 1888 by the

German scientist K. Bayer, has been used to extract and purify the alumina ($Al_2O_3$) from bauxite. Any changes in the process conditions result in alumina having different physical and chemical properties. One of the critical stages in the Bayer process is the crystallization of aluminum trihydroxide, $Al(OH)_3$, which is an intermediate product. Aluminum trihydroxide is then converted to alumina to make the final product. One of the key steps in the Bayer process is the crystallization of aluminum trihydroxide ($Al(OH)_3$).

Crystallization is one of the most commonly used methods to purify a chemical solid. The production of basic crystalline commodity in the world exceeds 1Mt/year. Thus, better understanding of the process represents an enormous economic importance. In the past, fundamental research on crystallization was focused mainly on understanding and predicting the particulate nature of the crystalline phase. The recent advances in the electronic microscopy contribute to expand such knowledge and to further improve the understanding, by obtaining a direct relationship between the crystal structure and the processing conditions (such as temperature and impurities). The crystal properties such as the size, shape, purity, structure strength and resistance to abrasion determine the suitability of the crystals for industrial applications (Zaknich, 1997). These properties of the produced crystals depend on the processing conditions.

In the present study, the crystallization process and the morphology of aluminum trihydroxide, $Al(OH)_3$, was studied under various processing conditions. The reactor temperature, the initial concentration ratio of alumina to sodium oxide, $[Al_2O_3]/[Na_2O]$, and the concentration of the two impurities, titanium oxide and ferric oxide, were varied.

Note that the concentration ratio of $[Al_2O_3]/[Na_2O]$ defines the ratio of aluminum and sodium dissolved in the solution and is commonly used in literature and industry (See Appendix A). The crystal morphology was observed under Scanning Electron Microscope (SEM). X-ray diffraction was used to characterize the various polymorphs of $Al(OH)_3$ as well as the impurities present in the crystals. Furthermore, the zeta-potentials and the settling velocities were measured to confirm the effect of the impurities on the agglomeration of $Al(OH)_3$.

## *1.1 Bayer Process*

There are various hydroxides of aluminum with different physical and chemical characteristics. Their production is an intermediate stage in the production of alumina ($Al_2O_3$). Figure 1.1 shows the different aluminum hydroxides. From this classification, the crystalline forms of aluminum trihydroxide are the most-well defined.

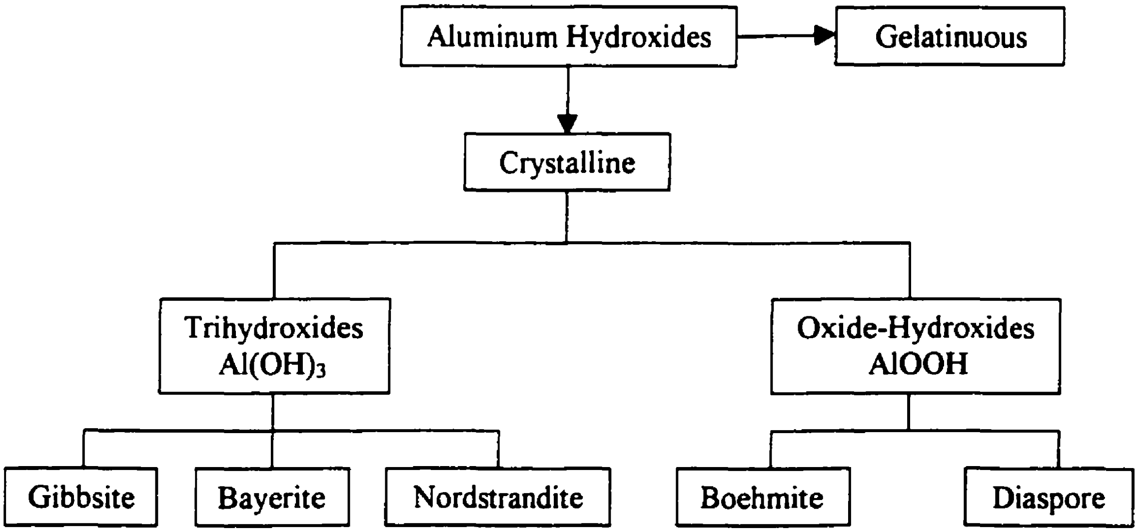

**Figure 1.1:** Different compounds involved in the production of alumina (Misra, 1986).

The difference in the stacking order of the $[Al_2(OH)_6]_n$ double layers defines the three main polymorphs of the aluminum trihydroxide: gibbsite, bayerite and nordstrandite (Misra, 1986). Figure 1.2 shows all the polymorphs of $Al(OH)_3$ produced as a function of the temperature and the pressure of the reactor. For a temperature lower than 100°C, only gibbsite or bayerite are stable. Bayerite, however, is unstable at a temperature higher than 20°C. In an aqueous solution it is converted to gibbsite in the presence of $Na^+$ ions (Misra, 1986).

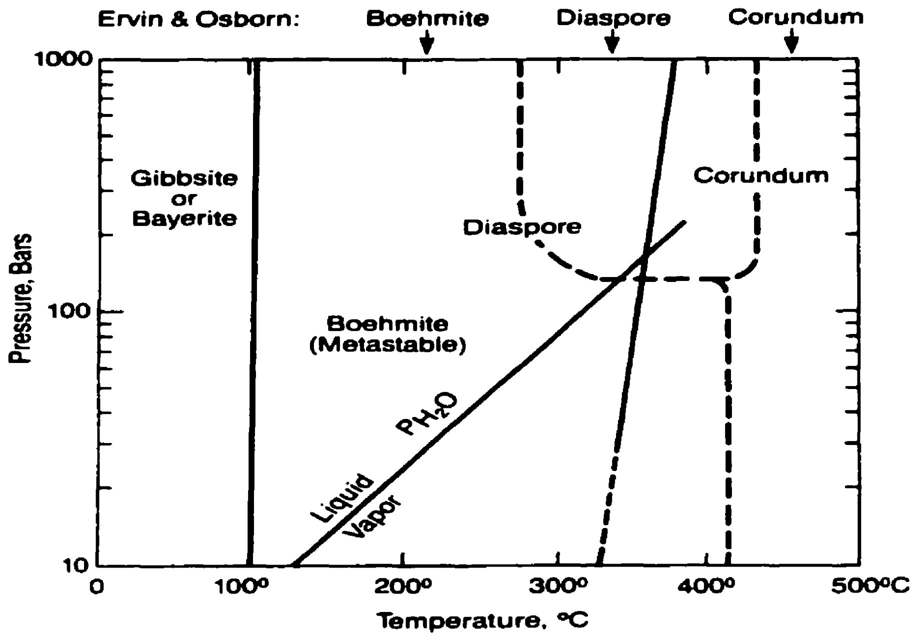

**Figure 1.2:** Different polymorphs of the aluminum trihydroxide formed as a function of the temperature and pressure in the reactor (Misra, 1986).

The Bayer process, developed by Karl Josef Bayer over 100 years ago, involves the production of aluminum trihydroxide and alumina. A flow chart of the Bayer process is shown in Figure 1.3. The process involves four basic steps: digestion, clarification, crystallization and calcination (Weiss, 1995).

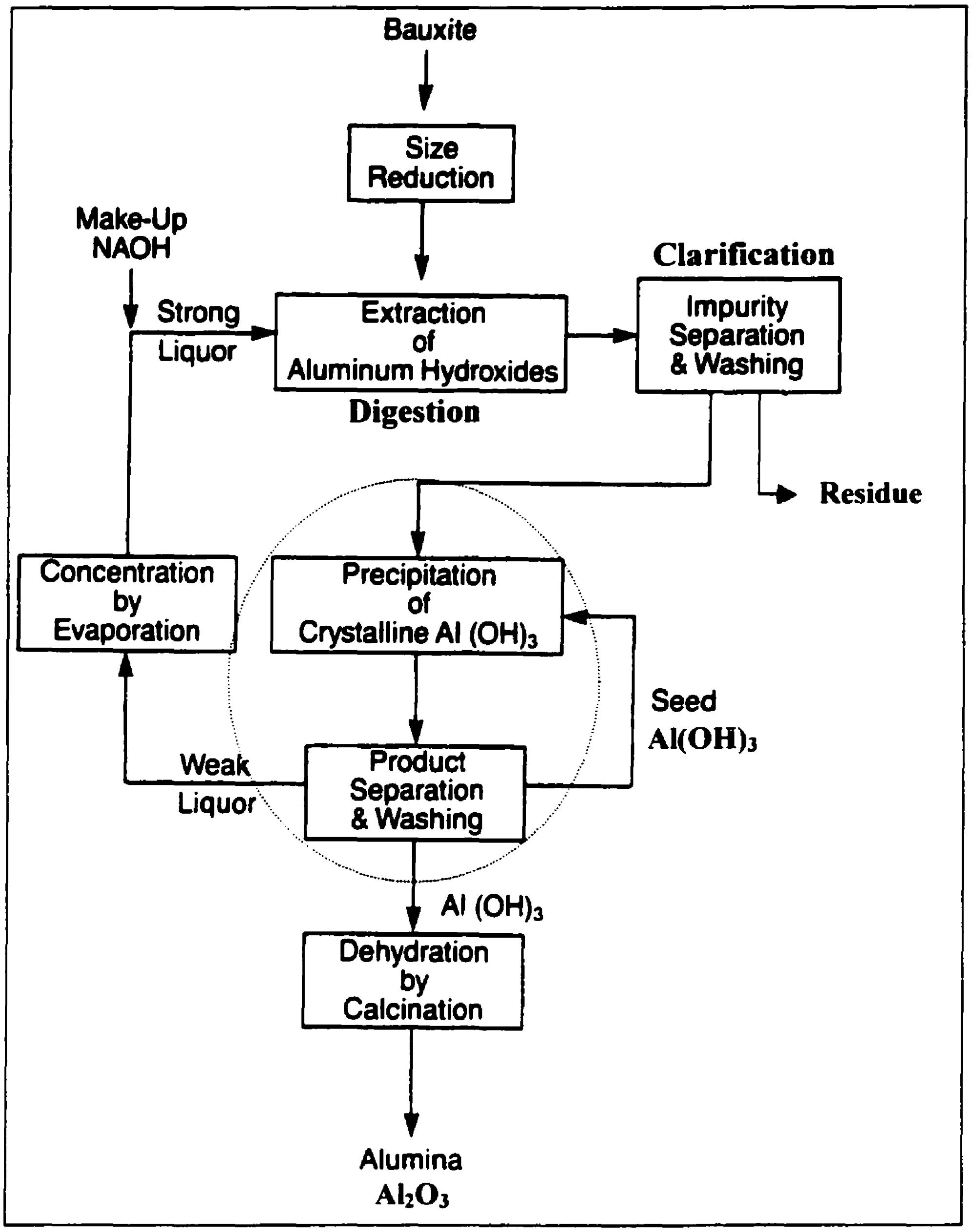

**Figure 1.3:** The production of alumina by the Bayer process (Misra, 1986).

- Digestion

The crushed and powdered bauxite is digested in a strong caustic soda solution at atmospheric pressure and at a temperature up to 240°C to dissolve the gibbsite ($Al(OH)_3$) contained in the ore. The advantage of using bauxite as an aluminum source is that it can be digested at a relatively low temperature and pressure compared to other aluminum ores. The chemistry of the digestion process can be written as the reactions of gibbsite with the sodium hydroxide solution (Misra, 1986).

For the gibbsite (represented by $Al(OH)_3$):

$$Al(OH)_3(solid) + NaOH(aq) \Leftrightarrow NaAlO_2(aq) + 2\,H_2O(aq) \quad (1)$$

- Clarification

Upon digestion, aluminum trihydroxide is dissolved in the caustic solution. Any insoluble residues of iron oxide, silica or insoluble $Al(OH)_3$, remain as solid particles. These are removed from the caustic solution by settling in the clarification step.

- Crystallization

The critical step of the Bayer process is the crystallization of aluminum trihydroxide from the caustic solution. The hydrate-rich solution, after the clarification stage, is cooled, seeded with small $Al(OH)_3$ crystals and cooled again. At the end of the process, the precipitate is washed in order to remove the final traces of caustic soda and other impurities. Aluminum trihydroxide is then recovered from the sodium aluminate solution. One disadvantage of this process is that it is very slow despite the high supersaturation and heavy seeding. A large fraction of soluble $Al(OH)_3$ remains in the spent liquor.

At the high temperature and the high concentration of caustic solution used in the digestion process, the reaction in the equation 1 proceeds from left to right. After the liquor is cooled and diluted, the overall reaction of the crystallization of $Al(OH)_3$ proceeds from right to left :

$$NaAlO_2(aq) + 2\,H_2O\,(aq) \Leftrightarrow Al(OH)_3\,(solid) + NaOH(aq) \qquad (2)$$

- Calcination

After washing and filtering, the hydrated $Al(OH)_3$ crystals are calcined (or 'roasted') at high temperature to dehydrate the $Al(OH)_3$ crystals to form the final product, alumina ($Al_2O_3$). The final product with more than 99% purity is in a form of fine white powder (Misra, 1986).

## *1.2 Crystallization process*

The important step in the Bayer process, as explained in the previous section, is the crystallization process, which consists of two steps: nucleation and growth. Nucleation is the formation of small crystals (nuclei) which subsequently undergo many transformations (such as crystal growth, agglomeration or recrystallization) until they reach their final state at the end of the crystallization (Söhnel and Garside, 1992). Figure 1.4 shows the crystallization process as a function of time. The particle-size distribution of the final crystalline product depends on the nucleation and growth. As observed in this figure, when $Al(OH)_3$ is supersaturated in a caustic solution, primary nucleation (nucleation without seed) takes place. The formation of nuclei crop depends on the reactor's temperature, the initial relative concentration of aluminum to sodium ratio and the impurities contained in the solution.

Upon the formation of the first precipitate, precipitation proceeds by three different methods:

- Secondary nucleation, which involves the formation of a new solid phase in a seeded solution.
- Secondary changes of the crystals (ripening, aging, agglomeration and coagulation) if the precipitated crystals are sufficiently small.
- Growth of the crystals.

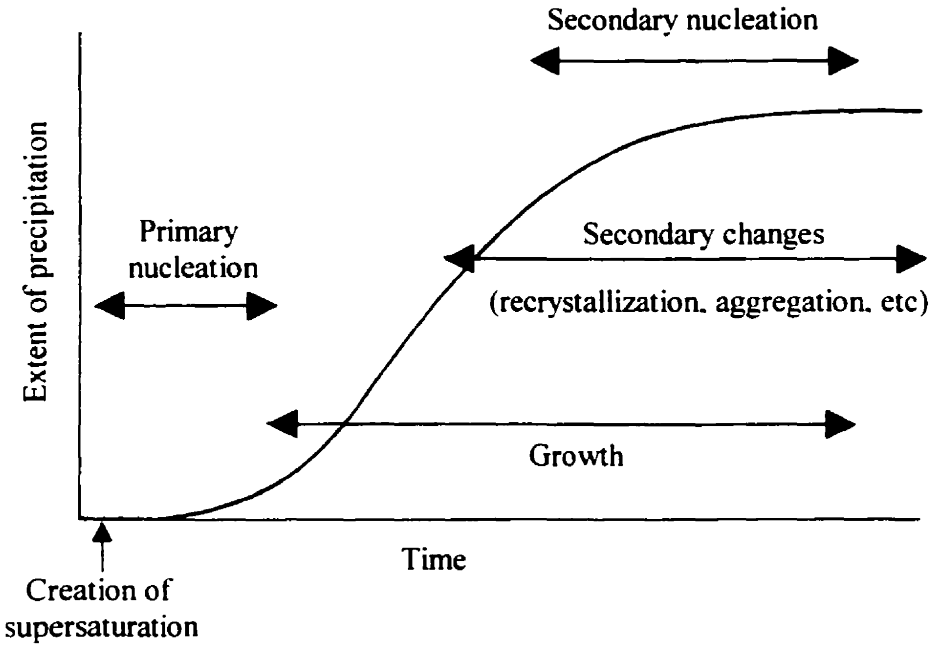

**Figure 1.4:** The different processes involved in the production of a crystal (Söhnel and Garside, 1992).

In a batch reactor, initially seeded with $Al(OH)_3$, the crystallization process starts immediately by a secondary nucleation. All these processes (secondary nucleation, secondary changes and growth of the crystals) are closely related and can occur simultaneously.

Depending on the reactor conditions and the precipitation time, the crystal size distribution can vary. For example, more rapid precipitation can be induced by a high supersaturation of $Al(OH)_3$. Thus, the degree of supersaturation of $Al(OH)_3$ in the caustic solution is a very important parameter in this process. High supersaturation favors the production of a large number of crystals by primary nucleation. In contrast, the decrease in the supersaturation level in the batch process limits the precipitation process and thus reduces the average crystal size (Söhnel and Garside, 1992).

## *1.3 Crystal morphology and structure of $Al(OH)_3$.*

A crystal consists of a rigid lattice of molecules or atoms; their locations are characteristics of the substance. For example, $Al(OH)_3$ crystallizes in the face-centered cubic system. The regularity of the internal structure gives to the crystal smooth surfaces or plane faces, which allow the crystal growth. The planes of these faces are parallel to atomic planes in the lattice. Generally, each growing crystal is unique in its conception, and has completely different size and external shape.

The growth rate of the $Al(OH)_3$ crystals, mostly the slow-growing faces, has a strong effect on the strength and the morphology of the crystal. The latter is governed not only by the crystal structure and crystal defects but also by the environmental conditions of the crystal growth. For instance, new scanning electron microscopic (SEM) studies reveal that the crystals generated in a batch reactor and in a continuous stirred tank reactor can have different growth patterns and crystal structures (Roach *et al.*, 1998). The chemisorption of an impurity can cause also chemical changes in the crystal surface resulting in a new structural appearance and thus new crystal properties. The other main parameters controlling the properties of the $Al(OH)_3$ crystal growth will be discussed in detail in section 2.4.

## *1.4 Imperfections and impurities in crystals*

Perfect crystals with homogeneous physical and chemical properties are rare and in many cases they are not required. In fact, the lattice imperfections and other defects confer important chemical and mechanical characteristics on crystalline materials. There are three main types of lattice imperfection (Zettlemoyer, 1969):

- Point (zero dimensional): results of interstitial, substitutional impurity, vacancy.
- Line (one-dimensional).
- Surface (two-dimensional): due to mechanical thermal stresses or irregular growth.

These surface defects are believed to be due to the change in the crystal growth pattern, which is greatly influenced by many factors including the presence of impurities in the crystal (Zettlemoyer, 1969). Thus, a better understanding of the effect of soluble and insoluble impurities on the crystal structures is necessary to optimize the process. The imperfections can be caused, for example, by the presence of chlorides, phosphates, sulphates, fluorides carbonates, calcium, iron and silica in the pregnant sodium aluminate liquor (Patnaik and Vidyasagar, 1998). Some of the main impurities originating from bauxite and caustic soda are listed in Table 1.1.

**Table 1.1:** Example of impurities present in the row bauxite and the purified $Al_2O_3$ produced by the Bayer process.

| **Jamaican bauxite (Blankenship, 1999)** | | **Alumina produced by NAPCO** | |
|---|---|---|---|
| Chemistry | Typical | Chemistry | Typical |
| $Al_2O_3$ | 48.2% | $Al_2O_3$ | 96.34% |
| $TiO_2$ | 2.38% | $TiO_2$ | 2.65% |
| $SiO_2$ | 0.70% | $SiO_2$ | 0.56% |
| $Fe_2O_3$ | 19.60% | $Fe_2O_3$ | 0.08% |
| CaO | 0.60% | CaO | 0.15% |
| L.O.I | 27.30% | MgO | 0.50% |

The physical properties of the final product (aluminum) produced with the alumina depend on the purity of the aluminum (Table 1.2). Noticeable changes in the electrical resistivity and thermal conductivity are observed at lower purity.

**Table 1.2:** Physical properties of different aluminum (Varley, 1970).

| Property | Purity | |
|---|---|---|
| | 99.99% | 99% |
| Melting point, °C | 660.2 | 657 |
| Latent heat of fusion, cal/g | 94.6 | 93 |
| Density at 20°C, g/cm$^3$ | 2.7 | 2.71 |
| Electrical resistivity μΩ–cm at 20°C | 2.68 | 2.87 |
| Reflectivity (total) | 90% | Less than 86% |

## *1.5 Objectives : the research Project*

The production of alumina by the Bayer process has been practiced since 1888 and research has been going on since then; however, there has been a renewed interest in the study of the relation of growth and morphology due to the recent refinements in the techniques for the analysis of crystal. The main objective of this work was to study some of the main factors that affect the crystallization of $Al(OH)_3$. The specific objectives were:

(1) To determine the influence of temperature and concentration on the concentration of the particles (slurry density), the dissolved aluminum and sodium concentration and the morphology of the crystals formed.

(2) To determine the effect of insoluble impurities ($TiO_2$ and $Fe_2O_3$) on the concentration of the particles (slurry density), the dissolved aluminum and sodium concentration and the morphology of the crystals formed.

(3) To propose the different mechanisms involved in the evolution of the crystal.

Experiments at different temperatures and different initial concentration of dissolved aluminum and sodium as well as impurities were performed. Analytical techniques, such as x-ray diffraction analysis, zeta-potential analysis and settling velocity measurements were used to examine the effect of impurities on the properties of the produced crystals.

# Chapter 2

# LITERATURE REVIEW AND TECHNICAL BACKGROUND

## *2.1 Supersaturation conditions.*

The rate and the mechanism of crystal growth in solution depend on supersaturation. Unless the mother solution is supersaturated, crystals can neither form nor grow. The supersaturation refers to the quantity of solute present in the solution compared with the quantity that would be present in the solution at the equilibrium (Perry and Green, 1997). The equilibrium solubility in the aluminum trihydroxide solution can be determined from an empirical model developed by Misra (1970):

$$\ln R_{eq} = 6.2106 - \frac{2486.7}{T+273} + 1.08752 \times \frac{C}{T+273} \qquad (3)$$

where $R_{eq}$ : the equilibrium ratio ($Al_2O_3/Na_2O$ by wt).

T : the temperature of the reactor (°C) (between 25 and 100°C).

C : the caustic concentration (g/L) in the solution expressed by $Na_2O$ (in a range between 30 and 230 g/L).

This correlation has the advantage of being simple and representative of the driving force by subtracting it from the actual $Al_2O_3/Na_2O$ ratio present in the mother liquor. As discussed in p. 2, all the aluminum and sodium concentrations are expressed as a function of $Al_2O_3$ (noted A) and $Na_2O$ (noted C) respectively. The ratio is thus noted A/C ratio and is commonly used in literature and industry.

## 2.2 Description of the aluminum trihydroxide crystal.

The aluminum trihydroxide has a hexagonal (rhombic) crystal shape (Figure 2.1). The agglomerated particle consists of many individual crystals fused together. During the growth process, the deposition of fresh hydrate increases the size of the $Al(OH)_3$ particle.

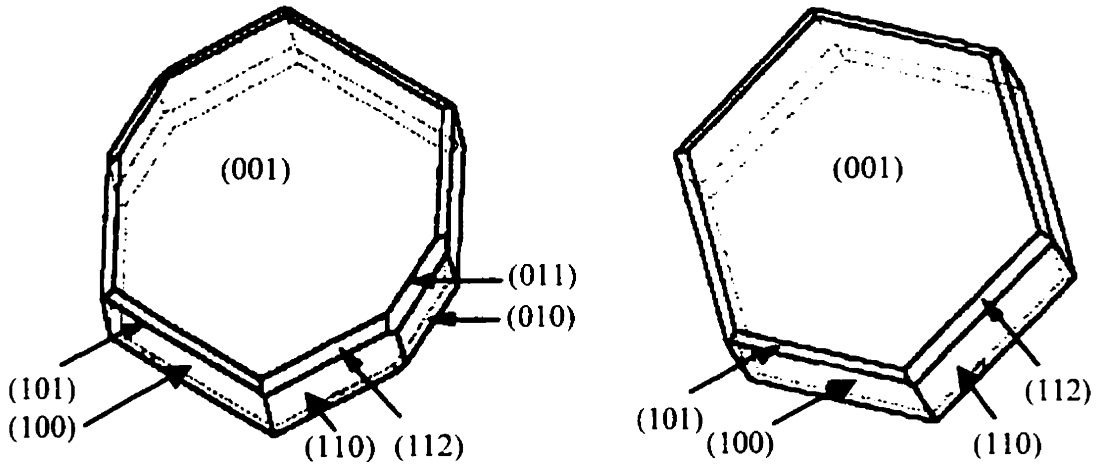

**Figure 2.1:** Typical morphologies of the $Al(OH)_3$ (Seyssiecq *et al.*, 1999).

Bigger particle sizes can be obtained by agglomeration. Agglomeration is favored by minimal agitation and high precipitation rate. From the first appearance of a new particle as a nucleus, the particle undergoes growth and secondary change like agglomeration. These fines, obtained at a specific agitation level, originate from nucleation rather than attrition (crystal breakage). The nuclei are called lamelar dendrites, which form and easily separate from the largest hydrate particles. Nucleation increases exponentially with supersaturation. The crystals have various shapes and surface textures. Zaknich (1997) categorizes the crystal properties in terms of particle shape, single crystal, texture, crystal size, agglomeration, susceptibility to breakdown and type.

## *2.3 Crystal growth mechanism*

In general, a new surface can be created by three different ways (Söhnel and Garside, 1992):

A. Two homogeneous phases are cleaved into two parts and then the halves formed are put into contact.

B. The transfer of atoms or molecules from one phase to another (growth of $Al(OH)_3$).

C. The stretching out of an old surface.

In the first two cases A and B, the chemical bonds are broken during the formation of the new surface. The sum of all the broken bonds for a unit area corresponds to the specific surface free energy, $\sigma$. In the case of C, only the surface energy of the crystal changes, the number of broken bonds remains unchanged. The resulting crystals will be the most stable state possible. The crystallization of aluminum trihydroxide in a well mixed reactor is achieved by the surface integration process; the transfer of atoms in case B. The growth takes place at the crystal ambient phase interface in a caustic solution. The growth rate is simply proportional to the flux of atoms from the ambient phase and the density of the growth sites (half crystals or kink positions) which the faces offer to the building units. This density is related to the crystallographic orientation of the face and to the temperature of the system.

The group of atoms, which integrate on to the crystal surface during the crystallization process, is called the growth unit (Söhnel and Garside, 1992). Figure 2.2 shows a planar representation of the gibbsite growth unit. It is formed by two aluminum atoms surrounded by ten hydroxyl groups of which two of them are shared by the aluminum atoms. This growth unit can be directly placed into the gibbsite growth sites called kinks as in Figure 2.3.

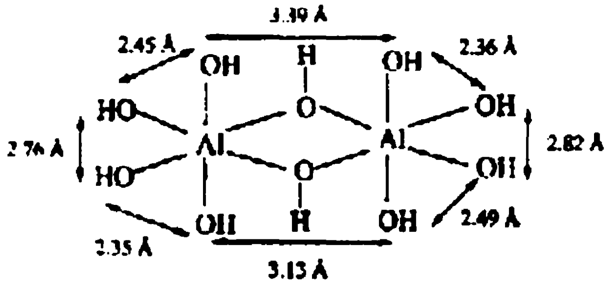

**Figure 2.2:** A planar representation of Gibbsite growth unit (Seyssiecq *et al.*, 1999).

The atomically rough face of a crystal or dislocation, for example, offers a great number of kink positions. Building particles from the mother solution are easily incorporated to the crystal lattice. When the chemical potential of the solution is greater than that of the crystal (supersaturation), the growth units of the crystallizing material (atoms, ions or molecules) are adsorbed to kink positions. They become part of the crystal. In any other position they are connected more weakly to the crystal surface than the atoms at the kink positions. The surface of a crystal, however, is more complicated and differs from this ideal plane surface. The growth units move in a random manner, colliding with one another. In some cases, the formation of a critical two-dimensional nucleus can result from these collisions. The 2-D nucleus steps initially appear randomly on the surface (Figures 2.4 and 2.5).

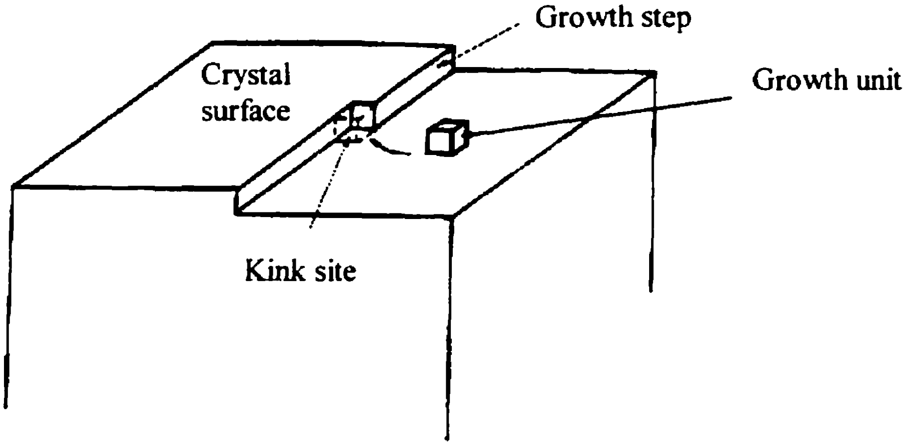

**Figure 2.3:** Attachment of a growth unit from the adsorption layer on the crystal surface into a kink site (Söhnel and Garside, 1992).

The nuclei are in metastable equilibrium with their surrounding and have an equal probability of growing or dissolving. They are very unstable and tend to dissolve into the caustic solution. However, when they reach a critical size their growth is thermodynamically favored.

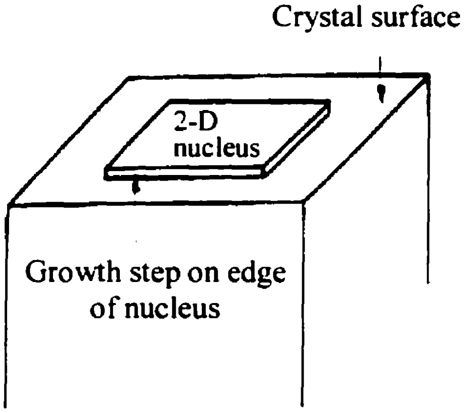

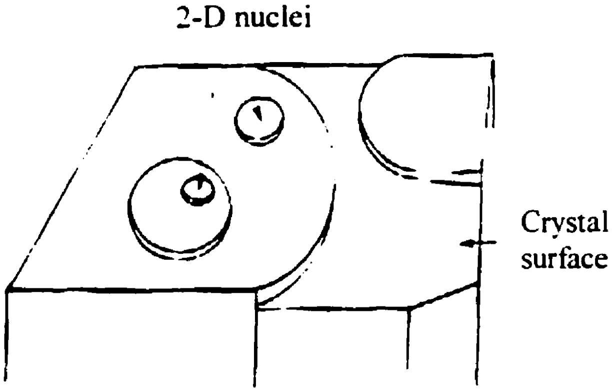

**Figure 2.4:** Two-dimensional nucleus on a crystal surface (Söhnel and Garside, 1992).

**Figure 2.5:** Growth of a crystal by a polynuclear mechanism (Söhnel and Garside, 1992).

In the case of a multinuclear layer by layer growth, the face restores the initial surface plane. The growth is a periodic process involving successive 2-D nucleation and a slow lateral growth as shown in Figure 2.6. However, the formation of 2-D nuclei and the rate of growth are functions of a critical supersaturation. Some energetic difficulties can also appear during the layer formation resulting in a polynuclear mechanism. A bilayer growth is then observed with states of higher and lower total step densities (Figure 2.7).

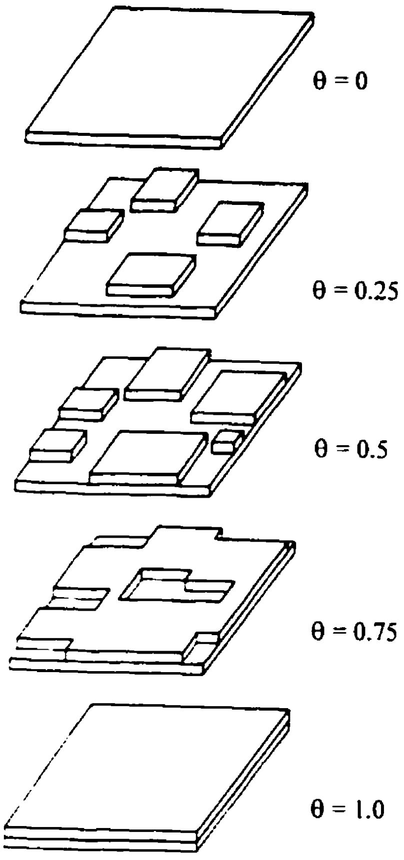

**Figure 2.6:** Theoretical crystal formation by multinuclear layer-by-layer growth (Markov, 1995).

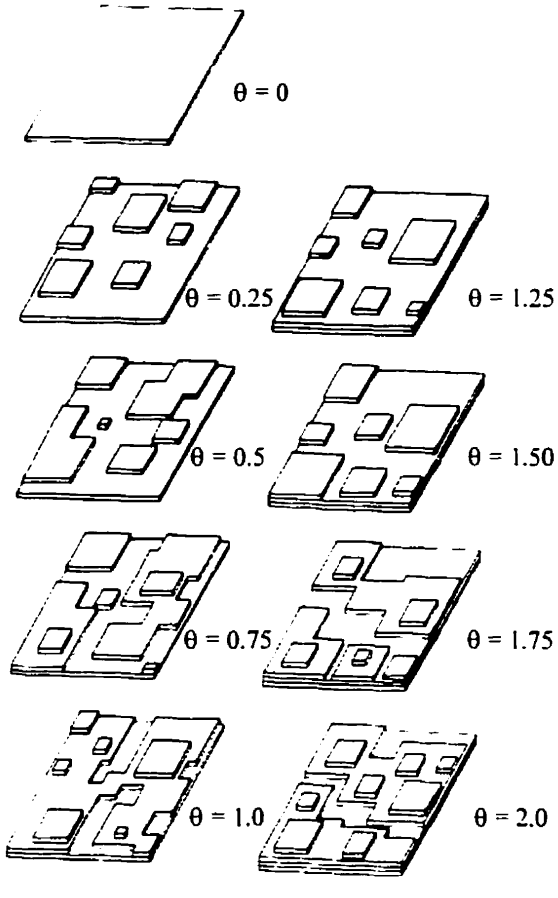

**Figure 2.7:** Theoretical different stages of a bilayer formation (Markov, 1995).

Another mechanism, the spiral process, results from a continuous growth at low supersaturation. This mechanism is observed in a batch reactor after the step of "first nucleation". The supersaturation is lower and favors the growth process. However, as shown in Figure 2.8. the presence of crystal defects like screw dislocation offers nonvanishing monatomic steps (Markov, 1995). The kink positions available make the 2-D nucleation unnecessary in this case. As a result, a growth hillock around the screw dislocation is formed.

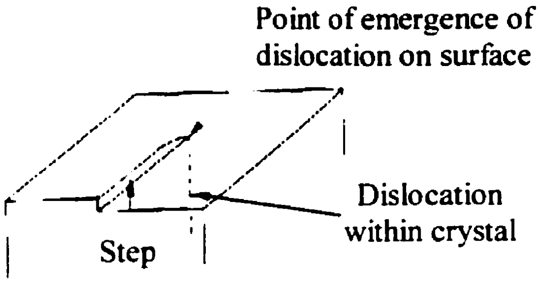

**Figure 2.8:** Growth step originating at a screw dislocation (Söhnel and Garside, 1992).

Markov (1995) explains this phenomena in more detail. As shown on Figure 2.9, at the initial moment for a given supersaturation, the dislocation offers a single step with a lower terrace. The growth units join the kink sites along the initial step (a) and favor the formation of a new step (b). The step, assimilated to a two dimensional cluster, is then between a two dimensional nucleus and a spiral growth process. When the length of the second step exceeds the edge of a two-dimensional nucleus, the cluster becomes thermodynamically favored. The crystals in the second step begin to grow. From the growth of the second step proceeds to the third step, (c), and continues further (Markov, 1995).

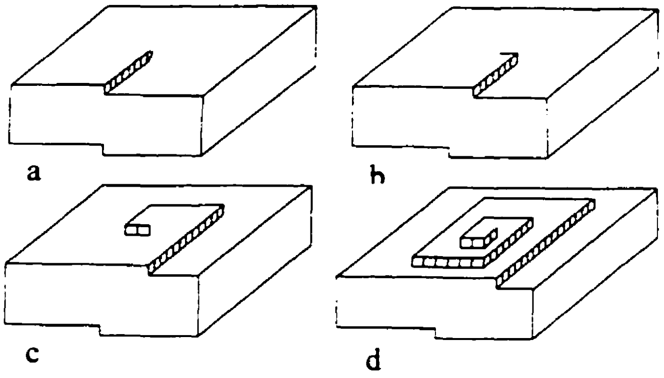

**Figure 2.9:** Formation of a spiral with a square shape around the screw dislocation (Markov, 1995).

Since the crystal can grow with different mechanisms, the relative sizes of its faces must have different translational velocities. The overlapping principle is based on these variations of velocity (Perry and Green, 1997). Following this principle, in the case of a crystal growth, the faces with the lowest translational velocities survive while the others slowly disappear. In contrast, during the dissolution of a crystal, the faces with fast translational velocities survive. This principle is illustrated on the following drawing of the cross section of a growing crystal.

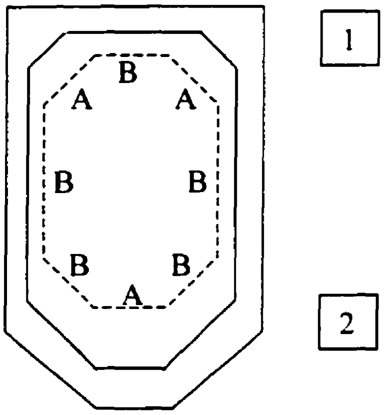

**Figure 2.10:** Growth of a crystal under the overlapping principle (Perry and Green, 1997).

Each polygon represents different times in the growth of a crystal on this figure. The initial hexagonal crystal is delimited by the dashed line. The faces A have high translational velocities and can grow fast. In contrast, the faces B have slow translational velocities and grow slowly. As denoted in the Figure 2.10, only the slower B face remains in the case 1 giving a uniform flat surface. In the case 2, the hexagonal structure still exists. During the growth process, the faces B overlap the faces A.

## 2.4 Parameters affecting the crystallization of $Al(OH)_3$

The physical characteristics of the aluminum trihydroxide crystals as well as the impurity levels need to be controlled during the crystallization process to meet product specification. In view of the large-scale operations involved in the industry, any variations in the process can have considerable repercussion on the final product. Thus, such variations need to be determined at their early stages and corrected. Several studies have been carried out to define the parameters influencing the crystallization process and their effect on the final crystal (Armstrong *et al.*, 1996; Scott, 1963; Patnaik and Vidyasagar, 1998; Dianfeng *et al.*, 1997). The main factors are:

1. Precipitation time and the ageing of the aluminate solution.
2. Temperature
3. Supersaturation
4. Seed
5. pH
6. Stirring rate
7. Impurities

During the crystallization process of $Al(OH)_3$, the growth rate of the crystal is very slow. Satapathy and Vidyasagar (1990) reported a growth rate of 0.4 to 1 μm/ day and a temperature of 60°C to 64°C respectively. In this case, the mother liquor was composed of 151 g/L of $Na_2O$ and 108 g/L of $Al_2O_3$, corresponding to an initial A/C ratio of 0.71. A review of literature shows the predominant effect of the temperature and the supersaturation on the crystallization process compared to the others parameters. Seyssiecq *et al.* (1998) indicates that at high temperature (70°C rather than 55°C) and high initial supersaturation of the mother liquor (1.8 rather than 1.4), the agglomeration rate of gibbsite crystals was enhanced in a batch reactor.

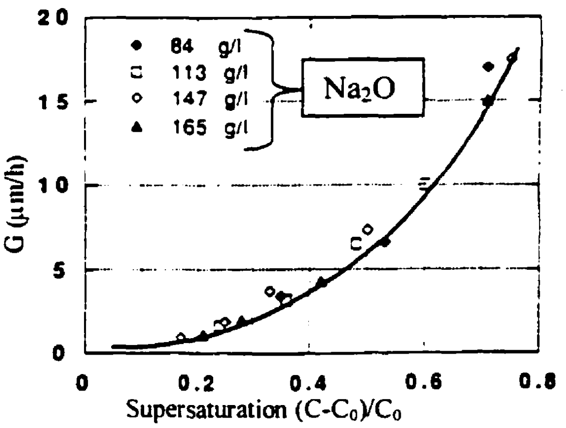

**Figure 2.11:** Effect of the initial sodium concentration (expressed in $Na_2O$) and of the supersaturation on the growth rates of $Al(OH)_3$ for a fixed temperature of 89.5°C (Veesler and Boistelle, 1993).

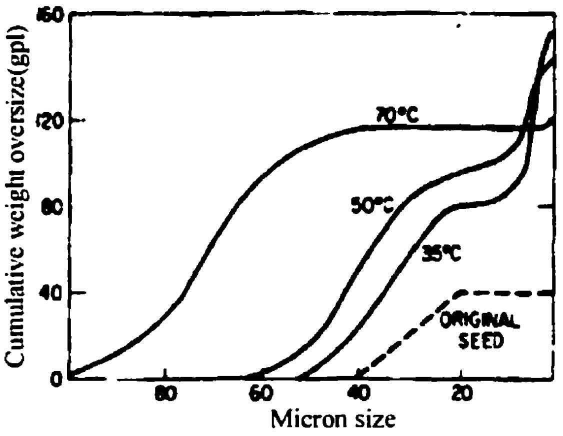

**Figure 2.12:** Effect of the temperature on the crystallization (a seed charge of 40 g/L, initial concentration of 130 g/L of $Na_2O$ and $Al_2O_3$, precipitation time of 96 hours) (Scott, 1963).

The influence of the initial supersaturation was also discussed in the case of batch experiments by Veesler *et al.* (1994). They concluded that the agglomeration and the crystal growth become negligible at low supersaturation. The supersaturation is necessary directly on the crystal growth. In the case of the effect of the temperature, Scott (1963) that an increase of the temperature increased the growth rate and agglomeration but decreased the amounts of new nuclei. The resulting crystals were coarser (Figure 2.12). An industrial application of this effect is to increase the temperature, whenever there is a rise in nucleation, to control it. Increasing the temperature favors the formation of bigger particles of $Al(OH)_3$ and thus favors their separation from the solution by settling. By controlling the temperature and the pressure, different polymorphs of $Al(OH)_3$ could also be produced (Misra, 1986). Scott (1963) obtained bayerite at room temperature but by increasing the temperature more gibbsite was produced.

The stirring rate, the seed and the others parameters have also effects on the crystallization process as well. Stirring is necessary to have a homogeneous suspension of the crystals and contributes to the attrition (Chan and Ang, 1996). Seyssiecq *et al.* (1998) reported that an increase in the stirring rate from 330 to 520 rpm can decrease the degree of agglomeration and favored the formation of fine crystals due to the attrition (Figure 2.13). In the same publication, Seyssiecq *et al.* showed the influence of the size and the mass of the seed at constant supersaturation and temperature. They obtained a variation of the degree of agglomeration by increasing the mass of seed from 1 g/L to 250 g/L. As shown in Figure 2.14, the degree of agglomeration increased until a seed charge of around 80 g/L, due to the decrease of the distance between the particles. Over this optimum, the agglomeration decreased due to the attrition. A decrease of the size of the seed showed the same type of curve but an augmentation of the degree of agglomeration was observed.

seed showed the same type of curve but an augmentation of the degree of agglomeration was observed.

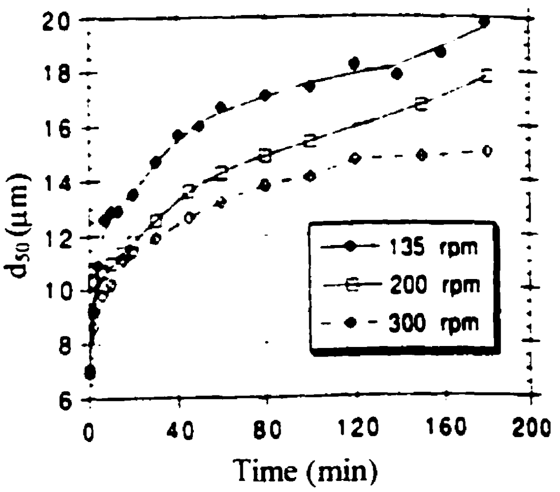

**Figure 2.13:** Effect of the stirring rate on the crystals (70°C, an initial supersaturation $C_{Al}/C_{Al\,eq}$ of 1.5, seed charge of 50 g/L) (adapted from Veesler *et al.*, 1994).

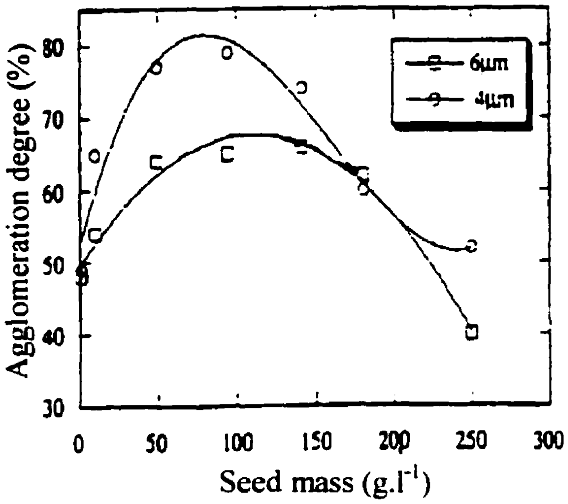

**Figure 2.14:** Effect of the charge and the size of the seed and the degree of agglomeration (70°C, an initial supersaturation $C_{Al}/C_{Al\,eq}$ of 1.4, precipitation time of 2 hours) (Seyssiecq *et al.*, 1998).

The pH of the solution is also important for the crystallization. As $Al(OH)_3$ is amphoteric, the pH varies the solubility of $Al(OH)_3$ in the liquor and then its precipitation (Misra, 1986). As observed in Figure 2.15, the solubility increases for an acid pH (lower than 4) and for a basic pH (higher than 10).

Another parameter affecting the crystallization process is the impurities present in the liquor solution. Literature reported changing in the physical properties of the liquor, the crystal morphology and the crystal habit (Seyssiecq *et al.*, 1999; Scott, 1963; Lee *et al.*, 1997). Thus, some impurities like oxalate and chloride affect the kinetics of the precipitation process by changing the properties of the liquor. In this case, the sodium oxalate enhances the nucleation and thus the formation of fine crystals. The chloride decreases the particle concentration but the size of the fines is increased (Scott, 1963). Other ionic impurities like sodium, carbonate, chloride and sulfate increase the solubility of alumina.

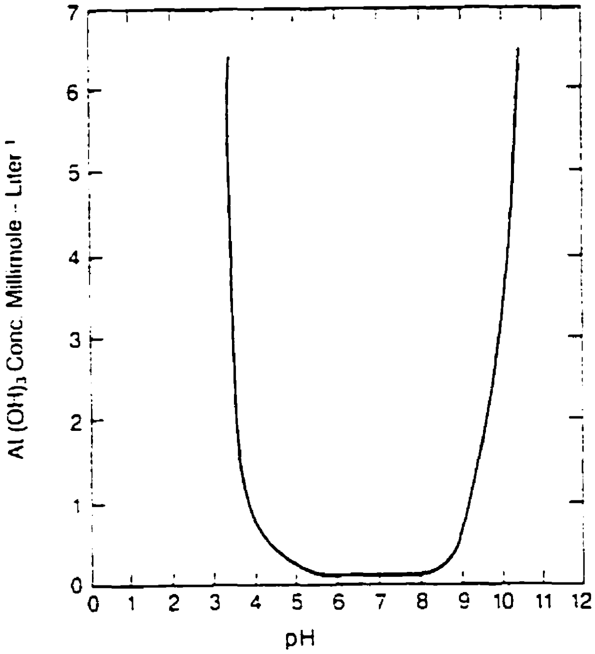

**Figure 2.15:** Effect of the pH on the solubility of Al(OH)$_3$ (Misra, 1986).

# Chapter 3

# MATERIALS AND METHODS

## *3.1 Apparatus and experimental conditions*

### 3.1.1 Batch reactor design

A batch reactor was used for the crystallization experiments. The reactor was made of a cylindrical glass vessel with an inner diameter of 125mm. The working volume was $1dm^3$. The crystallization was carried out in a constant temperature bath (Neslab, GP 500). The temperatures were varied from 40°C to 80°C (± 0.1°C) for a precipitation time of 24 hours.

In order to increase the mixing inside the reactor, and thus increase the homogeneity of the suspension mixture, four removable baffles with flat vertical strips were radially located along the reactor wall. The baffle had a diameter of 12mm corresponding to the one tenth of the reactor diameter as recommended by the Weiss (1995).

In order to minimize the accumulation of solids on the surface, the baffles were placed one half of their width from the vessel wall. The mixture was agitated at constant speed (300 rpm) by an impeller whose speed was varied depending on the vessel configuration as well as the type of impeller. In order to ensure the homogeneous suspension of the precipitate, a radial flow stainless steel impeller was used in the experiment. The schematic diagram of the experimental set up is shown in Figure 3.1.

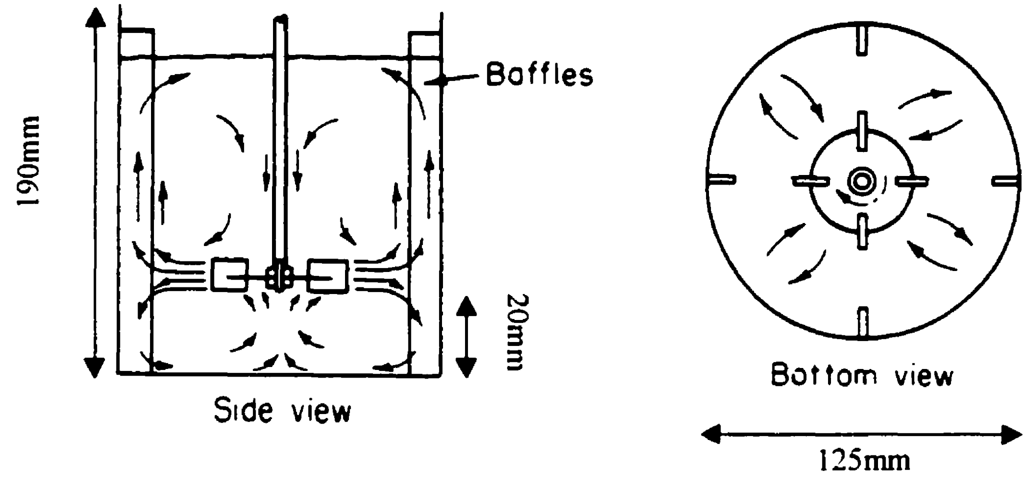

**Figure 3.1:** Flow pattern in the baffled reactor with the turbine positioned at the center (Perry and Green, 1997).

The flat-blade turbine had a diameter of 50 mm, 0.4 times the size of the tank diameter as recommended in literature (Coulson and Richardson, 1996). The impeller speed as well as the torque were controlled automatically by the stirrer (Caframo BDC 3030). The minimum impeller speed required for homogeneous suspension was determined experimentally (section 4.1.1).

In order to examine the reproducibility of the experiments, two reactors were operated together in parallel, and the reaction was carried out simultaneously using the same mother solution. At the end of each experiment, the components in the reactor were washed with concentrated sulfuric acid (Reagent A300-P500, A.C.S, Fisher Scientific) in order to remove any precipitate residues.

### 3.1.2 Preparation of the mother liquor

A synthetic supersaturated sodium aluminate solution was prepared according to the method described by Addai-Mensah *et al.* (1998). Before each experiment, the mother liquor was freshly prepared using aluminium powder (A559-500 supplied by

Fisher Scientific), NaOH (30% w/w, SS255B-1, supplied by Fisher Scientific), and distilled water. A fixed amount of NaOH was first dissolved in distilled water, followed by a gradual addition of a known weight of aluminum metal. The reaction was instantaneous and quite vigorous. Thus, extra care was taken to ensure the slow addition of the aluminum powder. Upon complete dissolution, the mixture was filtered through a 0.45 μm glass microfibre membrane (Whatman; 934-AH; Cat. No. 1827 055). After filtration, the solution was optically clear. The solid residual, composed mainly of aluminum and impurities, was washed with hot distilled water and air dried at 100°C for later analysis.

### 3.1.3 Preparation of the precipitate.

The precipitates from each experiment were collected in glass vials. The samples were taken rapidly but with care in order to avoid any fractures or phase changes in the crystal structure. A known volume of the supersaturated sodium aluminate solution was filtered through a 0.45 μm glass microfibre membrane (Whatman; 934-AH; Cat. No. 1827 055) to remove the crystals in suspension. The filtered solution was used for atomic absorption analysis as explained below while the precipitate collected on the filter was washed with hot distilled water before being air-dried at 100°C. The dried precipitate was used to calculate the slurry density. Another sample of particles was used for crystal analysis. This second suspension was centrifuged (RC-5 superspeed, Refrigerated centrifuge, Dupond instruments, Sorvall) at 5000 rpm for 5 minutes. The upper phase, which was the caustic solution was removed and replaced with hot distilled water. The crystals, in the bottom layer, were suspended and mixed with the solution. Then the mixed solution was centrifuged again. This procedure was repeated five times to remove all the sodium (see section 4.1.3). A small representative sample of the powder in suspension in the distilled water was air-dried at room temperature in a confined place. The dried crystals were dispersed to separate them from each other and to obtain a crystal density low enough to allow an image analysis. The crystals were glued on to a special SEM support (Aluminum pin mount 12.7×3.2, Soquelec, No C10075) and analyzed. The remaining crystals were stored in the final distilled water used for the washing. The storage solution contained 1% of sodium meta-bisulfite (Fisher Scientific S244-500, Certified A.C.S.) to disperse the crystals and avoid the agglomeration of the small particles.

### 3.1.4 Preliminary experiment on the stirring and the sampling position.

In order to determine the optimum impeller speed and sampling position, a solution simulating the mother solution was prepared according to the method by Chan and Ang, 1996. Aluminum trihydroxide crystals (A581-500 supplied by Fisher Scientific) were suspended in a mixture of glycerol-water at 25°C. The crystals contained, 0.10 wt% alkalies and earths, 0.0004 wt% Cl, 0.0015 wt% heavy metals, 0.0025 wt% Fe, 0.01 wt% $SO_4$, 34.05 wt% water of hydration and 0.16% water-soluble substances. Glycerol (99.5 wt%, G-33B, supplied by Fisher Scientific) was diluted in distilled water to prepare 28% by weight solution in order to simulate the viscosity of caustic aluminate solution at an operating temperature of 70°C.

### 3.1.5 Reference case

A crystallization experiment, conducted without any impurities at a temperature of 60°C and an initial alumina/caustic ratio of 1.38, was performed as a reference case. A temperature of 60°C and a precipitation time of 24 hours were recommended by Alcan International limited. These latter correspond to the conditions used to prepare an ultra pure aluminum trihydroxide (Alcan H-10 Hydrate). During this experiment, 12 samples were taken every 2 hours.

### 3.1.6 Main experiments

Main experiments having a duration of 24 hours were also conducted with a variation in the temperature, the initial ratio of aluminum to sodium and for the two different insoluble impurities $Fe_2O_3$ (I116-500, Fisher Scientific) and $TiO_2$ (T315-500, Fisher Scientific). Two extreme conditions were analyzed in each case. For each experiment, 1 g/L of pure gibbsite crystals with diameter less than 11 μm was used as seed (Warren and Armstrong, 1994).

**Table 3.1:** Main 24 hours experiments conducted for different parameters.

| **Parameters** | **Experimental set-up values** |
|---|---|
| Temperature (at a 1.3 initial A/ C ratio) | 45°C<br>80°C |
| initial A/ C ratios (temperature of 60°C) | 0.89<br>1.79 |
| Impurities: $Fe_2O_3$ (temperature 60°C) | 0.2 g/L. (1.15 initial A/C ratio)<br>0.7 g/L. (1.23 initial A/C ratio) |
| $TiO_2$ (temperature 60°C) | 0.20 g/L. (1.31 initial A/C ratio)<br>0.75 g/L. (1.31 initial A/C ratio) |

## 3.2 Sample analysis

### 3.2.1 Atomic Absorption

The supersaturated sodium aluminate solution was characterized using the atomic absorption (Thermo Jarrel Ash, Smith-Hieftje II). A volume of 100 µl of the filtered solution was diluted in 100 ml of distilled water to have a dilution of 1:1000. The instrument was calibrated using:

- Aluminum reference solutions (Reference solution certified 1000 ppm ±1%, CSA 442-500, Fisher Scientific) stabilized with 4% HCl (A 144P-500, Fisher Scientific Reagent A.C.S) at concentrations of 10, 30, 50 ppm.
- Sodium reference solutions (Reference solution certified 1000 ppm ±1%, CSS 139-500, Fisher Scientific) stabilized with 4% HCl at concentrations of 10, 25, 30, 40, 50, 100 ppm.

Figure 3.2 shows a typical calibration curve for the absorbence versus Al total concentration. The absorbence of the aluminum dissolved in the solution samples was generally below 0.2, (i.e., below a concentration of 50 ppm), for the wavelength used.

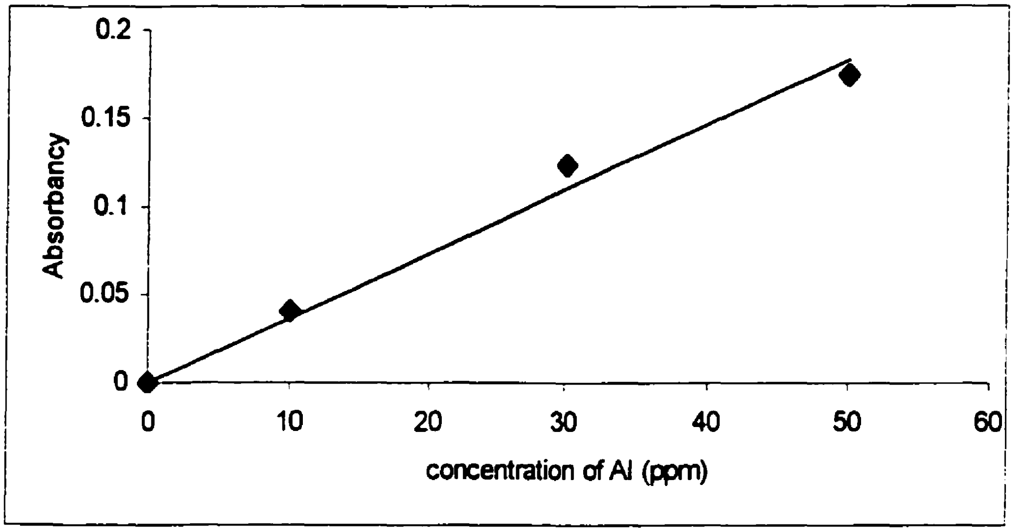

**Figure 3.2**: Typical calibration curve for atomic absorption.

### 3.2.2 Image analysis: Scanning Electron Microscope (SEM)

The particles were first examined under a microscope (Laborlux S Leitz) coupled with a digital video camera (Sony CCD-IR15 black & white video camera, model SSC-M374). As shown in Figure 3.3 (a), due to the brightness of the crystal and the high reflectance of the light, a Scanning Electron Microscope (SEM) JEOL 840 A was more appropriate. By using the SEM, the grey-scale digital images with good resolution, depth of field images, edge detail, surface texture and high contrast were obtained, as shown in Figure 3.3 (b). The background and the noise were eliminated in order to obtain an image background, which was as dark as possible with the only bright spots being the crystals. Furthermore, in order to study the impurities on the crystals, a x-ray (EDAX Phoenix Energy Dispersive X-ray) coupled with the Scanning Electron Microscope (SEM JEOL 840 A) was used.

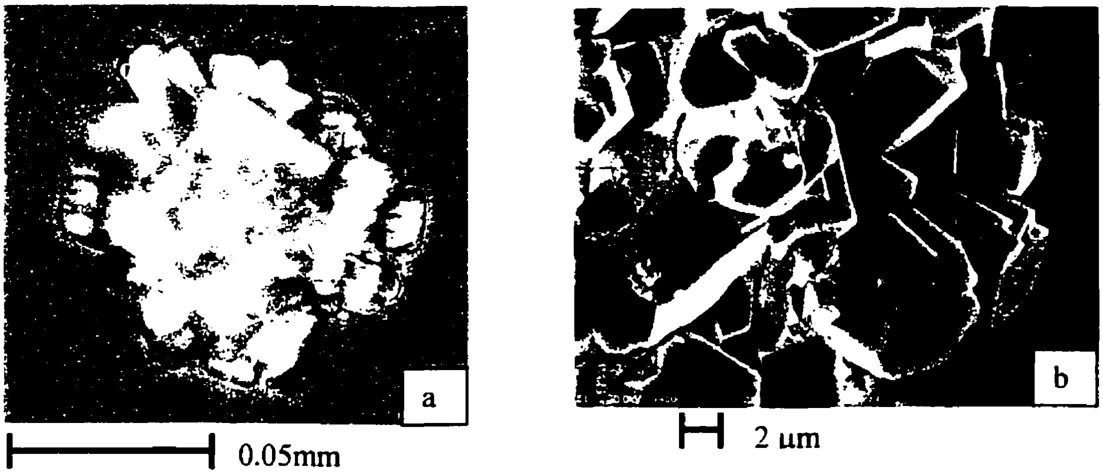

**Figure 3.3:** Pictures of $Al(OH)_3$ crystal with (a) a microscope (b) a SEM.

### 3.2.3 X-ray Diffraction analysis

The polymorphs of the aluminum trihydroxide (gibbsite in this study) and the impurities present in the precipitate were analyzed by a x-ray diffraction (Philips Diffractometer PW 1710). The spectra obtained were used to identify the impurities and the aluminum trihydroxide by using a database (JCPDS- International Centre for Diffraction Data, PCPDFWIN V.2.01, 1998).

### 3.2.4 Particle size analysis

The measurement of particle size varies in complexity according to the particle shape and the precision necessary. Different instruments were used to calibrate the size of the aluminum trihydroxide:

- Sieves to screen the precipitate at the end of the experiments. Mainly used during the drying to avoid the formation of flocs.

- Cyclosizer (Warman international PTY-LTD) to prepare a seed with a diameter less than 11 μm.
- Particle size analyzer (Brinkmann) to size the crystals after a 24 hours precipitation where the amount of crystals produced was enough.
- Image analysis (Particle/phase analysis EDAX, Phoenix) used to analyze images taken from the SEM. The diameter of the particle was measured by the software using the Martin's diameter, which is the simplest means of measuring and expressing the diameter of irregular particles (Heimenz, 1997). As shown in Figure 3.4, Martin's diameter is the length of a line that bisects the projected area of a particle. The direction of measurement is arbitrary and subjective but consistent to avoid bias.

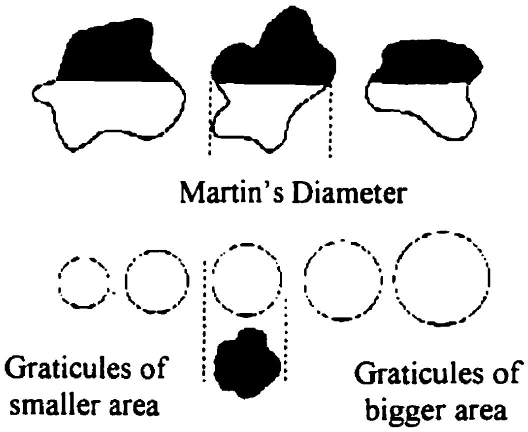

**Figure 3.4:** Characterization of the size of irregular particles (Heimenz and Rajagopalan, 1997).

- Particle size analyzer (Sedigraph 5000D, Micromeritics instrument corporation) used only during the preliminary experiments due to the limitation of the apparatus (maximum diameter of 100 μm for the particles).

### 3.2.5 Zeta-potential

The zeta-potential was measured according to the procedure defined by Vergouw *et al.* (1998) using a Laser-Zee meter (model 501, Penkem, Inc.). The measurements were made at room temperature (25°C) in less than one minute to avoid the excitation of the particles caused by the laser. Each crystal sample was dried and screened to obtain a size fraction less than 38 μm necessary for a good reading. One-half gram of sample was dispersed in 500 mL of $10^{-2}\,M$ KCl (AC 7600T, Anachemia chemicals LTD.) for 5 minutes. The pH of the mixture was adjusted by a pH-meter (accumet Research AR50, Fisher Scientific). Sodium hydroxide was used as a pH modifier. The stirring was fixed at 1000 rpm for homogeneous mixing. A volume of 25 mL of the suspension was taken to fill the sample chamber of the Laser-Zee meter. The zeta-potential was recorded accordingly. The reproducibility of the measurements as determined by many replicates of the samples was within ± 3 mV.

### 3.2.6 Settling velocity

The settling velocity was measured as suggested by Vergouw *et al.* (1998) to show an attractive interaction of the aluminum trihydroxide on impurities. A conventional settling test cylinder was modified to relate the conductivity between two rings, distant of 10 cm, to the settling velocity. A settling curve is thus obtained for each specific compound. The experiments were performed first by adjusting the pH with sodium hydroxide. The solids (a minimum of 2% v/v) were suspended and dispersed in a $10^{-2}$ M KCl solution by an end-over-end rotation of the cylinder. When the solution was homogenized, the cylinder was placed vertically and the time was set zero (the initial time). The evolution of the conductivity between the two rings was recorded accordingly by the computer software, called TableCurve (Jandel Scientific). These data were then converted to obtain settling velocity by Microsoft Excel. The determination of the settling velocity from this curve is shown in detail in Figure 3.5. The tangent of the settling curve (noted B) and the time T necessary to pass through the conductivity cell (L= 10 cm) are calculated for a defined pH ($\Delta T = T_C - T_A$ with $T_A$ and $T_C$ corresponding respectively to the intersection of the tangents A and C with B). The settling velocity corresponds to the ratio $L/\Delta T$.

In this study, the change in the settling velocity of the aluminum trihydroxide was measured in the presence/ absence of two insoluble impurities: ferric oxide and titanium oxide. The samples were prepared in such a way that the solids analyzed were always higher than 2% v/v as recommended by Vergouw *et al.* (1998). Aluminum trihydroxide was ultra sonicated in distilled water before mixing with the impurities in order to remove any adhering fines. The experimental conditions are tabulated in Table 3.2.

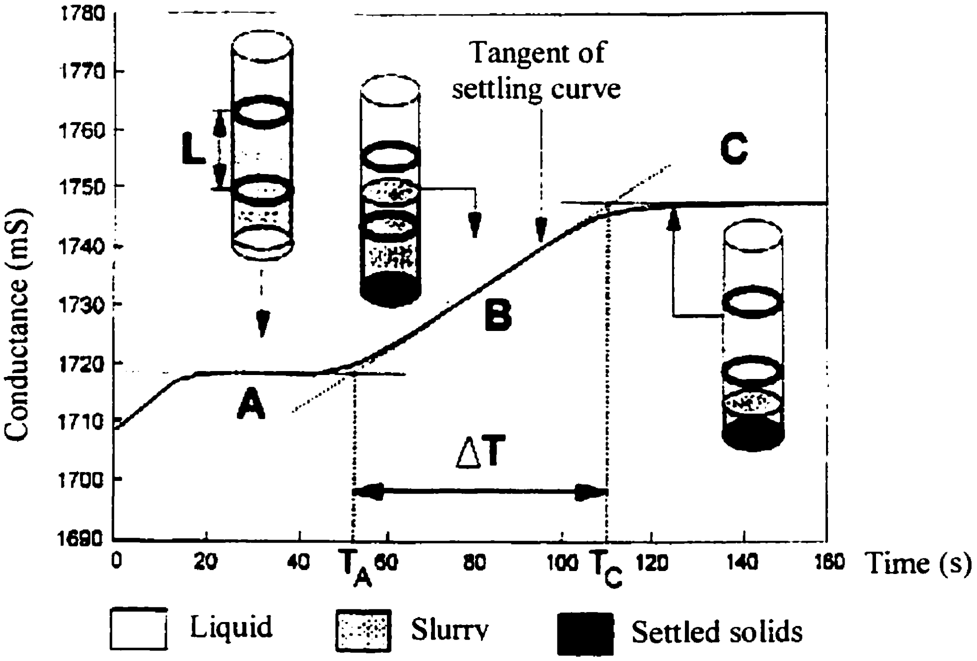

**Figure 3.5:** Deriving settling velocity from settling curve (Vergouw *et al.*, 1998).

**Table 3.2:** Mineral mixing conditions. Background electrolyte 500 mL $10^{-2}$ M KCl.

| **Conditions** | | |
|---|---|---|
| **Fine** | **Mixing time (minutes)** | **Settling time (minutes)** |
| **Single** | | |
| $Fe_2O_3$ | 5 | 5 |
| $TiO_2$ | 5 | 5 |
| $Al(OH)_3$ Coarse (-45 μm) | 5 | 5 |
| **Mixed** | | |
| $Fe_2O_3$ + $Al(OH)_3$ Coarse (-45 μm) | 5 | 5 |
| $TiO_2$ + $Al(OH)_3$ Coarse (-45 μm) | 5 | 5 |

# CHAPTER 4

# RESULTS AND DISCUSSION

This chapter consists of seven sections. In the first section, the results of the preliminary experiments regarding the reactor set up and the analysis of the aluminum trihydroxide are presented. In the second section, the results of the reference case are discussed in order to present the main parameters used in the third and fourth sections. The effect of the temperature and of the initial A/C ratio on the $Al(OH)_3$ crystals are investigated, in the third and fourth sections, respectively. In the fifth section, impurities ($TiO_2$ and $Fe_2O_3$) were added to the mother solution to study their influence on the $Al(OH)_3$ crystals. In the last two sections of the chapter the morphology and the various growth mechanisms of the crystals are presented in detail.

## *4.1 Preliminary experiments*

### 4.1.1 Determination of impeller speed and sampling position in a batch reactor

The minimum impeller speed and sampling position required for homogeneous suspension were determined experimentally. An attrition test (section 3.1.4) was performed at the stirring speeds from 100 rpm to 450 rpm. The seed crystals (100 g/L) were suspended in the glycerol-water mixture for a period of 24 hours. For an impeller speed below 300 rpm, negligible attrition was observed in the tank when the initial and the final particle size distributions were compared. Figures 4.1 and 4.2 show the variation of the crystal size distribution between two different speeds: 300 rpm and 400 rpm. At the higher speed, there was more breakage and attrition of the crystals. This resulted in a reduction of the crystal sizes. Comparing Figure 4.1 to Figure 4.2, region (1) shows the size decrease of the big crystals from 60 to 50 μm while the region (2) shows an increase in the amount of small crystals. This was confirmed by SEM image analysis of the crystals. Below a speed of 300 rpm, no noticeable change in the crystal shape was observed. Thus, it was concluded that stirring at a speed below 300 rpm had a negligible effect on the crystallization process.

Different concentrations of $Al(OH)_3$ seed (from 10 g/L to 100 g/L) were suspended in the glycerol-water mixture. All the samples were taken with a 10-ml pipette at the same depth in the solution. Figure 4.3 illustrates the homogeneous suspension of the different seed concentration for 300 rpm. In this figure, the maximum variation on the slurry density obtained at 100 g/L was 9% with respect to the expected value, which was the mass of $Al(OH)_3$ seed added per volume liquid. The measurement of the slurry density is thus unaffected by the concentration of particles.

For the stirring speeds where the attrition was minimal (less than 300 rpm), an experiment was performed to determine the precision of the sampling position. Samples from different positions in the reactor were taken to define the best position for the sampling and to confirm the homogeneous dispersion of the slurry in the reactor.

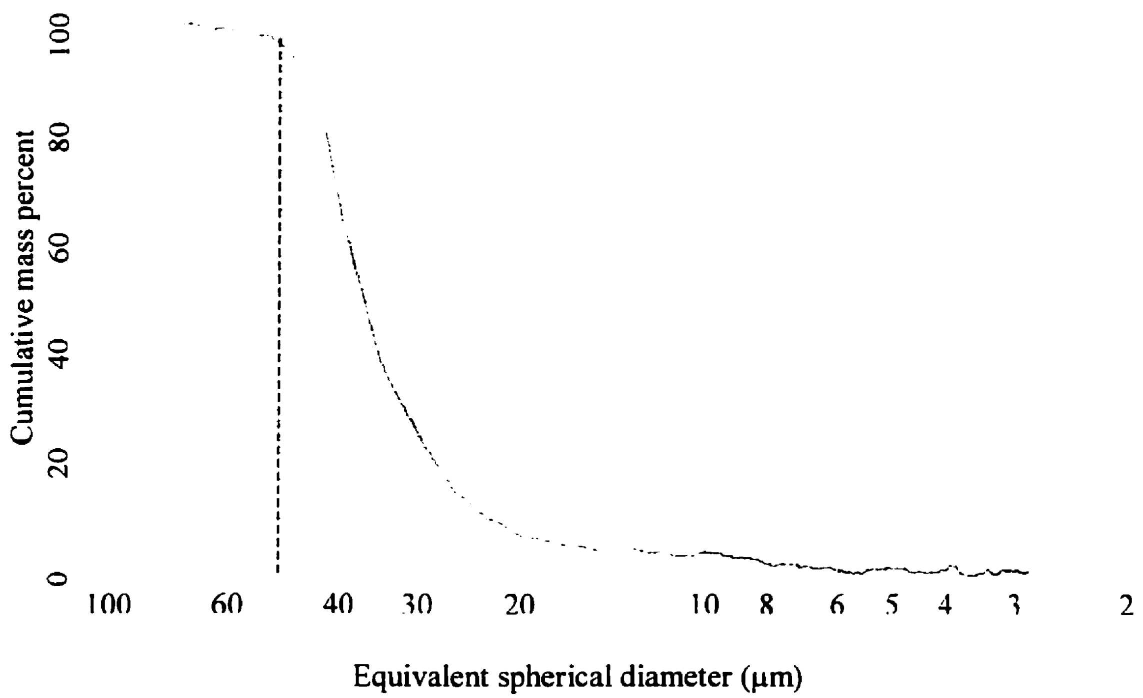

**Figure 4.1:** Crystal size distribution of the aluminum trihydroxide particles with minimal effect of the attrition for a stirring speed of 300 rpm.

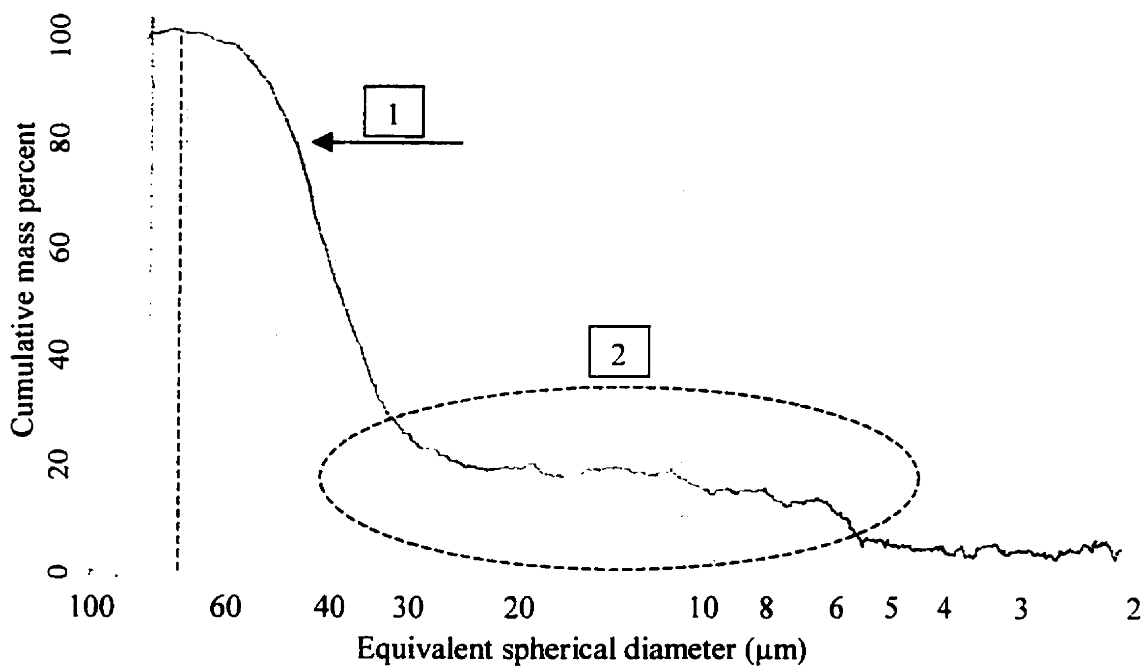

**Figure 4.2** Crystal size distribution of the aluminum trihydroxide particles with apparition of the attrition for a stirring speed of 400 rpm.

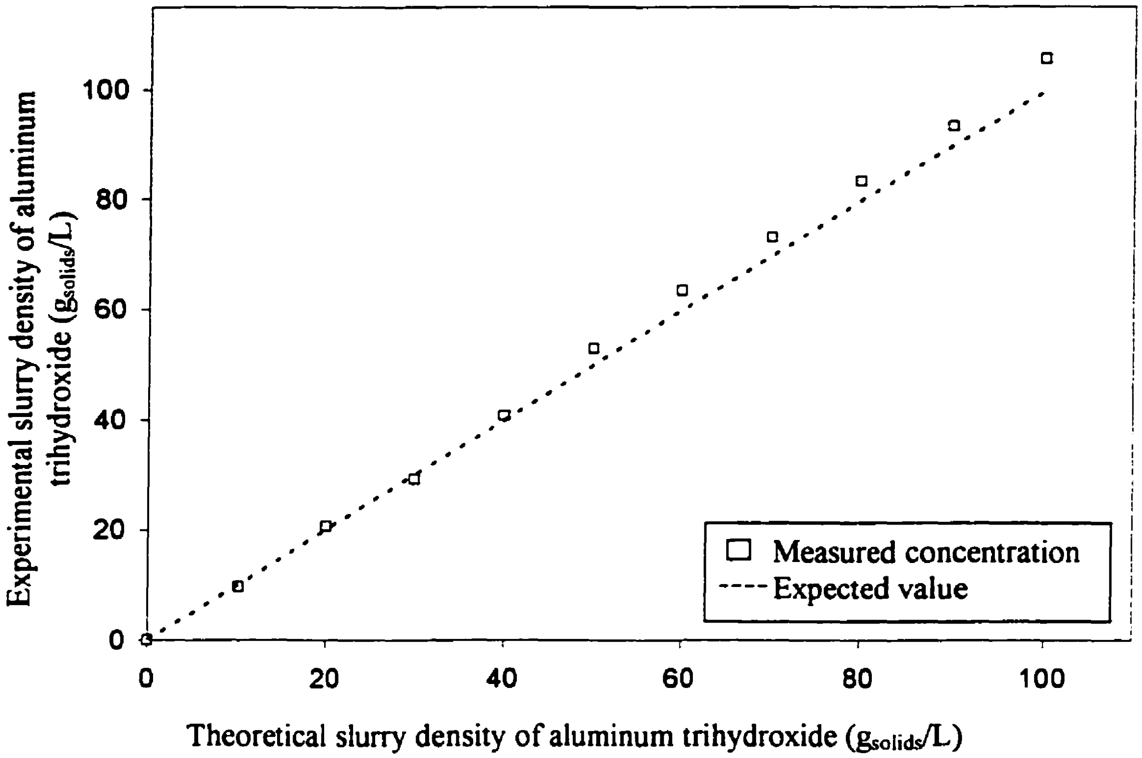

**Figure 4.3:** Representation of the consistent slurry density in a reactor stirred at 300 rpm.

Three positions were defined at two opposite sides in the vessel as shown in Figure 4.4.a: two at the Top (1&2), two in the Middle (3&4), and two at the Bottom (5&6). The error for a fixed slurry density (100 g/L) measured as a function of the sampling position is plotted in Figure 4.4.b. On this figure, the uncertainty on the slurry density of each sampling position (Top, Middle, and Bottom) was represented. The sampling in the middle position resulted in the most consistent slurry densities. It was subject to less variation compare to the bottom and top positions at which the errors are higher. As shown in Figure 4.1 at the speed of 300 rpm, no significant variation of the crystal size distribution was detected.

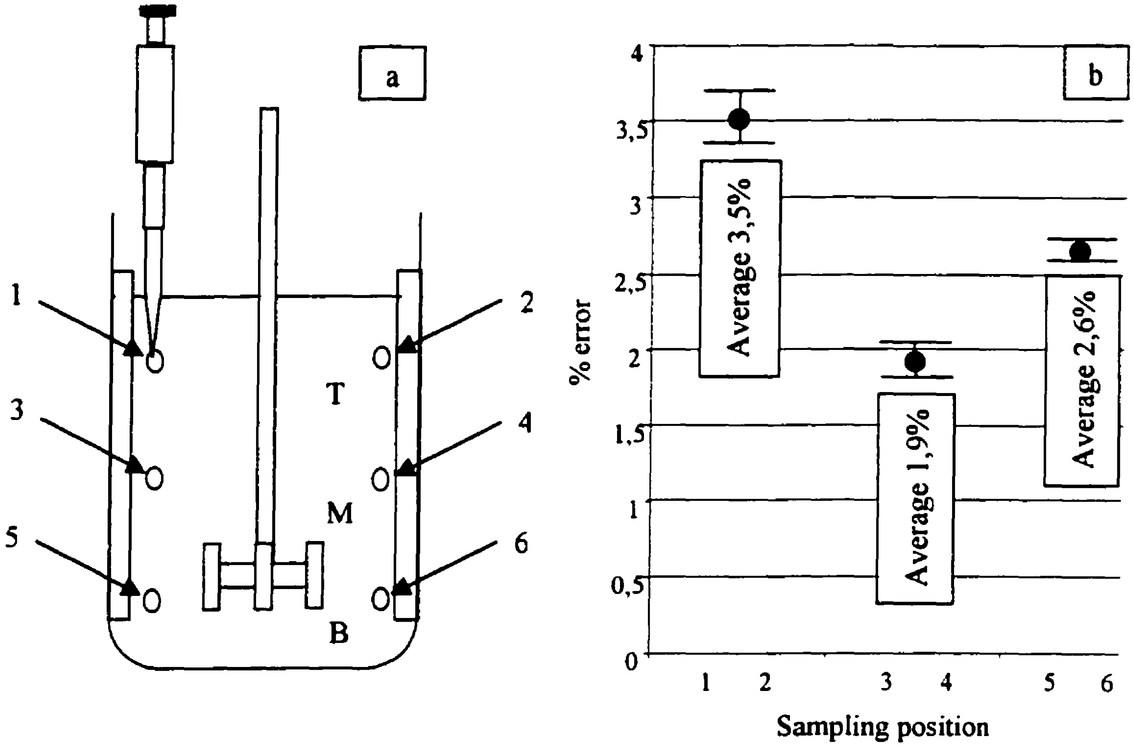

**Figure 4.4:** Reproducibility of the slurry density as a function of the sampling position (Experiences realized with an $Al(OH)_3$ charge of 100 g/L ).

### 4.1.2 X-ray diffraction of the aluminum trihydroxide

X-ray diffraction analyses of all precipitated products were performed to establish their crystallographic characteristics and categorize the polymorphs of aluminum trihydroxide. As was shown in Figure 1.2, only gibbsite and bayerite can be produced by crystallization at the experimental temperatures. The x-ray analysis was performed on the precipitated products crystallized at various temperatures, $Al_2O_3/Na_2O$ initial ratios and amount of impurities. The spectra revealed that only gibbsite was present in all cases.

Figure 4.5 shows typical x-ray diffraction spectrum of gibbsite obtained after 24 hours in the seeded reference case (section 4.2). This spectrum was obtained for a range of angles (2Θ) between 0 to 100°, corresponding to the maximum angle deviation of the apparatus. The results indicated sharp and narrow diffraction peaks expected for a crystalline $Al(OH)_3$, regardless of the precipitation time or the nature of the particle surface features. The dashed line (line 1 in the Figure) delimits the background noise as given by the x-ray diffraction software. The sharp peak denoted as (2) is also believed to be a part of noise due to its narrowness. The peaks with star symbols identify the characteristic angles of gibbsite. These angles are listed in Appendix C. The pattern of the crystals from the reference case matches the spectrum of a synthetic gibbsite produced by Matheson *et al.* (1998) confirming the presence of synthetic gibbsite. The spectrum for a synthetic gibbsite precipitated from hot sodium aluminate solutions produced by Stumpf

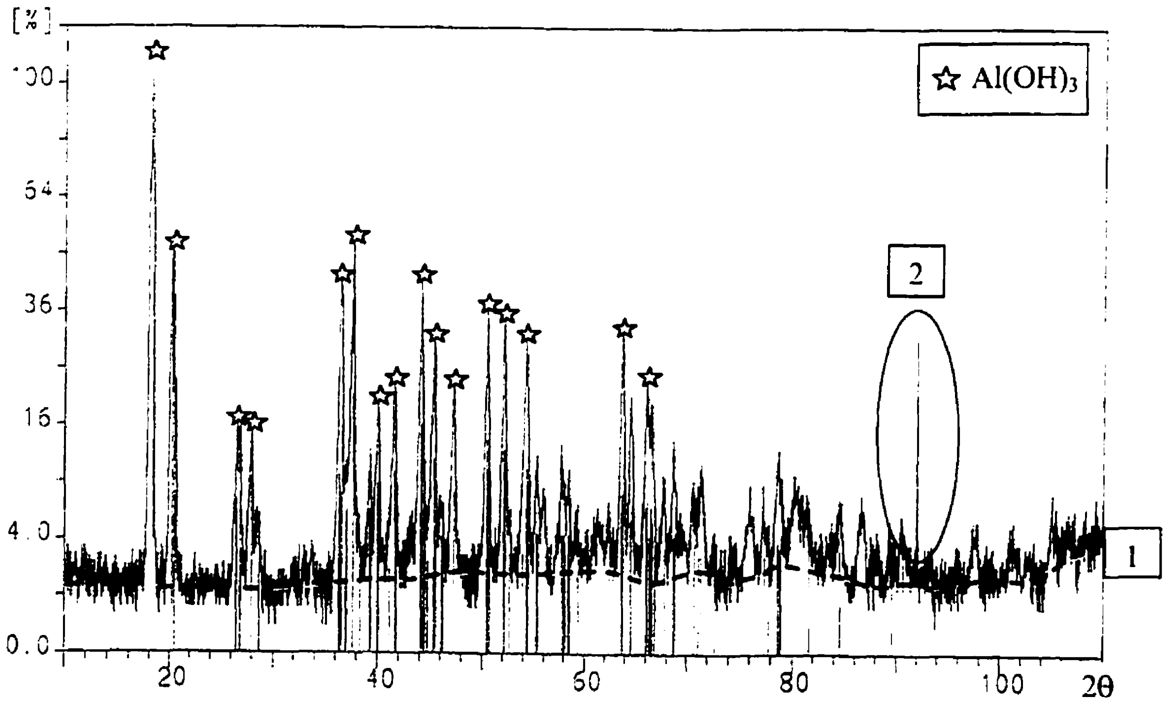

**Figure 4.5:** Spectrum of a precipitate obtained after a 24 hours experiment (temperature of 60°C and an initial A/C ratio of 1.38).

(1998) also corresponds to the spectrum of this sample (see Appendix C). This agrees with the fact that the crystals were formed in a synthetic solution.

While gibbsite was the only polymorph of $Al(OH)_3$ produced in these experiments, some impurities were also detected in the crystal samples. Despite the repeated washings, the precipitates contained the impurities added intentionally ($TiO_2$ and $Fe_2O_3$) at the beginning of the experiment (section 4.5). Also the sodium from the mother liquor was not detected by the x-ray diffraction. The amount of soluble sodium salt (concentrated on the surface of the crystals) and bound sodium (at the interior of the crystal) was not sufficiently high in the analyzed samples.

The polymorphs of aluminum trihydroxide and the main impurities ($TiO_2$, $Fe_2O_3$ and some sodium salt) can be defined by main diffraction angles with a high intensity. In the case of the crystals produced in the presence of ferric oxide, as shown in Figure 4.6, three additional angles appear: one small, at an angle around 22°, and two major at 33°~35° and at 50°~54° $2\theta$. Most of the important diffraction angles for gibbsite are below 55°. The presence of ferric oxide in the crystals was also confirmed by the red color of the $Fe_2O_3$ embedded in the crystals.

As the main diffraction angles of the compounds are between 15° and 55°, reduced spectra between these angles were studied to shorten the time of analysis. Figure 4.7 shows the spectrum of aluminum trihydroxide with no impurities added in this range. In comparison, the crystals produced in the presence of $TiO_2$ showed the distinct $TiO_2$ peaks at 25° and 32° ($2\theta$) (Figure 4.8).

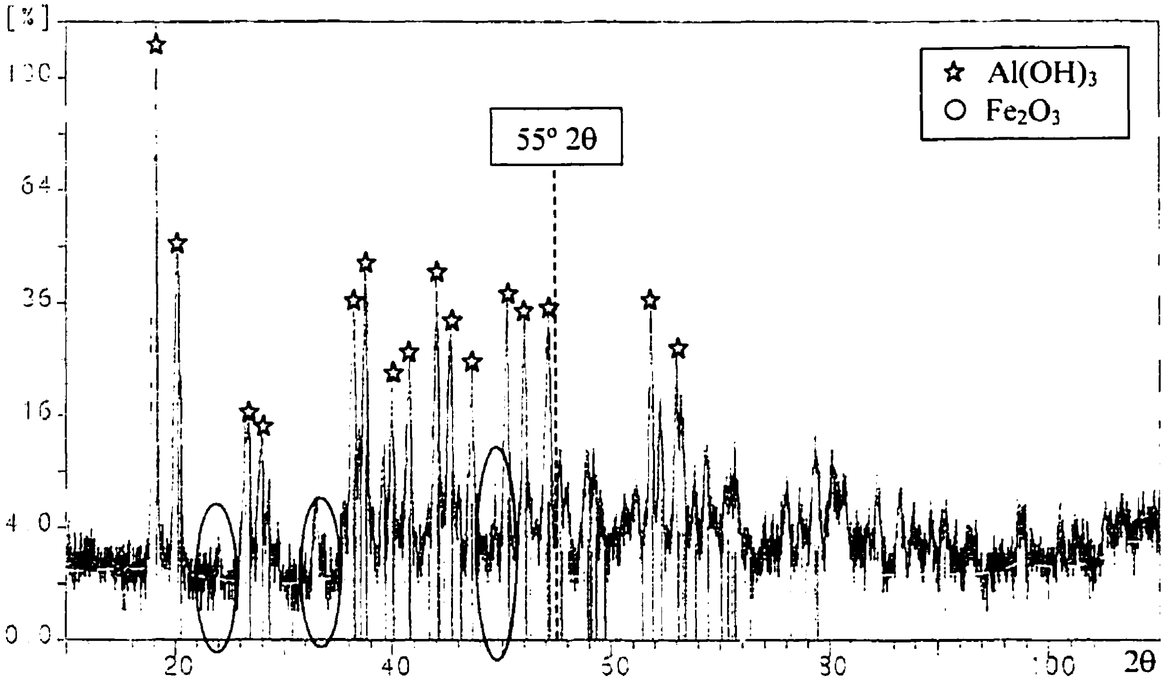

**Figure 4.6:** Spectrum of gibbsite precipitated with 0.7 g/L of iron oxide as an impurity (temperature of 60°C and an initial A/C ratio of 1.23).

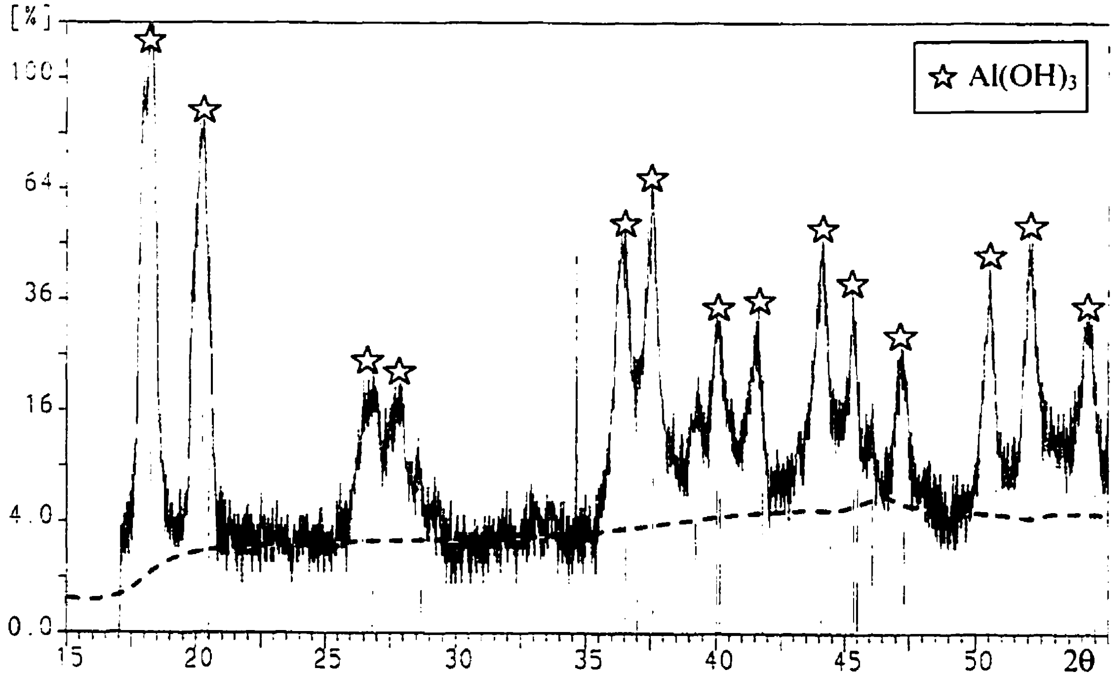

**Figure 4.7:** Reduced spectrum of gibbsite obtained after a 24 hours experiment (temperature of 45°C and an initial A/C ratio of 1.38).

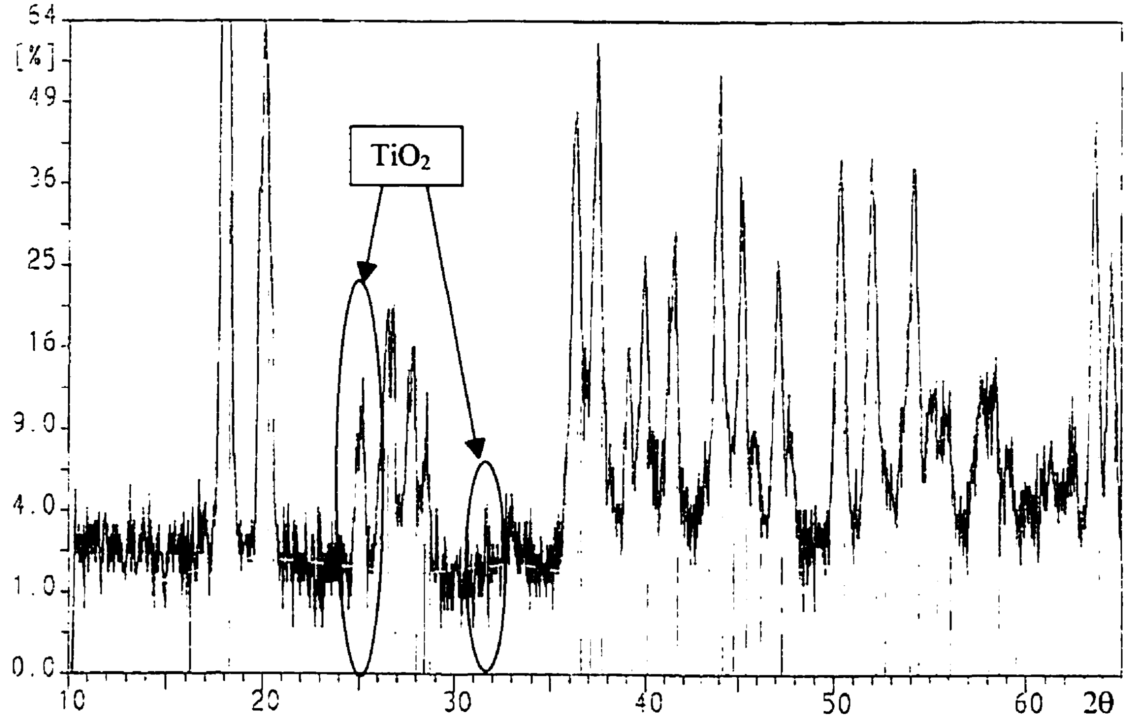

**Figure 4.8:** Spectrum of gibbsite grown in presence of $TiO_2$ (0.1 g/L of $TiO_2$, temperature of 60°C and an initial A/C ratio of 1.31).

### 4.1.3 Sodium residual

The presence of soluble sodium in the samples, prepared for image analysis, affects the crystal morphology during the drying procedure (Figure 4.9.a). The evaporation of water concentrates the sodium dissolved in the solution. Branch crystals are formed with a typical fractal shape and a sodium shell is observed on the dry crystals. In order to remove all soluble sodium material from the crystal/ liquid samples (i.e., below a detectable limit), a test was conducted to determine the number of washing necessary before the drying. For this test, two sizes of defined particles were selected: one with a diameter smaller than 11 μm and the other with a diameter around 100 μm. A given amount of these particles (100 g/L) were suspended in a 30 g/L sodium solution. A sample of 30 ml of this mixture was centrifuged. After the first washing, 750 ppm of sodium for the case of small particles and 633 ppm for the bigger particles were detected by the atomic absorption. Six consecutive washings were performed and the sodium content was plotted in Figure 4.10. The sodium concentration after first washing is not plotted on the figure to scale up the lower concentration range. At least five washings were found to be necessary to have the minimum amount of sodium in the solution. After five washings, the crystal surface was clean giving SEM images of a good resolution (Figure 4.9b). The detection of the sodium concentration below 5 ppm was difficult since the distilled water used for the washing contained some amount of sodium; also, the atomic absorption apparatus was not sensitive below this lower limit of 5 ppm.

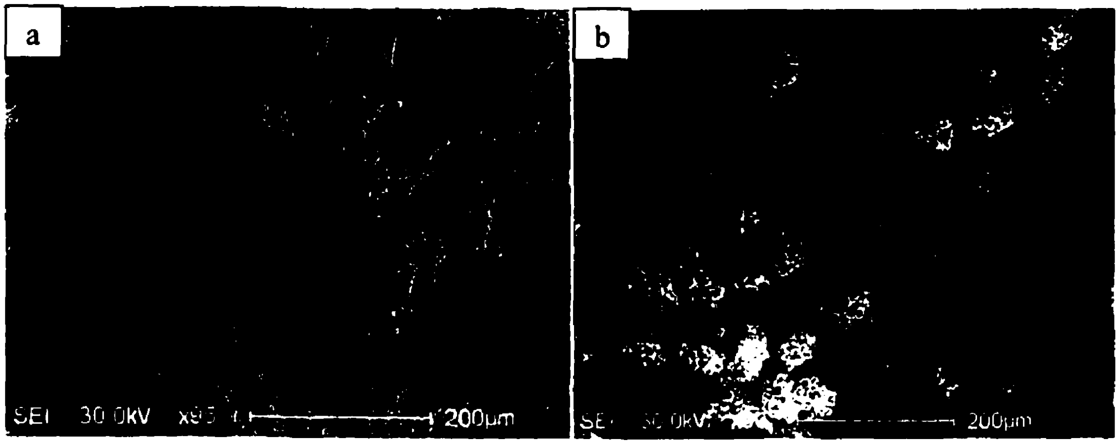

**Figure 4.9:** (a) Sample containing sodium, (b) Clean sample: the particles are well defined.

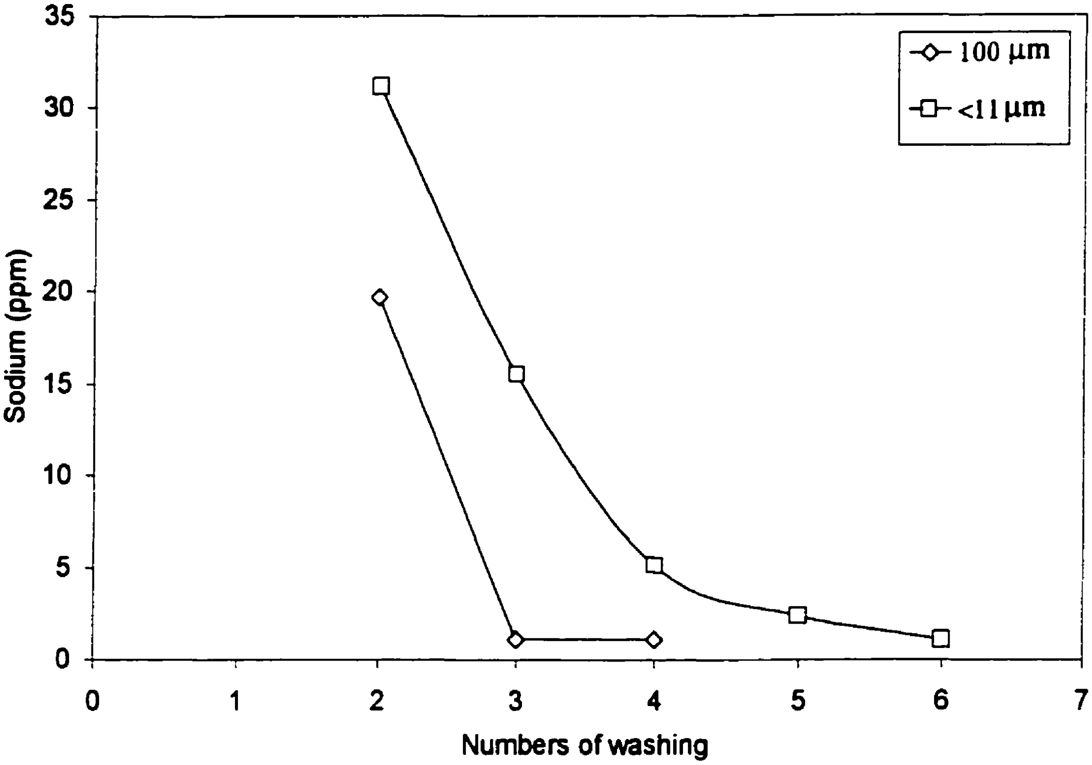

**Figure 4.10:** Effect of the size of the $Al(OH)_3$ particles on the removing of the sodium.

## *4.2 Reference case*

### 4.2.1 $Al_2O_3/Na_2O$ ratio

The results presented in this section were obtained from the experiment carried out at 60°C, and initial aluminum and sodium hydroxide concentrations of 29.43 g/L and 52.33 g/L respectively. The soluble concentrations, reported here, are calculated from the atomic absorption analysis of the mother solution. These conditions of temperature and concentration were chosen as representing typical industrial crystallizer conditions.

The results for the soluble concentration of aluminum and sodium can be combined by showing the change in the weight ratio of aluminum to the sodium expressed as the concentration ratio of $[Al_2O_3]/[Na_2O]$(Appendix A). This A/C ratio of aluminum to sodium dissolved in the solution will be used in all this study. Following this notation, the reference case corresponds to an initial A/C ratio of 1.38.

In most experiments carried out at high temperature, the concentration of sodium showed an increase although sodium was inert in the solution and its concentration was supposed to be constant. The observed increase in the concentration was related to the water loss due to evaporation, even if some sodium can be bound at the core of the $Al(OH)_3$ crystals (Patnaik and Vidyasagar, 1998). This effect of evaporation was corrected using a mass balance of the soluble sodium, as shown in Appendix B. The concentration of aluminum and the particles (i.e. slurry density) were appropriately adjusted accordingly to the evaporation effect and the A/C weight ratio was calculated using the estimated concentration of aluminum and by assuming that the sodium concentration was constant at its initial value.

Figure 4.11 shows the decrease of the weight ratio of $[Al_2O_3]/[Na_2O]$ during the precipitation for the reference solution. After seeding the solution at time 0, the crystallization started immediately with no primary nucleation. At the end of the experiment, 24 hours later, the A/C ratio approached a plateau. Due to the reduction in the concentration of aluminum and thus a lower A/C ratio, the crystal growth rate was slow resulting in a low rate of decrease in the soluble aluminum concentration. Also shown in the Figure is the equilibrium A/C ratio for the condition defined using the model developed by Misra (1970) (Equation 3). As observed, the equilibrium A/C ratio was constant because all parameters of the Misra equation (temperature and caustic concentration) were maintained constant.

The difference between the equilibrium A/C ratio curve and the reference A/C ratio curve represents the driving force for the crystallization. As shown in Figure 4.11, the highest driving of the crystallization process was at the beginning of the reaction. As the driving force decreased, the crystallization rate decreased and a slow growth rate of the crystals took place (confirmed later by the analysis of the slurry density). At the end of the 24 hours period, the difference between the equilibrium A/C ratio and the reference A/C ratio was only 0.3, 85% less than the initial driving force. These results correspond to the findings described by Veesler and Boistelle (1993).

### 4.2.2 Supersaturation

A different and more conventional way of depicting the driving force is by plotting the supersaturation (Figure 4.12), which is defined as:

$$S=R/R_{eq} \tag{4}$$

where R is the A/C ratio at any time and $R_{eq}$ is the equilibrium A/C ratio.

The advantage of S was to remove the small variations of the equilibrium ratio induced by the sodium concentration and by the variation of the temperature.

Figure 4.13 illustrates the expected interrelation between the decrease of the supersaturation in the solution and the increase of the slurry density (particle concentration), during the crystallization of the $Al(OH)_3$ in the reactor.

As shown in this figure, the curve of the supersaturation in the solution and the curve of the slurry density can be separated into three phases. The lag phase can be induced either by low supersaturation or by an insufficient seed. In the Figure, during the first six hours corresponding to the lag phase, the slurry density was constant with a small variation of only 2.5%. This plateau is related mainly to insufficient seed. However, in this particular case, it is also partially due to the uncertainty in the method for the measurement of the slurry density, having a relative small value (sampling of 0.08 grams of small particles can be corrupted by the soluble sodium not removed from the surface, as explained in section 4.1.3). The second phase is characterized by a fast increase in the slurry density and decrease in the supersaturation. This is caused by the increase in the surface of the produced crystals promoting nucleation and growth. Finally, in the third phase, the crystallization slows down due to the depletion of aluminum from the solution.

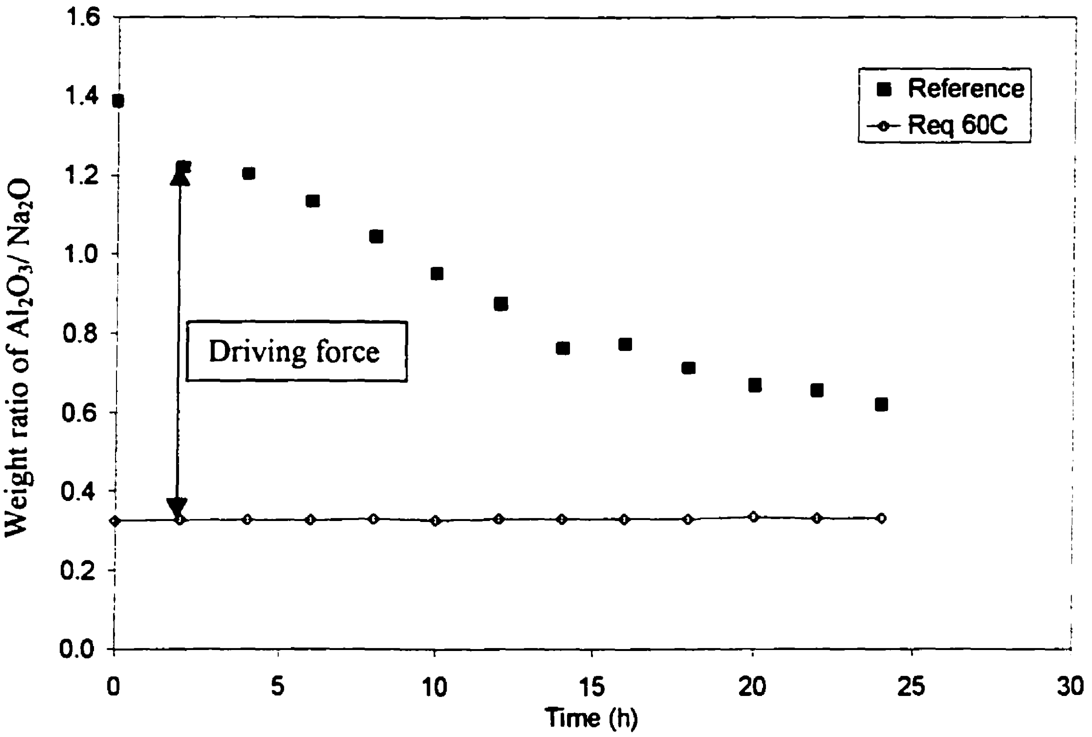

**Figure 4.11:** Decrease of the dissolved aluminum concentration in the caustic solution, expressed by the ratio A/C, during the precipitation process (temperature of 60°C).

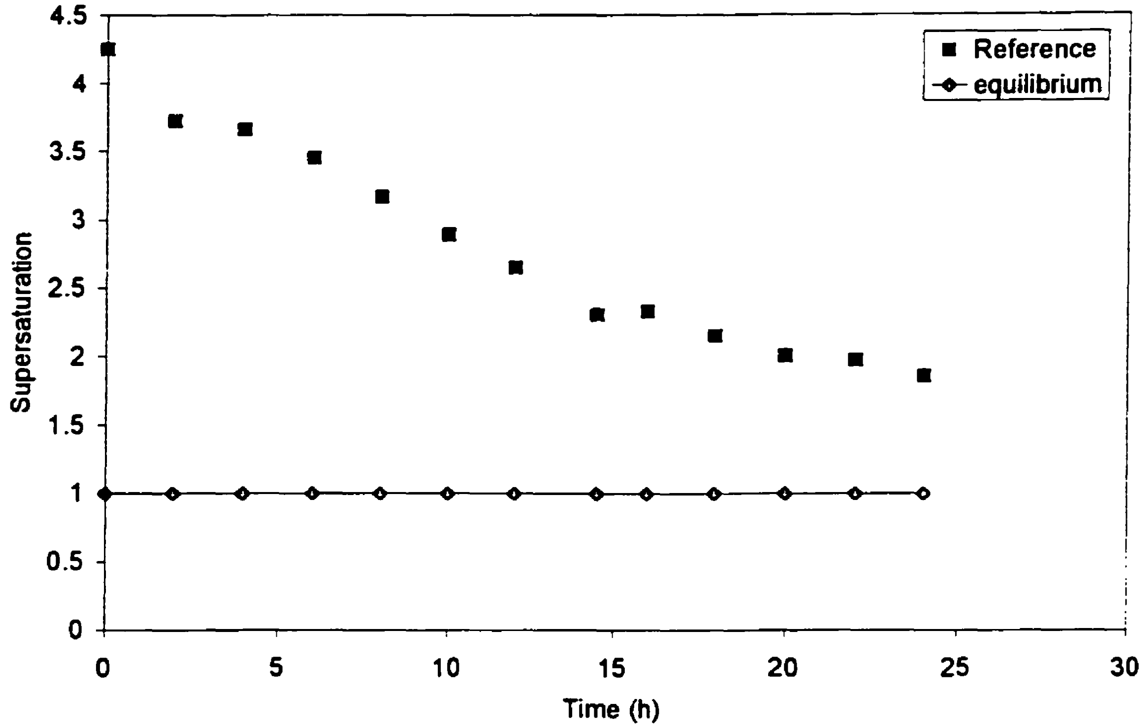

**Figure 4.12:** Decrease of the supersaturation and stability of the equilibrium value (temperature of 60°C).

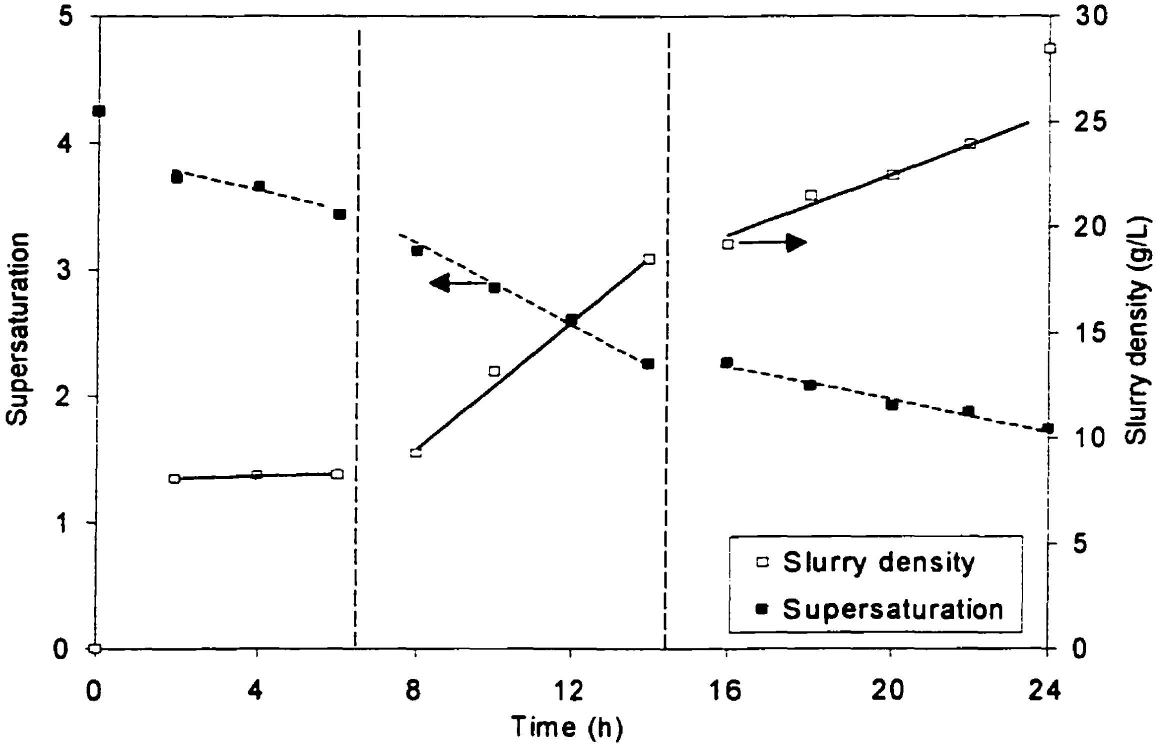

**Figure 4.13:** Interrelation between the [Al] dissolved (expressed by the supersaturation) and the slurry density (i.e. particles concentration) during the crystallization process.

### 4.2.3 Morphology

Some SEM images of $Al(OH)_3$ produced in the solution during the experiments are illustrated in Figure 4.14. Particles obtained after 2 hours during the lag phase and after 24 hours at the end of the experiment are shown. As observed in Figure 4.14, the agglomerate and the crystals formed on the particles after 2 hours (Figures 4.14 c and e) are smaller than those obtained after 24 hours (Figures 4.14 d and f). The first hours of the experiment correspond to a fast production of crystals favored by the high amount of dissolved aluminum. The weight and the surface of the crystals formed during these hours are very small but their total surface offers a large surface for the growth and secondary processes (like agglomeration). Thus, fast growth and nucleation rates are taking place generally at the beginning of the experiment (Söhnel and Garside, 1992). However, as observed in Figure 4.14, the particles did not contain a lot of small single crystals. As reported by Scott (1963), while the nucleation and the crystal growth occur at the same time in a reactor, the nucleation is favored by the addition of seed. For a small amount of seed, the nucleation is slow. The amount of dissolved aluminum in the solution decreases mainly due to the crystal growth giving coarser crystals. At the beginning of all the experiments in this study, only 1 g/L of $Al(OH)_3$ seed was added to the supersaturated solution. The small amount of seed used in this reference case was insufficient to initiate the nucleation resulting in the formation of coarser particles, as explained above. Thus, the lag phase observed in the slurry density (Figure 4.13) corresponds to the time necessary to have a primary nucleation as shown in Figure 1.4 section 1.2. Also, as fewer single crystals were formed in this experiment, the total exposed surface of the crystals was less important than expected resulting in a slower decrease of the dissolved aluminum concentration. In this crystallization process, the formation of the agglomerated crystals, which increased the size of the particles, does not affect the dissolved aluminum concentration as much as the growth process. The agglomeration is just a secondary change of the existing crystals.

The detailed characterization of the crystals will be given in the following sections. Note, however, the difference between the Figures 4.14 c and e. In Figure 4.14 c, small crystals appeared on the surface of a large particle, certainly formed from the seed or a secondary change (breakage...), while in Figure 4.14.e the single sharp crystals are agglomerated together.

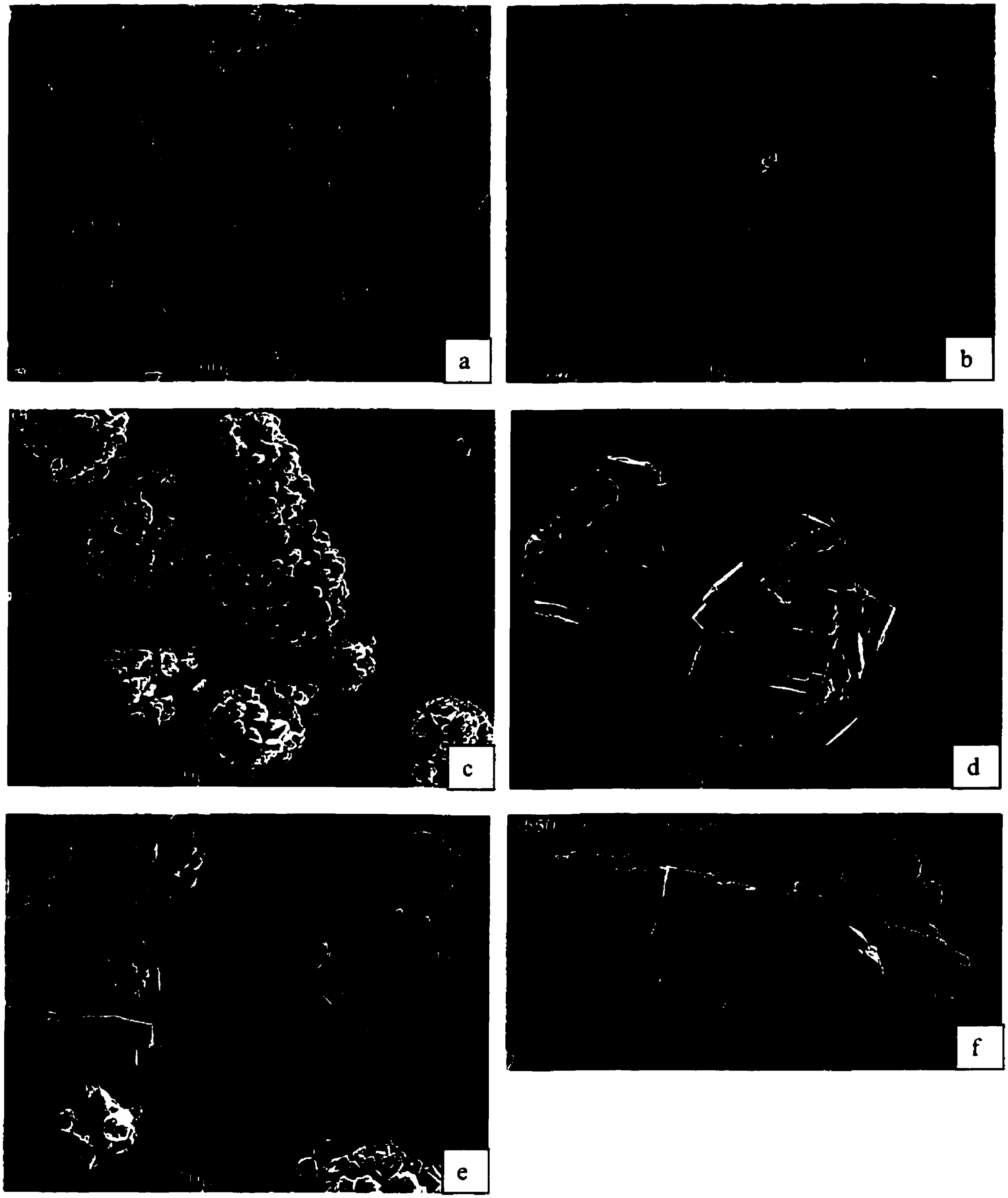

**Figure 4.14:** Shape and growth of the precipitate in the solution (a,c,e) after 2 hours, (b,d,f) at the end of the experiment after 24 hours.

Finally, a mass balance of the system was also calculated for each experiment to detect any imprecision or error in the experimental procedure. All the masses were expressed in gram of elemental aluminum. As illustrated in Figure 4.15, the total amount of aluminum measured at the end of the reference experiment was 27.9 grams. This value represents an uncertainty of 6% compared to the initial amount of aluminum introduced to the reactor. The variation in the mass balance at the beginning of the experiment is due to the imprecision of the slurry density method, as mentioned above.

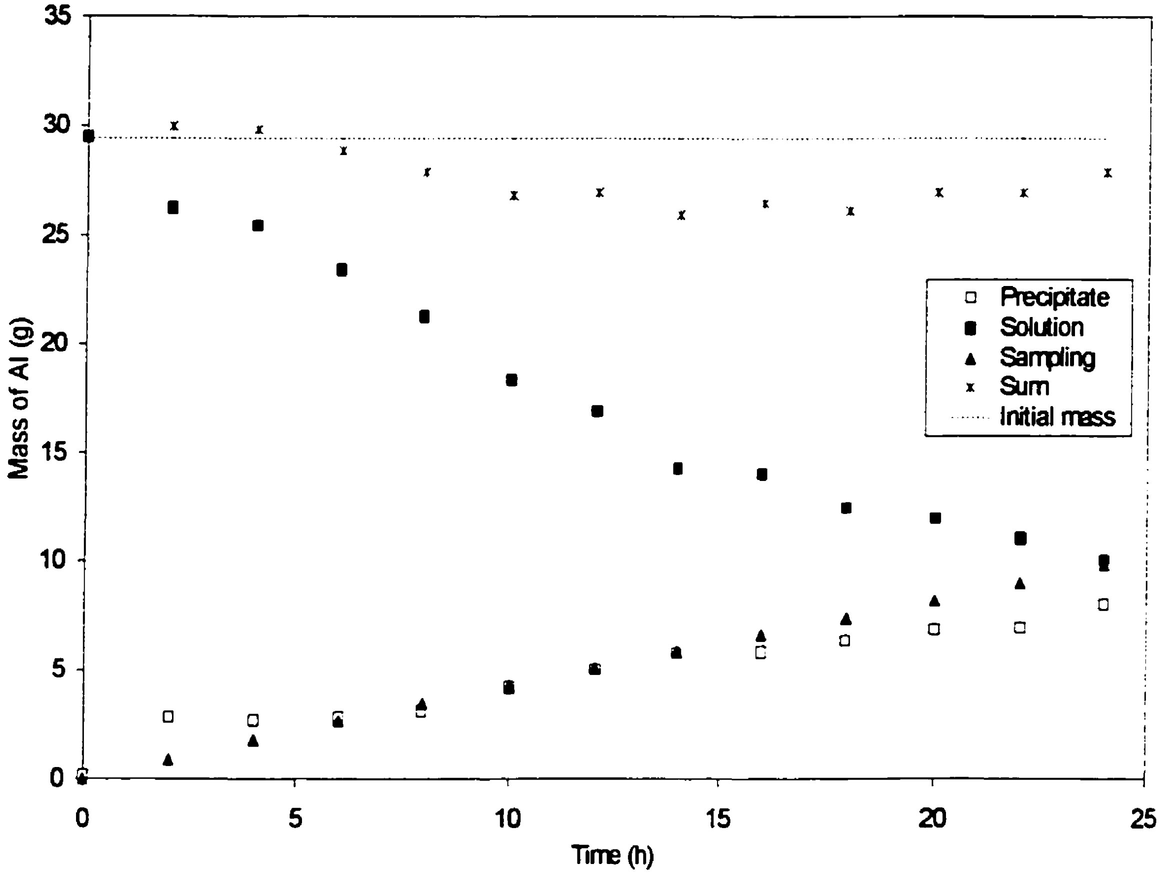

**Figure 4.15:** Mass balance of the aluminum in the reactor for a 24 hours experiment.

## *4.3 Effect of temperature*

### 4.3.1 Evolution of the crystallization in the reactor

The effect of the temperature was studied in the range between 45°C and 80°C, corresponding to the crystallization temperature range in a Bayer plant (Chaubal, 1990).

Figure 4.16 shows that the solubility of aluminum increases with the increase in temperature as reflected by the increasing equilibrium A/C ratio. Thus for a given initial condition, the lower temperature gives a higher supersaturation (driving force) for the crystallization. This curve of the equilibrium A/C ratio was calculated from equation 3, for a fixed sodium concentration of 29.79 g/L (expressed as $Na_2O$).

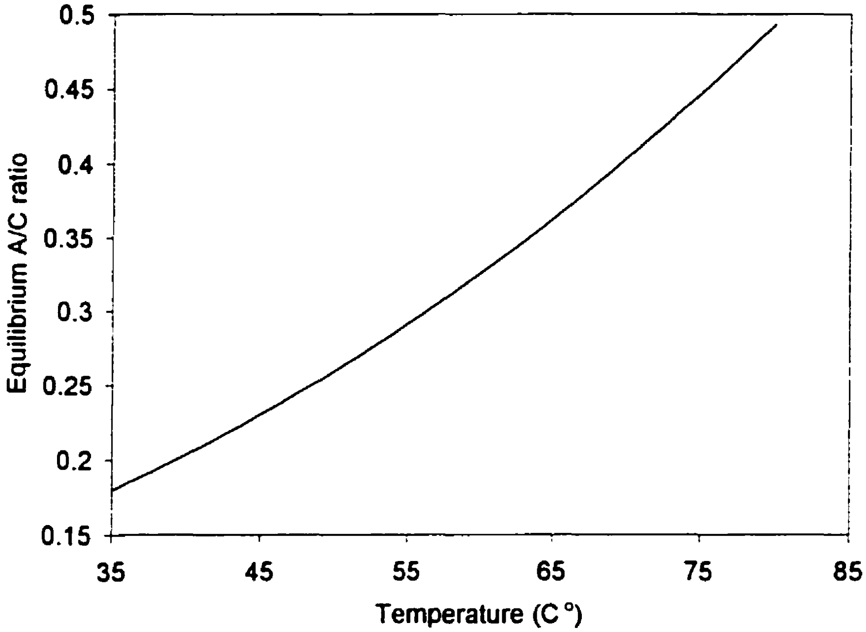

**Figure 4.16:** Effect of temperature on the equilibrium A/C ratio for a fixed concentration of sodium of 29.79 g/L (expressed by $Na_2O$).

Figure 4.17 represents the results obtained for the two extreme temperatures 45°C and 80°C. Also shown in the Figure 4.17 is the equilibrium A/C ratio as defined by Misra

(1970). To avoid any possible variations in the initial A/C ratio, the two solutions were prepared with the same mother solution, and the experiments were run in parallel. The initial concentrations of aluminum and sodium hydroxide were 29 g/L and 54.43 g/L, respectively, giving an initial A/C ratio of 1.3. The A/C ratio at 45°C varied more slowly than that at the higher temperature. For example, the A/C ratio at 45°C decreased by 20% in 15 hours, while the A/C ratio at 80°C decreased by around 45%. After 18 hours, the experiment at 80°C reached a plateau where the A/C ratio varied only by 5% in the last 6 hours of the experiment.

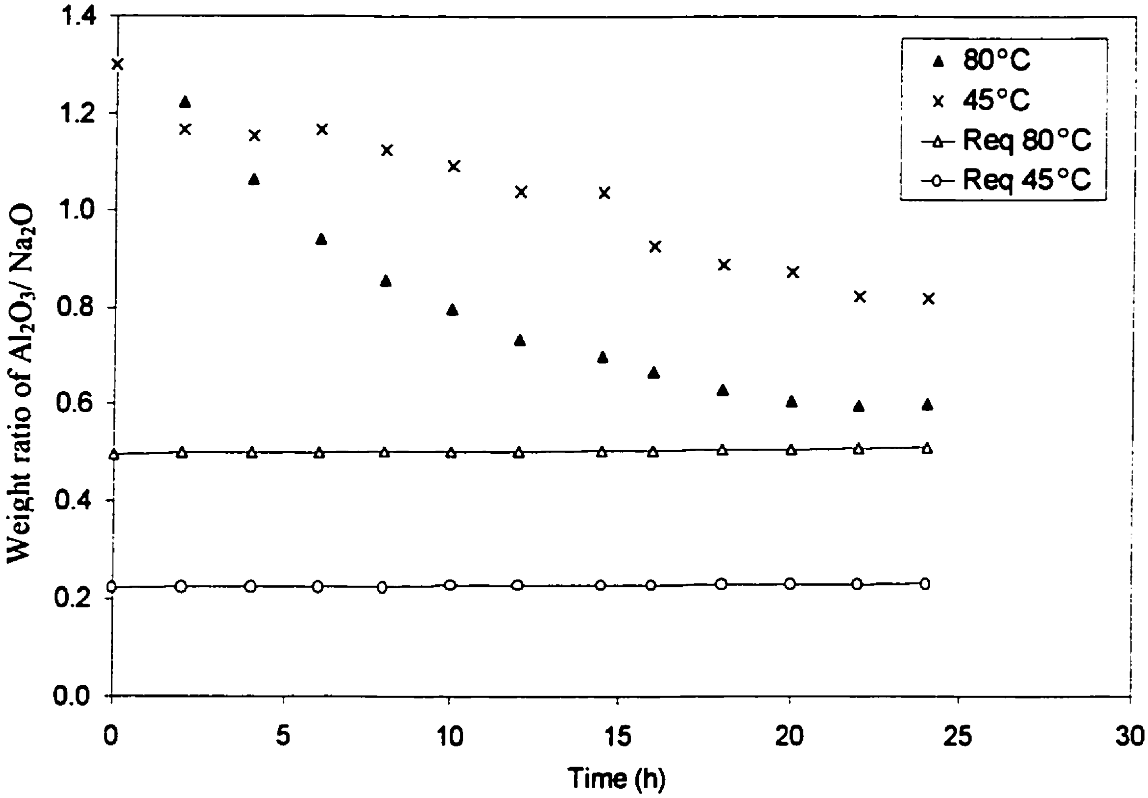

**Figure 4.17:** Influence of temperature on the precipitation process and the equilibrium ratio.

In the case of the experiment performed at 45°C, after 18 hours, the crystallization was not completed. At the end of the experiment, the supersaturation at 45°C was 70% higher than the supersaturation at 80°C.

Based on the results shown in Figure 4.17, Figure 4.18 shows the decrease in the calculated supersaturation for the two temperatures at 45°C and 80°C as well as at 60°C where the initial ratio was 1.38 (reference case). Also, while the supersaturation at low temperature was consistently higher than at the higher temperature, the lower temperature showed a slower rate of crystallization. Clearly, the crystallization process, thermodynamically favorable at low temperature, was kinetically limited. The crystallization rates were faster at higher temperature, but the process was limited by the supersaturation. This is used in the industry to optimize the crystallization process. Batch reactors with different temperature are used in series; the precipitation starts with the reactor having the highest temperature and finishes with the reactor with the lowest temperature to precipitate the maximum amount of aluminum trihydroxide. An example is the process developed by Yamada *et al.* (1982) resulting in an increase in the yield of 5.6% and in coarse grains of $Al(OH)_3$ which have a high resistance to disintegration.

These observations regarding the weight ratio and the supersaturation were consistent with the slurry density of $Al(OH)_3$ in the reactor (Figure 4.19). Although, there is some scatter in the data at 80°C, fewer particles were produced at a low temperature for a specific time than at a higher temperature. The amount of $Al(OH)_3$ produced in 10 hours at the temperature of 80°C was reached in 18 hours at a temperature of 45°C. After

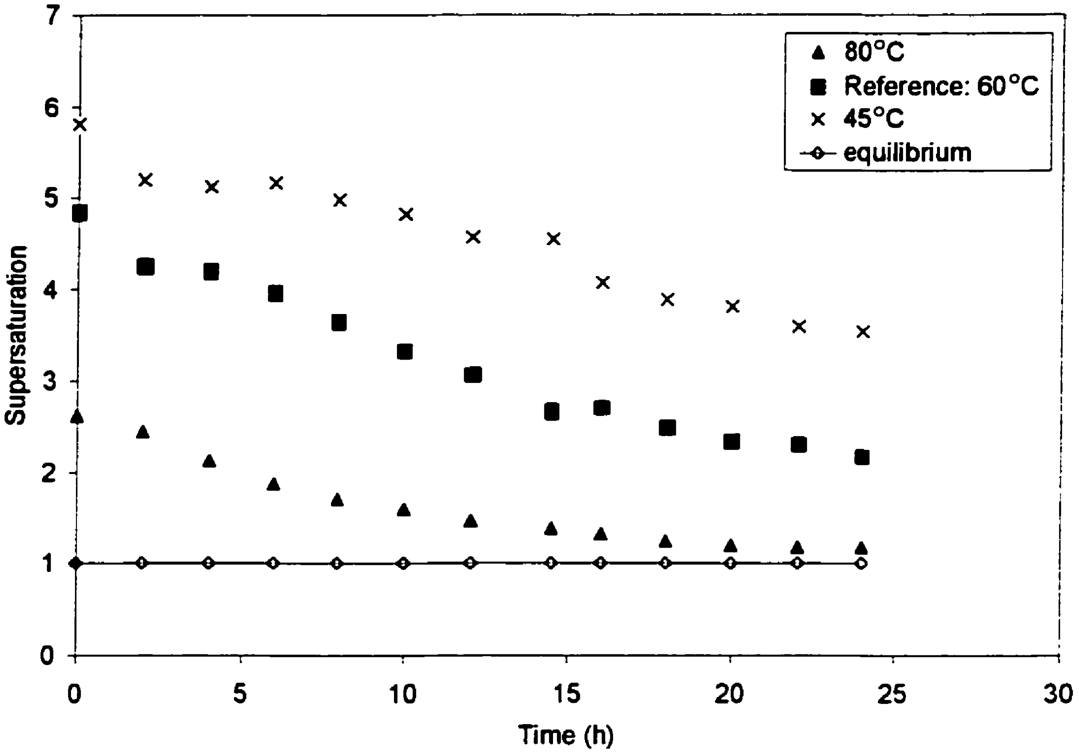

**Figure 4.18:** Effect of the temperature on the supersaturation for a 24 hours experiment.

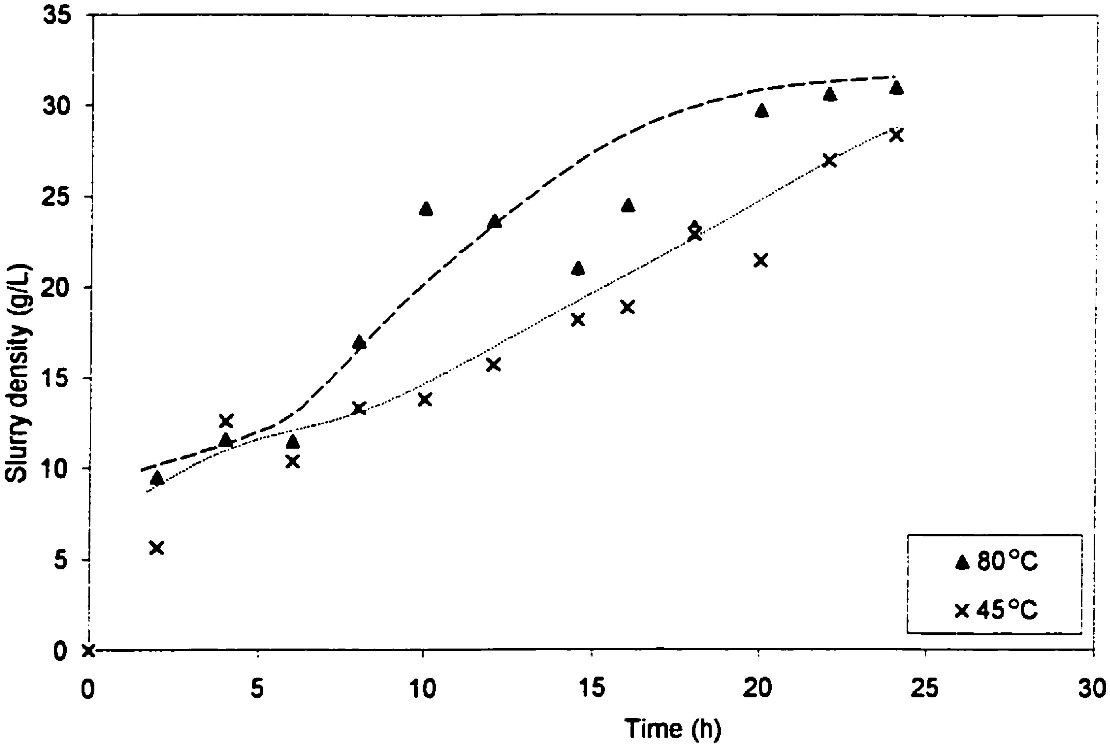

**Figure 4.19:** Increase of the slurry density with the temperature for a 24 hours experiment.

this time, as the weight ratio of the temperature of 80°C reaches a plateau, the differences in the slurry density slowly decreased.

### 4.3.2 Short term increase of temperature

To confirm the effect of the temperature on the crystallization process, an experiment was carried in parallel with the reference case. The same mother solution was used. The temperature was fixed at 60°C and the initial ratio at 1.38. After 4 hours, the temperature was increased to reach 90°C for 2 hours and then was decreased immediatly to 60°C (Figure 4.20). There were no other variations in temperature. Figure 4.20 shows the effect of this temperature step on the A/C ratio. While the two curves followed the same trend, the increase of temperature to 90°C favored the crystallization as shown in the decrease of the soluble A/C ratio. A decrease of 10% in the soluble A/C ratio appeared in two hours as the equilibrium A/C ratio of the step solution was brought back to its original value. Figure 4.21 shows the variation of supersaturation with time. At the end of the temperature step, the supersaturation decreased by 15%. This caused the crystallization of $Al(OH)_3$ and the soluble aluminum was removed from the solution as shown by the decrease in the supersaturation. Figure 4.22 represents the increase in the amount of $Al(OH)_3$ produced. After the step increase in temperature with time at 6 hours, an increase of 70% of the particle concentration was obtained. Furthermore, the same amount of particles was produced in only 16 hours in the step solution instead of 24 hours for the reference.

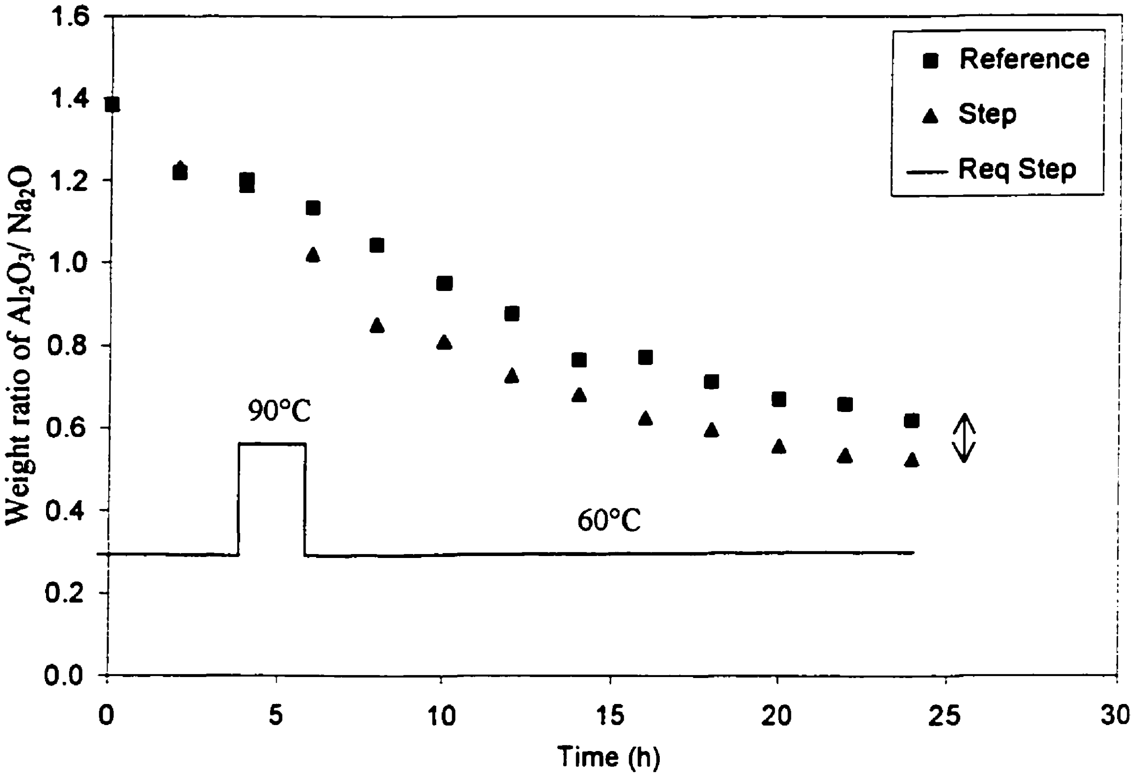

**Figure 4.20:** Effect of a short increase of the temperature on the weight ratio (initial temperature of 60°C).

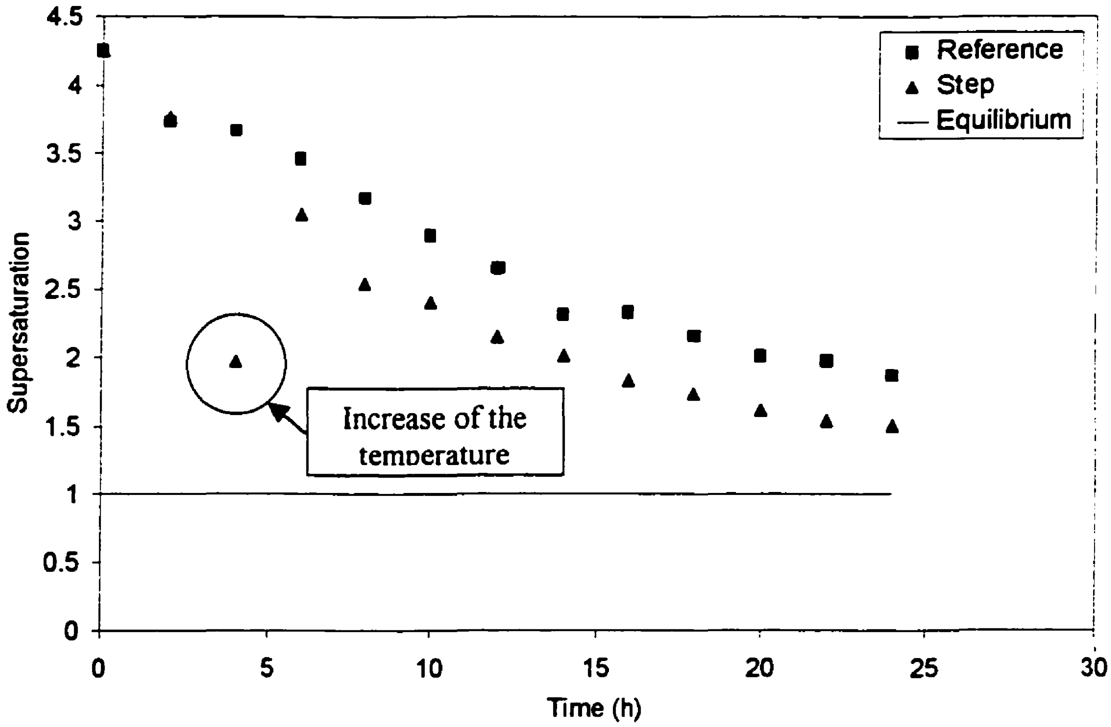

**Figure 4.21:** Effect of a short temperature increase on the supersaturation (initial temperature of 60°C).

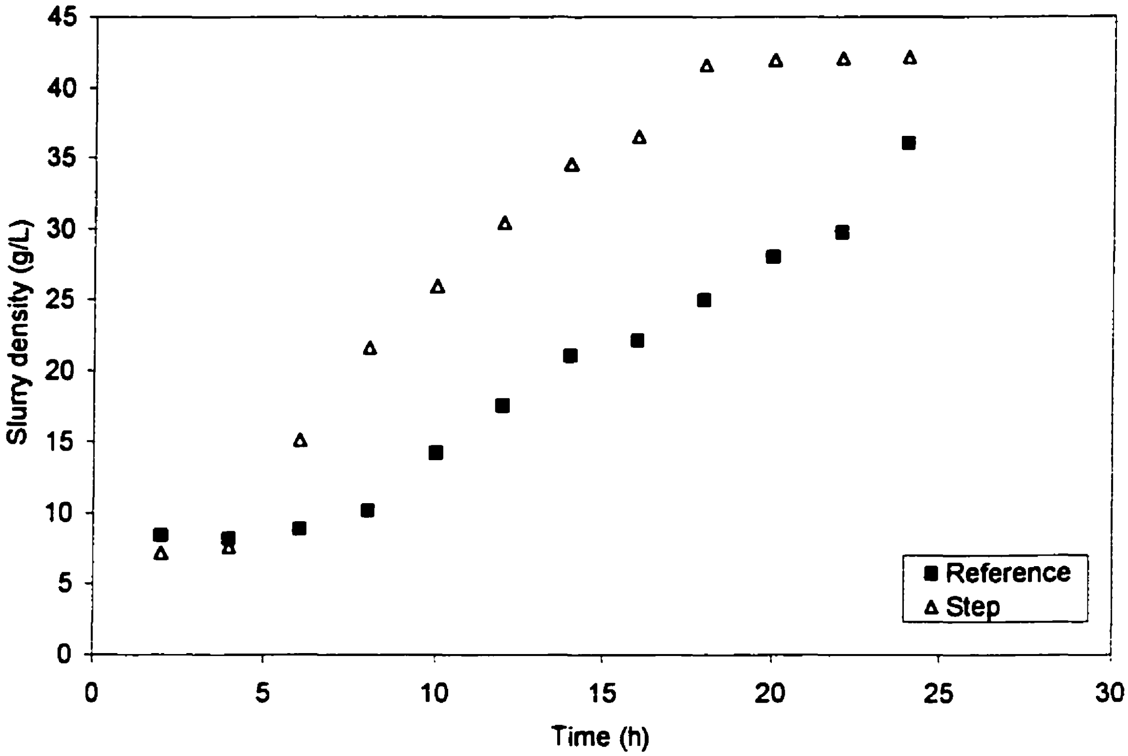

**Figure 4.22:** Augmentation of the slurry density by a short increase of the temperature (initial temperature of 60°C, increase step of 30°C).

### 4.3.3 Image analysis of the $Al(OH)_3$ crystals

Figure 4.23 provides some information on the change in the morphology of the crystals during the temperature step. Six different pictures were taken by a scanning electron microscope: two at a magnification of 80 x to obtain a general view of the precipitate, and four at a magnification ranging from 550 x to 1400 x to study the effect of temperature on the crystals.

As observed in Figures 4.23 a and b, the particles formed in the early stage of the experiment were small. The Martin's diameter of the particles shown in Figures 4.23 b and c varied from 5 μm to 16 μm for the single crystals and the small crystals on the surface of the particle matrix (Figure 4.23 c). The diameter of the larger particles, formed by different crystals (due to agglomeration or growth for example) reached 50 µm. The edge of these crystals was smooth due to the high attrition caused by the small particles. After two hours within which the temperature was increased from 60°C to 90°C, the single crystals showed sharper edges, and the shape became close to a long hexagonal tube. The length and the width of these crystals could reach up to 45 µm and 16 µm respectively (Figures 4.23 e and f). As shown in these two figures, most of the single crystals disappeared and bigger agglomerates were observed. An agglomerate with a spherical shape was also observed in Figure 4.23 f. It is believed that such agglomerate evolved from the earlier particle shown on picture 4.23 c. The crystals formed on its surface, with sharp edges and plane surfaces, were shorter than the new particles formed by the single crystal. The surface area of this agglomerate was thus bigger than the agglomerates formed with bigger single crystals, but its Martin's diameter was in the same order than the single crystal agglomerates.

The different processes of the growth will be discussed in the following section.

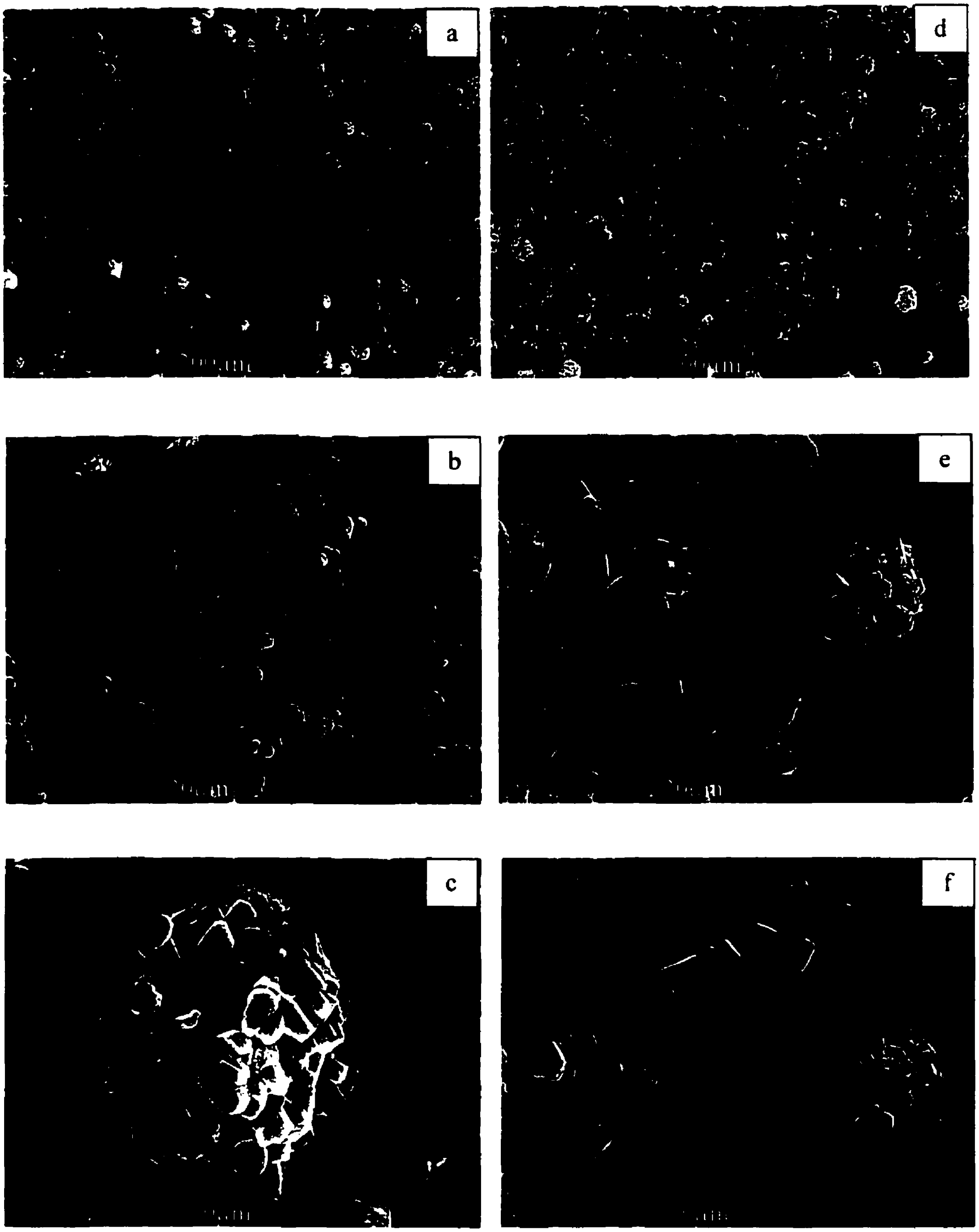

**Figure 4.23:** Influence of an increase of the temperature on the precipitate:
(a), (b) and (c) at initial temperature of 60°C after 4 hours; (d), (e) and (f) after 2 hours at 90°C (6 hours after the beginning of the experiment).

The increase of the size of the particles with the temperature, noticed by the image analysis (Figure 4.23), was correlated by the size distribution of the crystals. As shown in Figures 4.24 a and b, the particle size distribution of crystals produced at 60°C is bigger than those produced at a lower temperature 40°C. The average diameters of the particles formed at 40°C was 28 μm, while at a temperature of 60°C, the average diameter was 66 μm. The particles are smaller at 40°C because at this temperature, the rate of growth was slow. However, the slurry density at the end of these experiments was in the same order confirming that even though the particles were smaller at 40°C, more particles were formed.

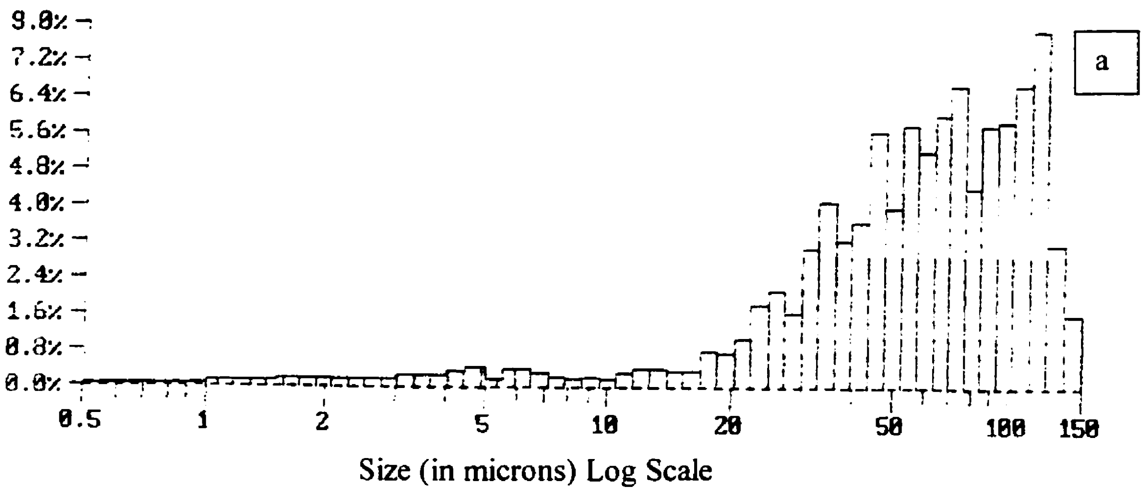

**Figure 4.24 a:** Density chart of the precipitates formed at a temperature of 60°C (initial A/C ratio of 1.38 and precipitation time of 24 hours).

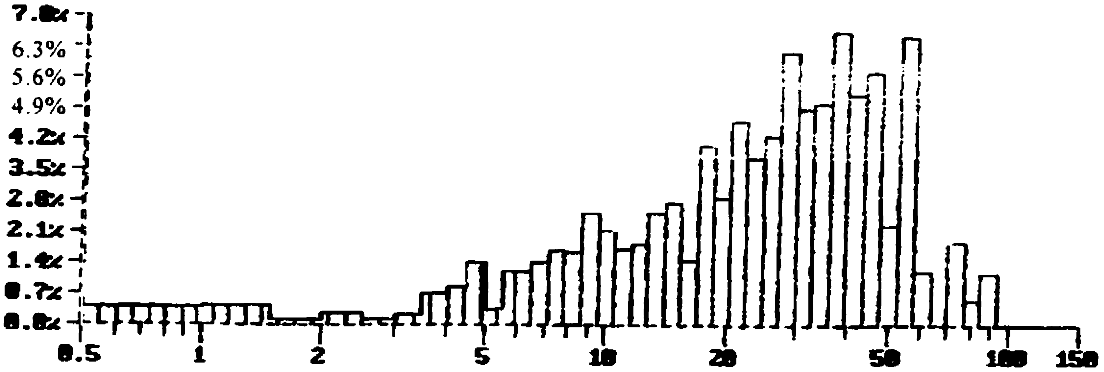

Figure 4.24 b: Density chart of the precipitates formed at a temperature of 40°C (initial A/C ratio of 1.38 and precipitation time of 24 hours).

## *4.4 Effect of the initial soluble A/C ratio*

During an experiment, the growth and the nucleation rate depend on the initial A/C ratio. Different initial A/C ratios will give different size distributions. Thus the effect of the initial A/C ratio was studied between the range 0.89 and 1.79. The corresponding amount of aluminum and sodium hydroxide dissolved in the mother solution is represented in Table 4.1. The concentrations reported here are from the atomic absorption analysis of the mother solution. The aluminum concentration was kept constant: just the sodium hydroxide concentration was varying in all the experiments.

**Table 4.1:** Initial amount of aluminum and NaOH dissolved in 1 L of mother solution.

| Initial A/C ratio | Aluminum (g) | Sodium Hydroxide (g) |
|---|---|---|
| 1.79 | 29 | 39.6 |
| Reference : 1.38 | 29.43 | 51.81 |
| 1.19 | 29.02 | 59.48 |
| 0.89 | 29.43 | 80.90 |

Figure 4.25 shows that the solubility of aluminum increases with the increase in the sodium hydroxide concentration as reflected by the increasing equilibrium A/C ratio. The influence of the sodium hydroxide concentration was less important than the effect of the temperature. While the equilibrium A/C ratio increased by around 180% for a difference of temperature of 50°C, the equilibrium A/C ratio just increased of 30% for a sodium hydroxide concentration varying from 0 to 100 g/L.

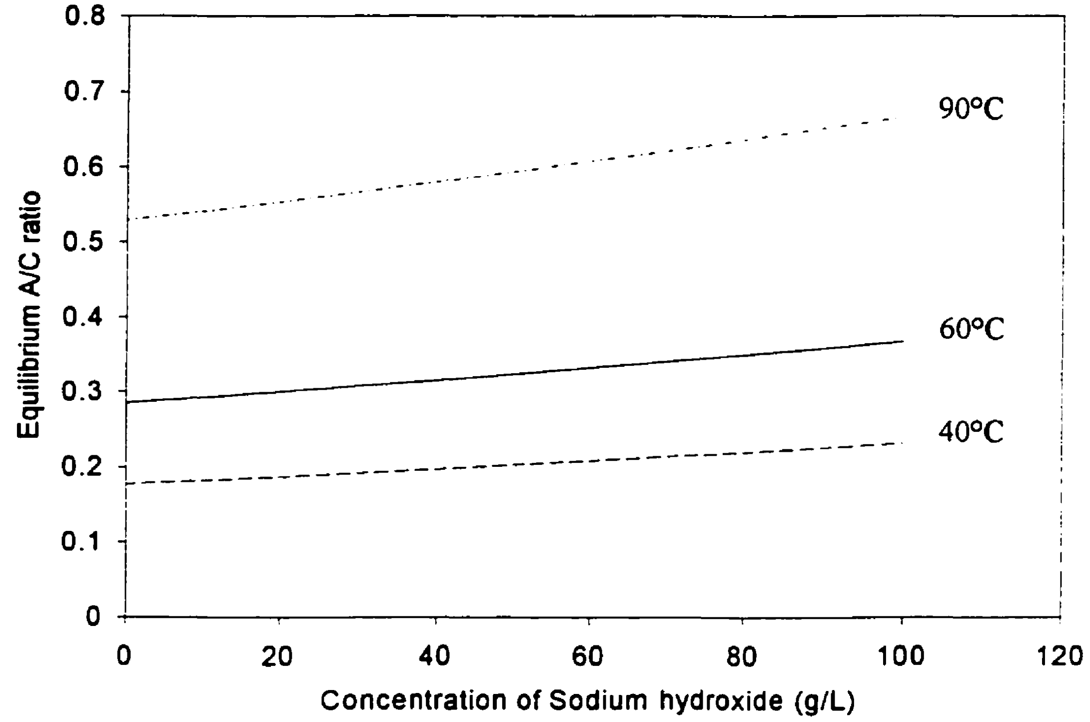

**Figure 4.25:** Effect of sodium hydroxide concentration on the equilibrium A/C ratio for different temperatures.

Figure 4.26 represents the decrease of the dissolved aluminum (expressed by the A/C ratio) in the reactor during the crystallization process. In this Figure, a fast decrease in the ratio was observed at the beginning of the reaction. As time elapsed, the ratios stabilized at some value. The two extreme initial values of 1.79 and 0.89 showed expected results. At initial A/C ratio of 1.79, the crystallization occurred immediately due to the high driving force. Because of the lack of appropriate equipment, the small particle size in the initial first hour of the experiment was not measured. However Söhnel and Garside (1992) reported that high supersaturation favors fast nucleation rate during this stage. They also report that at this high supersaturation level, the rapid formation of nuclei decrease the average nucleus size but increase the surface where the growth units attach. Thus, the removal of aluminum from the solution is faster. As seen in the Figure, the ratio decreased by 50% after 2.5 hours, 70% after 10 hours and then decreased by 12% until the end of the experiment, 24 hours later.

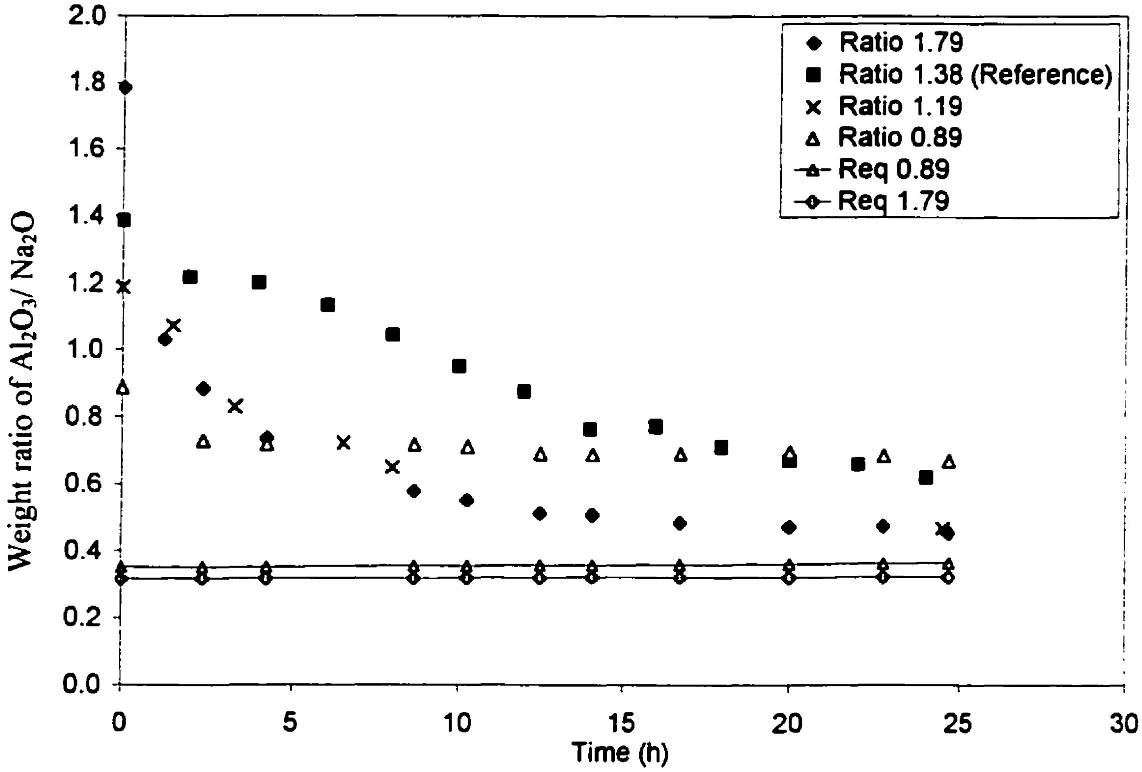

**Figure 4.26:** Evolution of the crystallization for different initial ratios of A/C (temperature of 60°C).

In contrast, in the case of the minimum experimental initial A/C ratio of 0.89, the ratio decreased by 18% during the first 2.5 hours and then decreased slowly by 12% in 24 hours. The supersaturation and thus the driving force were not sufficient enough to allow the formation of a large number of nuclei. The main result of this was that the surface area available for growth was not sufficiently large. Thus, while after 4 hours the ratio is the same for the two graphs of the initial A/C ratios 1.79 and 0.89, the initial ratio of 1.79 decreased to a value of 0.47 compared to 0.67 for the latter due to the higher contact surface available. As observed in Figure 4.26, there was also a small difference in the equilibrium ratio between the initial A/C ratio 0.89 and 1.79. Figure 4.27 shows the supersaturation for all four cases, which followed the same trend as that of the A/C ratio. All the different initial ratios lead toward the approximately same supersaturation value of 1.79 at the end of the 24 hours experiments. This value is about 40% higher than the equilibrium. For the initial A/C ratio of 0.89, as the growth rate was very slow and the contact surface area was low, the final supersaturation was 80% higher than the equilibrium. Similarly at an initial ratio of 0.89 and a temperature of 45°C, no crystallization was expected and none observed because as shown in Figure 4.18, the rate of crystallization at 45°C is very small. In order to observe any important change in the crystallization rate at this low temperature, the supersaturation has to be around 6 (Figure 4.18).

In Figure 4.27, the supersaturation for the initial ratio A/C ratios of 1.19 and 1.38, illustrated an unstable crystallization. The growth rate for the reference case (initial A/C ratio of 1.38) was slower than the growth rate of the initial A/C ratio of 1.19. This resulted in a rapid reduction of the supersaturation for the latter and thus in the formation of more crystals. This was confirmed by the results shown in Figure 4.28, where the slurry density for the A/C ratio of 1.19 was higher by 34% than for the initial A/C ratio

1.38. A replicate of the initial A/C ratio 1.19, prepared with the same mother solution and ran in parallel with the same initial conditions, reached at the end of the experiment, 24 hours later, a slurry density of 40 g/L. This value was 27% lower than the other initial A/C ratio of 1.19. The instability in the rate of crystallization was also observed with replicates of the initial A/C ratio 1.38. This instability was mainly due to the small amount of seed added. Since there was not sufficient seed present in the mixture for a secondary nucleation (Figure 1.4), the lag time may vary due to uncontrolled primary nucleation.

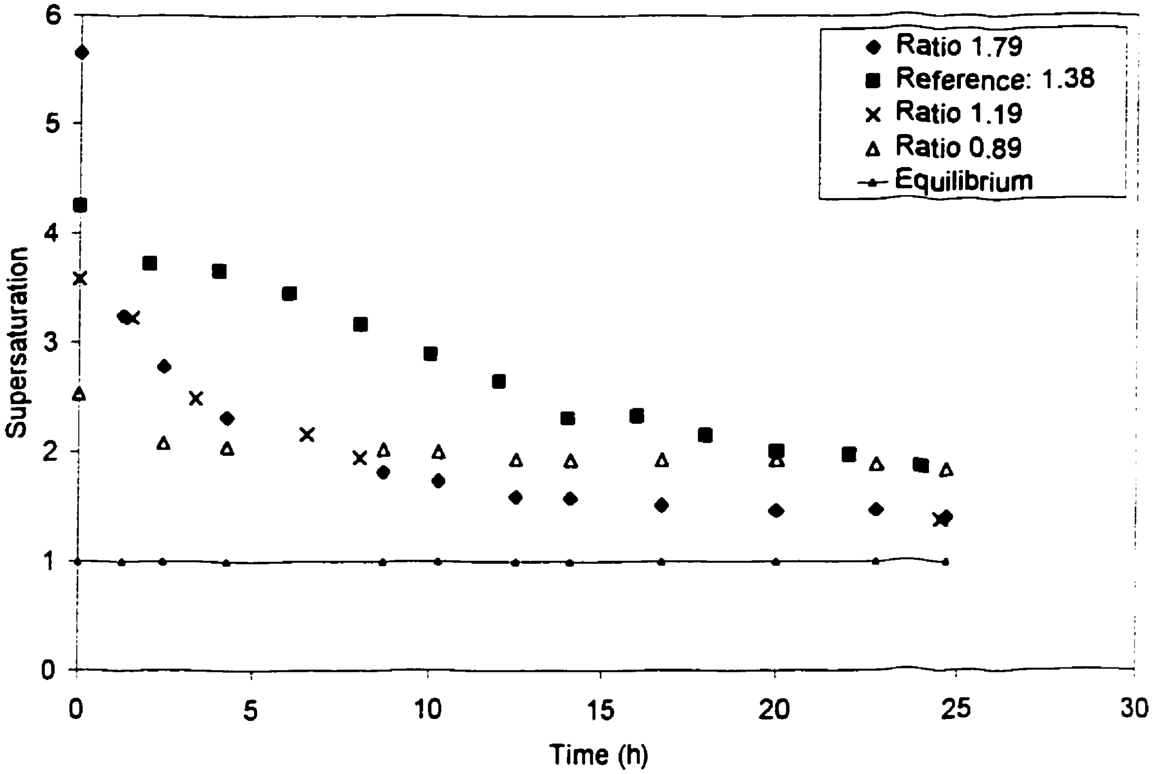

**Figure 4.27:** Effect of the initial A/C ratios on the supersaturation (temperature of 60°C).

Furthermore, as noticed above, the crystallization process of the initial A/C ratio 1.79 was fast. While the slurry density of the 1.19 ratio produced around 54 g/L in 24 hours, the 1.79 ratio produced 42 g/L of precipitate in only 4 hours and around 52 g/L in

10 hours. The main crystallization step in the initial A/C ratio 1.19 was during the first 8 hours with a decrease of the A/C ratio of 46% and a production of 27 g/L of $Al(OH)_3$. At the end of the experiment, the slurry density reached a maximum limit concentration of 60 g/L corresponding to the minimal value of the supersaturation (around 1.3).

Figure 4.29 a and b show the crystal size distribution for two different ratios at the end of the experiment after 24 hours. As observed, the average size of the particles was bigger for a higher A/C ratio and smaller in the case of a smaller A/C ratio. For the initial A/C ratio of 0.98 and 1.38, the average diameter was 37 μm and 66 μm respectively.

At the end of the experiments, the mass balance for the initial A/C ratio 1.79, the reference 1.38, the initial A/C ratio 1.19 and the initial A/C ratio 0.89 showed an uncertainty of less than 7%.

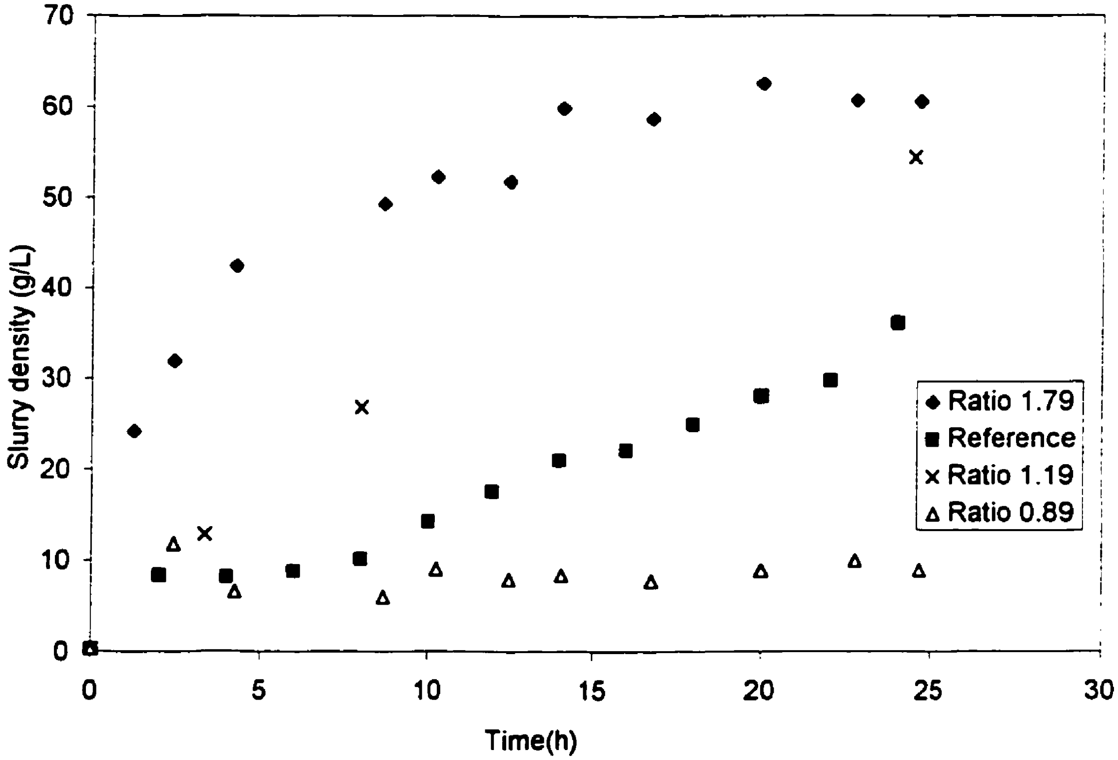

**Figure 4.28:** Effect of the ratio on the slurry density of $Al(OH)_3$ at a temperature of 60°C.

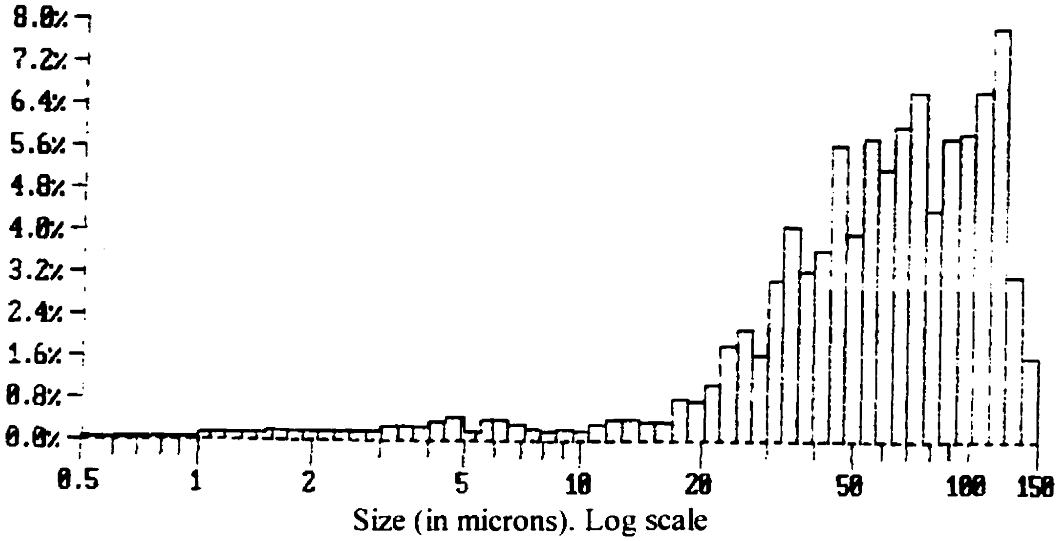

**Figure 4.29 a:** Density chart of the precipitates formed at 60°C with an initial A/C ratio of 1.38 (precipitation time of 24 hours).

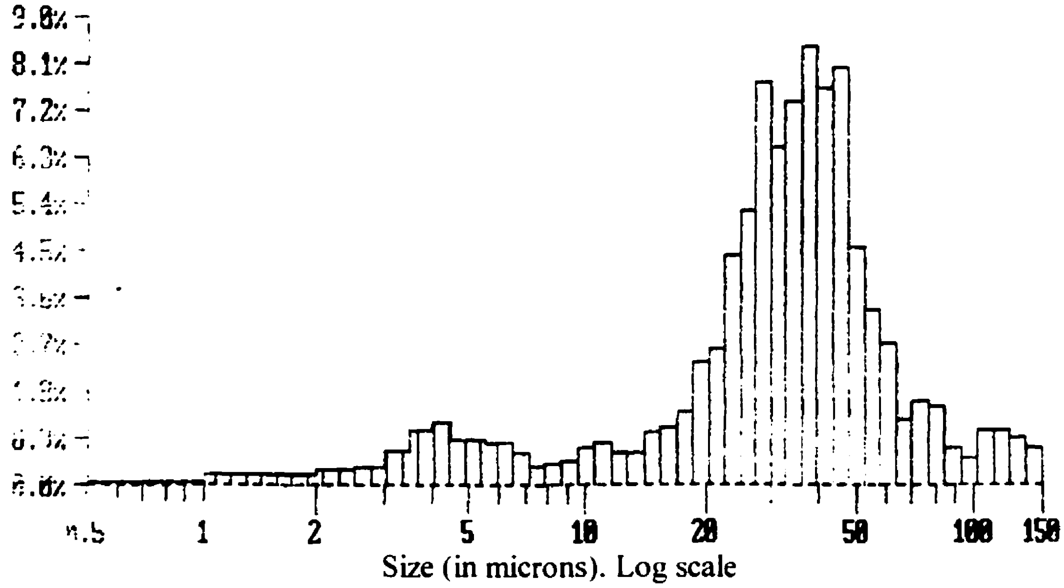

**Figure 4.29 b:** Density chart of the precipitates formed at 60°C with an initial A/C ratio of 0.98 (precipitation time of 24 hours).

## 4.5 *Effect of impurities*

The purpose of this section was to present the effect of the soluble and insoluble impurities on the morphology of the alumina crystals. To meet this objective, first the morphology of the added and precipitated impurities is presented. Subsequently, the results of the added impurities of $TiO_2$ and $Fe_2O_3$ are discussed. Finally, the results are explained in terms of the zeta-potential and settling velocity.

### 4.5.1 Definition of the different impurities in the precipitate

The soluble and insoluble impurities present in bauxite find their way into the mother solution where they have an effect on the crystal morphology (Section 1.4, Table 1.1). To study their effect, experiments with the addition of $TiO_2$ and $Fe_2O_3$ (the most common impurities in bauxite) were conducted up to a maximum concentration of 3 g/L. In addition to these added insoluble impurities, there was a minor source of impurities in the reactor from the sodium hydroxide solution and the aluminum powder used to prepare the mother solution.

The impurities present in the mixture of aluminum metal and NaOH were, from the highest to the lowest concentration, calcium, ferric and silicate ions. While silicate originated only from the sodium hydroxide, calcium and ferric ions were detected in both the sodium hydroxide and the aluminum powder. Compared to the two other impurities, the amount of silicate ions was very low (less than 1 ppm in the pure sodium hydroxide) and can be neglected. Also during the crystallization process without any added impurities, the ferric ions in the solution were negligible and no precipitates were observed while the calcium precipitate was observed on the SEM image (Figure 4.30). The crystal was identified as a calcium compound by x-ray analysis (EDAX).

**Figure 4.30:** Calcium salts formed in the reactor.

The formation of sodium salt (most likely NaOH) on the crystal surface was also observed. Figure 4.31 shows an example of the fractal shape of the soluble sodium salt crystallized on the aluminum surface during the drying of the samples. In this case, the sample was not sufficiently washed and the presence of the soluble sodium salt was confirmed by x-ray energy dispersive analysis. When the amount of sodium detected was not important, traces of sodium salts were also observed between the crystals of aluminum trihydroxide.

In the experiment with the intentionally added $TiO_2$ and $Fe_2O_3$, these impurities were detected on the surface of the crystals. The particles of $TiO_2$ and $Fe_2O_3$ added as impurities had a diameter less than 1μm; however some of them formed agglomerates as shown in Figures 4.32 a and b. These two impurities ($TiO_2$ and $Fe_2O_3$) were insoluble in the solution. No trace of soluble titanium or iron was ever detected in the solution.

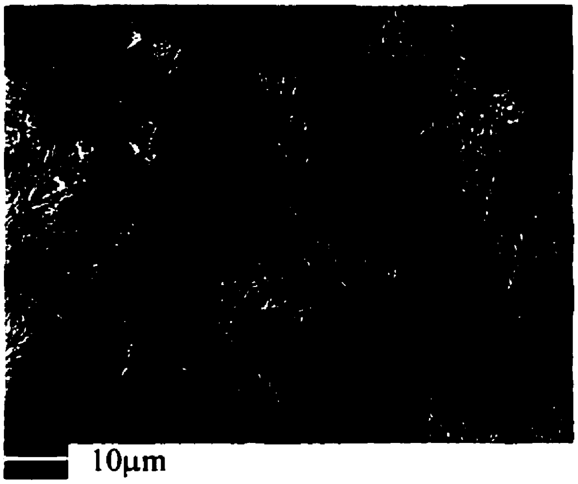

**Figure 4.31:** Sodium salt formed on the $Al(OH)_3$ crystals during the drying process.

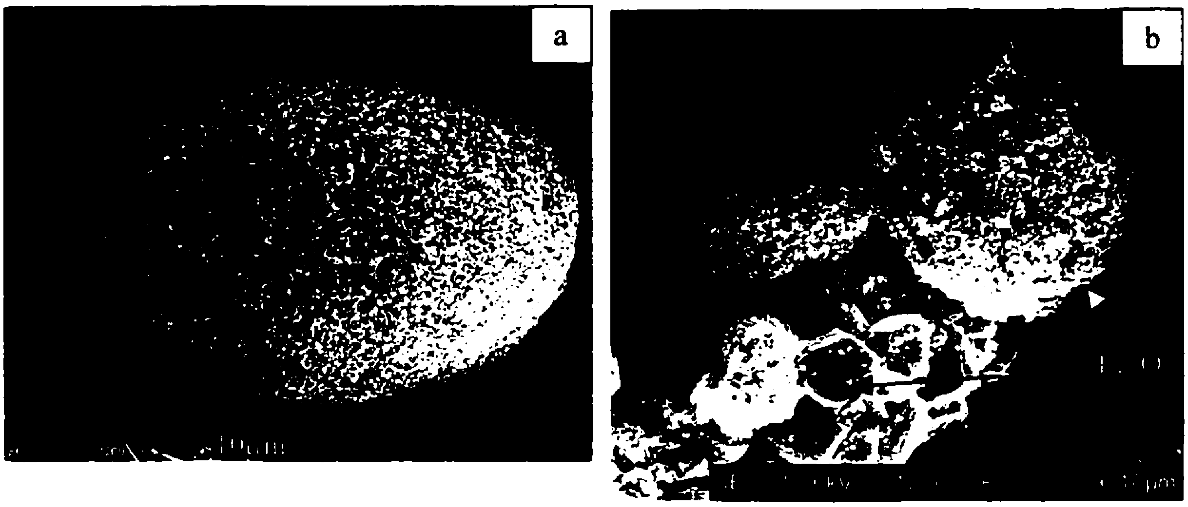

**Figure 4.32:** (a) Pellet of titanium oxide; (b) Iron oxide in pellet and stuck on the crystal surface (confirmed by x-ray energy dispersive analysis).

### 4.5.2 Effect of titanium oxide

The effect of titanium oxide on the precipitation process is presented in this section. Between 0.2 to 3 g/L of solid titanium oxide impurity were added to the solution at the beginning of each experiment. This amount of impurity corresponds to a weight percent of 0.005 and 0.055 per gram of $Al_2O_3$ calculated for a case of 1.31 initial A/C ratio. The weight percentages used here are lower than the percentage of $TiO_2$ found in the bauxite and in the industrial $Al(OH)_3$ as reported in section 1.4 Table 1.1.

Figure 4.33 illustrates the decrease of the A/C ratio when 0.2, 0.75 and 3 g/L of the $Ti_2O$ impurity is added. To be consistent in the analysis of the effect of small impurity amount and to avoid some initial variations of the A/C ratio, the same mother solution was used for the experiment conducted under 0.2 and 0.75 g/L. The experiment conducted under 3 g/L of $TiO_2$ was realized with a new freshly prepared mother solution. As observed in Figure 4.33, the addition of 0.2 g/L of $TiO_2$ did not have a great effect. The curve was close to the reference curve used. A maximum difference of 8% was observed between the two curves. However by adding 0.75 g/L of $TiO_2$, the soluble A/C ratio was significantly decreased in 10 hours. The decrease was about 45% in the case of the 0.75 g/L compared to only 30% for the reference and the 0.2 g/L of $TiO_2$. After 10 hours, the rate of precipitation with 0.75 g/L of $TiO_2$ decreased as seen by the reduction in the slope. In the case of the reference and 0.2 g/L of $TiO_2$, this reduction was noticed 4 hours later. The difference in the dissolved aluminum between the two impurity levels was around 20% from 10 hours until the end at the experiment. It was also noticed that the addition of 3 g/L of $TiO_2$ impurity affected the weight ratio in the same order than 0.75 g/L of $TiO_2$ impurity. In summary, the effect of $TiO_2$ is significant when added at or above a concentration of 0.75 g/L.

Figure 4.34 shows the change of the slurry density during the crystallization. The particle concentrations of the different amounts of $TiO_2$ were close during the first 6 hours of the crystallization. After this time, the slurry density of the 0.2 g/L of $TiO_2$ was lower than the slurry density of the higher amount of impurity (0.75 and 3 g/L of $TiO_2$). Also, the slurry density of the 0.2 g/L of $TiO_2$ was higher than the reference.

At the end of the experiment, with the convergence of the two weight ratios, the final slurry density for all cases was around 36-40 g/L. Thus the addition of $TiO_2$ increases the crystallization rate as noticed previously. The particle concentrations of the 0.75 and 3 g/L of $TiO_2$ have produced 15 to 30% more precipitate than the experiment with 0.2 g/L of $TiO_2$. The mass balance was closed with an error of 15% on the final values.

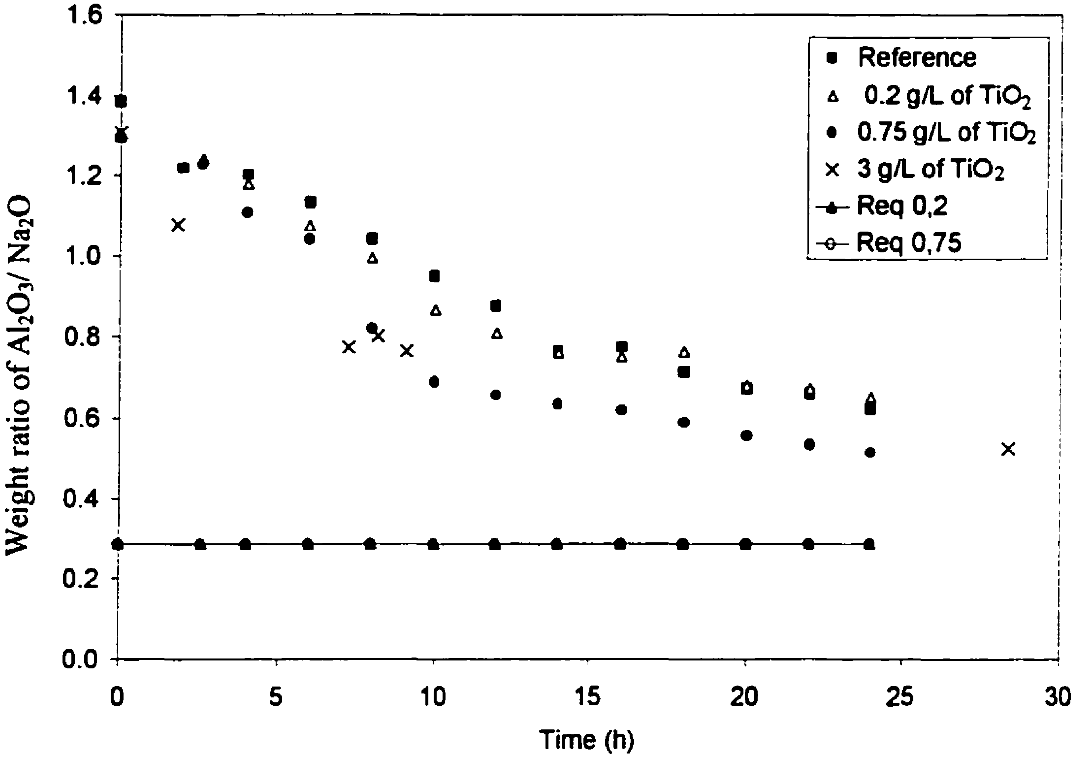

**Figure 4.33:** Influence of the titanium oxide impurity on the precipitation process (temperature of 60°C).

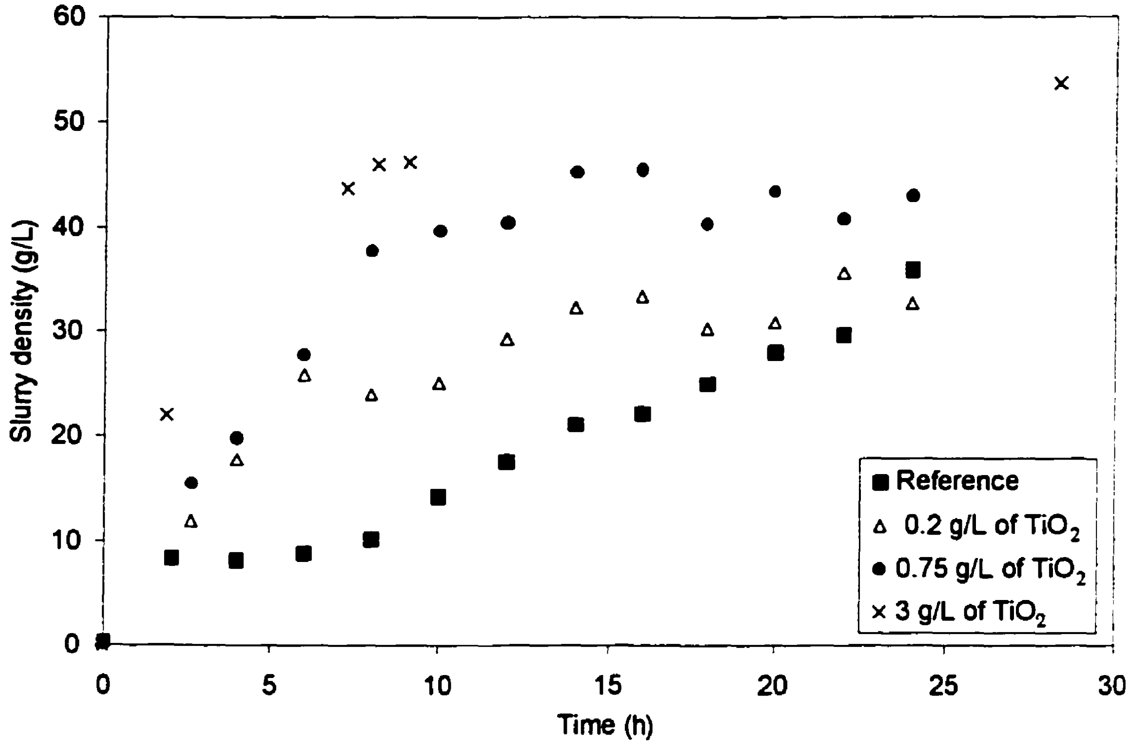

**Figure 4.34:** Increase of the precipitation of $Al(OH)_3$ with the addition of $TiO_2$ impurity (temperature of 60°C).

The image analysis of the precipitates by SEM is shown in Figure 4.35. As observed in Figure 4.35 a and d, the crystals formed with 0.2 g/L and 0.75 g/L of $TiO_2$ were very different. While the size of the crystals formed under the former case was close to those obtained without impurity, the crystals formed under the latter case were smaller. Figures 4.35 b, c, e and f illustrate the main difference between these two conditions of precipitation. The crystals formed with 0.2 g/L of $TiO_2$ corresponded mainly to agglomerated particles. The Martin's diameter estimated in Figures 4.35 b, c gave particles with diameters of 80 μm to 100 μm. The smallest diameter observed was 40 μm. Furthermore, the particles shown in Figure 4.35 c were agglomerates of smaller single crystals having a hexagonal and prismatic structure and a diameter of about 14 μm. The

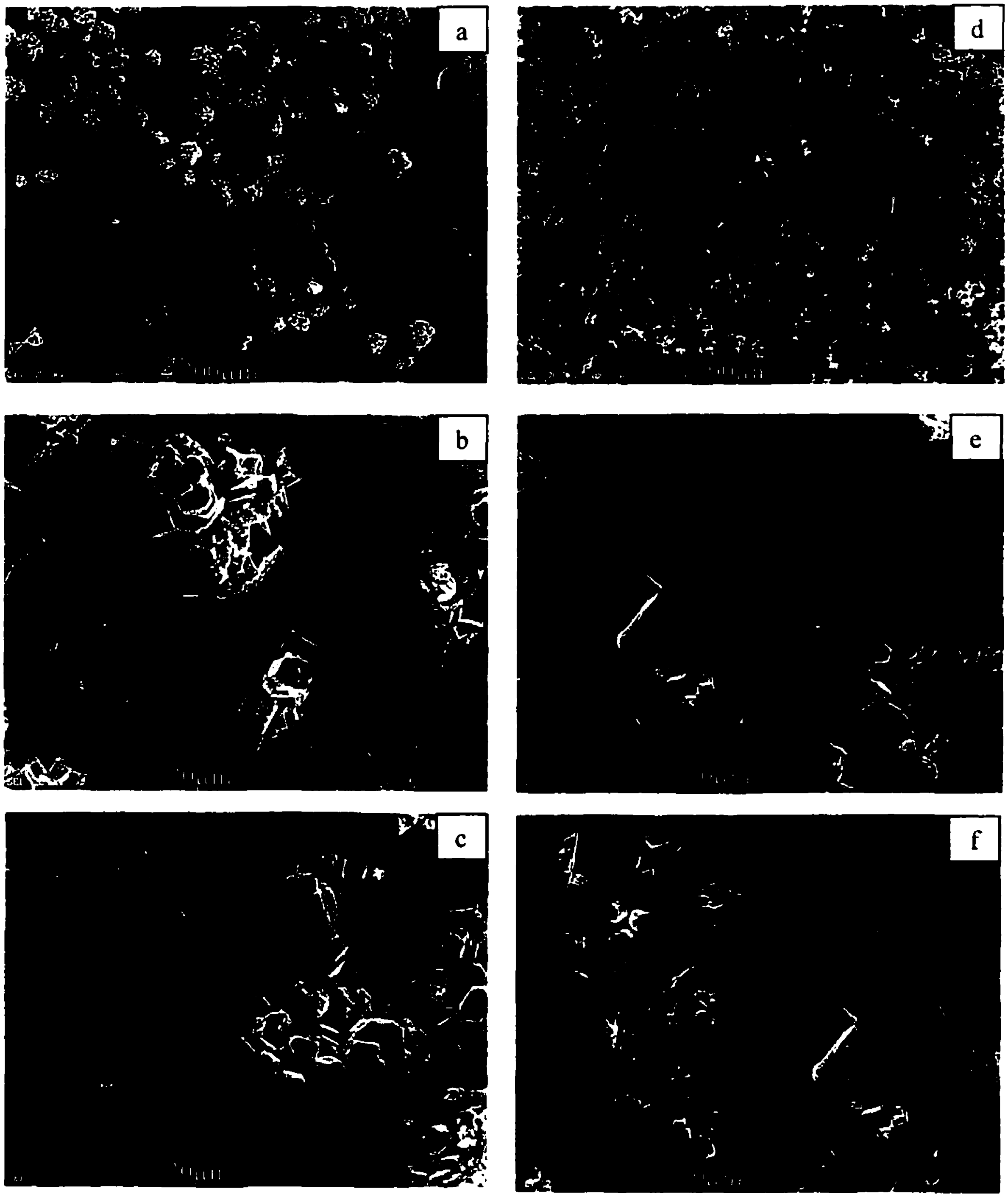

**Figure 4.35:** Influence of the Titanium oxide on the precipitation process (temperature of 60°C, initial A/C ratio of 1.31, precipitation time of 24 hours):

(a), (b) and (c) with 0.2 g/L of $TiO_2$; (d), (e) and (f) with 0.75 g/L of $TiO_2$.

longer ones could have a length of 46 μm and a width of 20 μm. In contrast, Figures 4.35 e, f show single long hexagonal crystals with 0.75 g/L of $TiO_2$ added. In this case, there were not many large agglomerates formed of various crystals as in the previous Figures. Their dimension varied from around 17 μm to 35 μm for the length and 8 μm to 17 μm for the width. In the case of the agglomerate observed in Figure 4.35 e, the crystals formed on its surface have an average diameter less than 8 μm, which was smaller than the ones observed in Figures 4.35 b and c.

The previous observation on the decrease of the size of the particle with an increase of the amount of $TiO_2$ was confirmed by the particle size analysis of the final precipitate. The size distributions of the $Al(OH)_3$ produced after 24 hours, with and without added impurity, were shown below in Figures 4.36 a, b, c. As observed on these charts, the size distribution decreased with and without impurity. It was found that the average size of the crystals was:

- 65 μm for the reference.
- 35 μm for the solution with 0.75 g/L of titanium oxide.
- 42 μm for the solution with 3 g/L of titanium oxide.

Although the average size of the higher concentration of titanium oxide (3 g/L) appeared to be larger than the average size of 0.75 g/L, the addition of the titanium oxide decreased the average size by at least 35%.

$TiO_2$ is believed to favor the nucleation by increasing the contact surface with the solution and then by acting like a seed. This was confirmed by the increase of the amount of $Al(OH)_3$ formed with an increase of the total amount of $TiO_2$ added (Figure 4.34).

**Figure 4.36 a:** Density chart of the precipitate formed with no impurities (temperature of 60°C. initial A/C ratio of 1.38 and precipitation time of 24h).

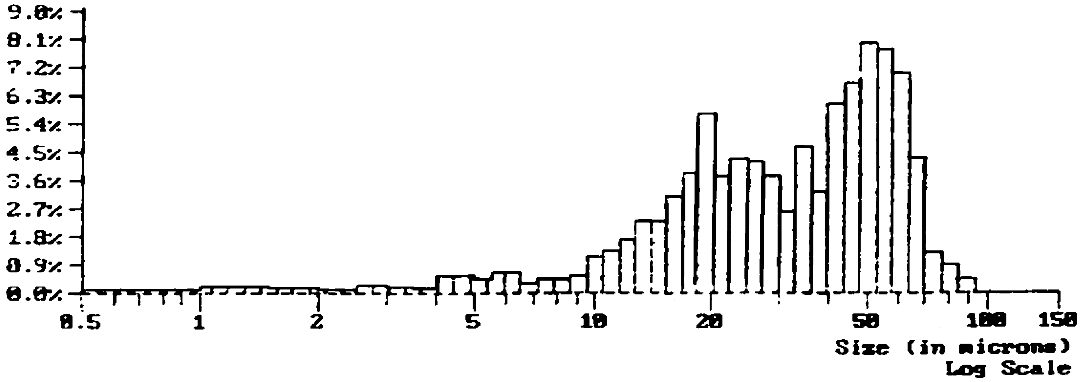

**Figure 4.36 b:** Density chart of the precipitate formed with 0.75 g/L of titanium oxide (temperature of 60°C. initial A/C ratio of 1.31 and precipitation time of 24h).

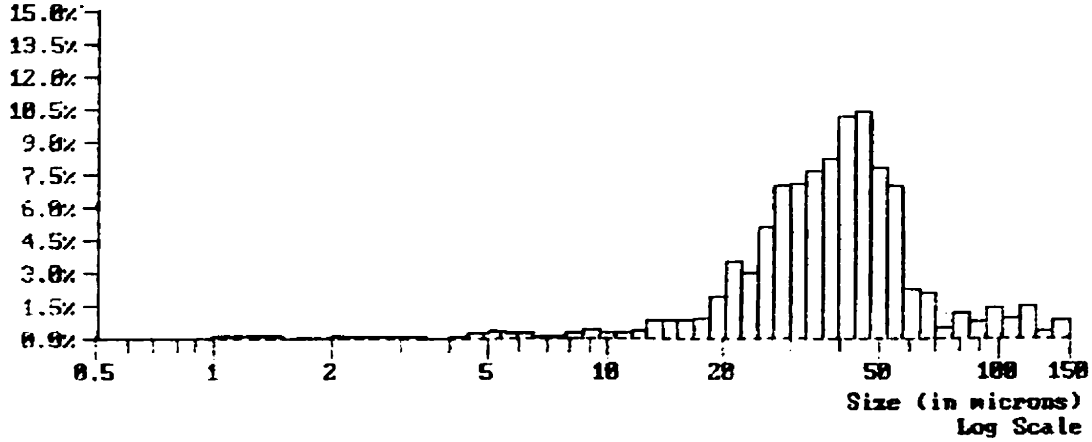

**Figure 4.36 c:** Density chart of the precipitate formed with 3 g/L of titanium oxide (temperature of 60°C. initial A/C ratio of 1.31 and precipitation time of 24h).

The crystallization process was thus faster, but the particles obtained after 24 hours were smaller. However, the uncertainty in the sample preparation method used could not determine the real relation between the size of the particles and the amount of impurity. Furthermore, as the titanium oxide did not dissolve in the caustic solution (confirmed by ICP analysis of the final solution), it was observed to be attached on the crystals (detected by x-ray energy dispersive analysis). This could explain the formation of smaller $Al(OH)_3$ agglomerates due to the competition between the $Al(OH)_3$ (growth unit and agglomeration) and the impurity to attached on the crystal surfaces to the kink sites.

### 4.5.3 Effect of ferric oxide

The effect of ferric oxide impurity on the crystallization process is described in this section. Between 0.2 to 1 g/L of $Fe_2O_3$ were added to the solution at the beginning of each experiment. This amount corresponds to a weight percent of 0.4 and 2 per gram of $Al_2O_3$ calculated for the respective case of the initial A/C ratio 1.15 and 1.38. The weight percentages used here corresponded to the average amount of $Fe_2O_3$ present in the $Al(OH)_3$ reported in the literature but was below the percentage of $Fe_2O_3$ found in the bauxite as shown in Section 1.4 Table 1.1.

Figure 4.37 illustrates the crystallization process with four different amounts of $Fe_2O_3$. In order to avoid the influence of the initial A/C ratio, the two experiments with 0.5 g/L and 1 g/L of $Fe_2O_3$ were conducted in parallel. The same mother solution with 25.1 g/L of aluminum and 44.3 g/L of sodium hydroxide giving an initial A/C ratio of 1.38 was used for these experiments. In the case of 0.2 g/L and 0.7 g/L of $Fe_2O_3$ a new freshly prepared mother solution was used with an initial A/C ratio of 1.15 and 1.23

respectively. As observed in Figure 4.37, the ferric oxide did not have an effect on the A/C ratio representing the crystallization of the $Al(OH)_3$ dissolved in the solution. The two solutions prepared with the same mother solution had exactly the same trend. While their initial A/C ratio was higher than the two other initial A/C ratios with a maximum of 15%, the final A/C ratio at the end of the experiment was still higher with a maximum of 25%. As seen in the effect of the ratio (Section 4.4), the precipitation process could be very unstable and a slight variation in the concentration could change the characteristic of the crystallization. However the different ratio did not affect greatly the crystallization process, as in this case.

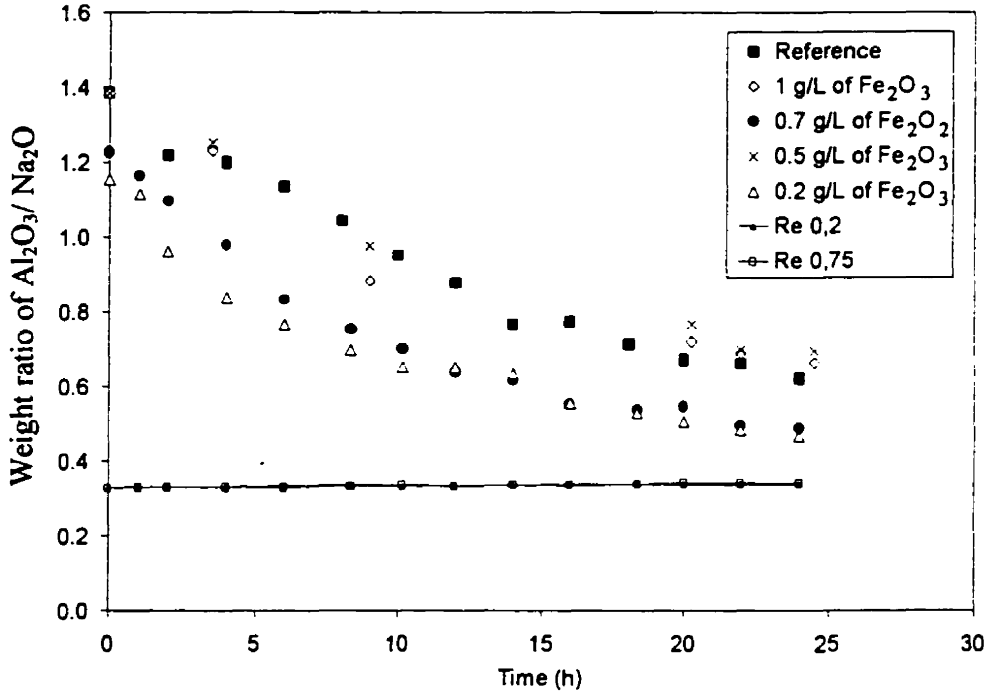

**Figure 4.37:** Influence of the $Fe_2O_3$ impurity on the precipitation process (temperature of 60°C).

In Figure 4.38, the slurry density confirmed that the ferric oxide did not affect the crystallization rate. All the different amounts of impurity reached a same maximum value

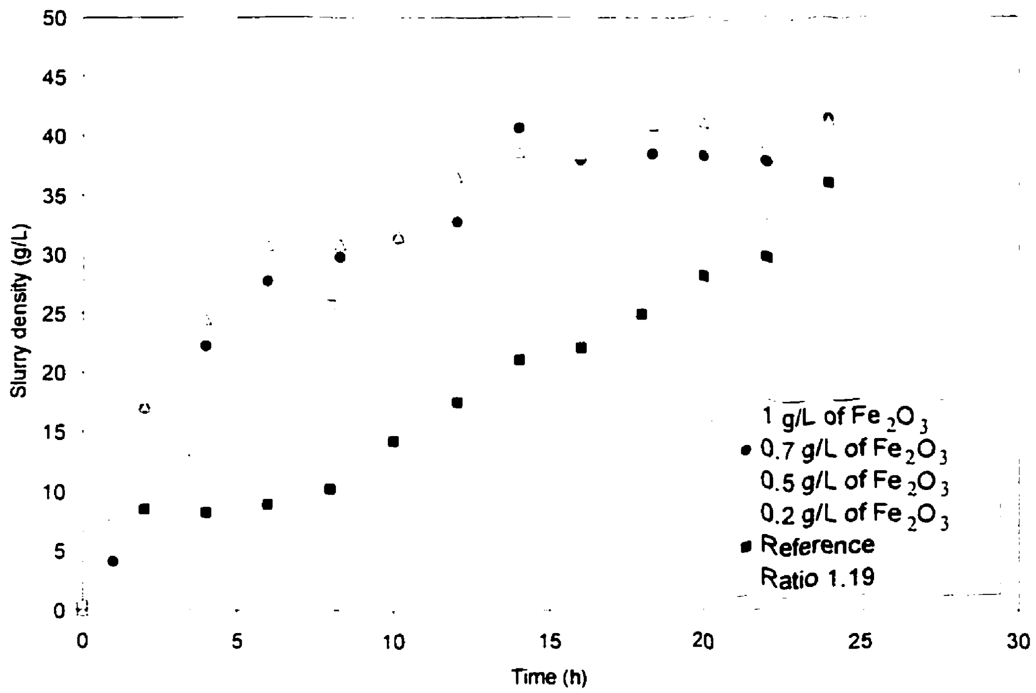

**Figure 4.38:** Stability of the particle concentration in presence of $Fe_2O_3$ impurity (temperature of 60°C, initial A/C ratios 1.38, 1.23, 1.38, 1.15 for 1, 0.7, 0.5, and 0.2 g/L of $Fe_2O_3$ respectively and 1.38 for the reference, precipitation time of 24h).

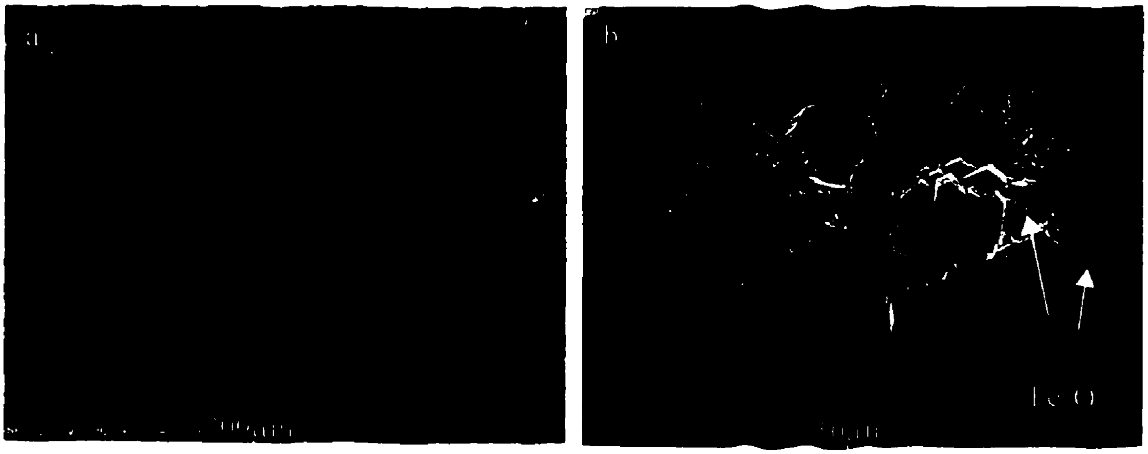

**Figure 4.39:** (a) General view of the precipitates formed under the presence of 1 g/L of ferric oxide (temperature of 60 °C, initial A/C ratio 1.38).

(b) $Al(OH)_3$ from the same sample agglomerated with ferric oxide on its surface.

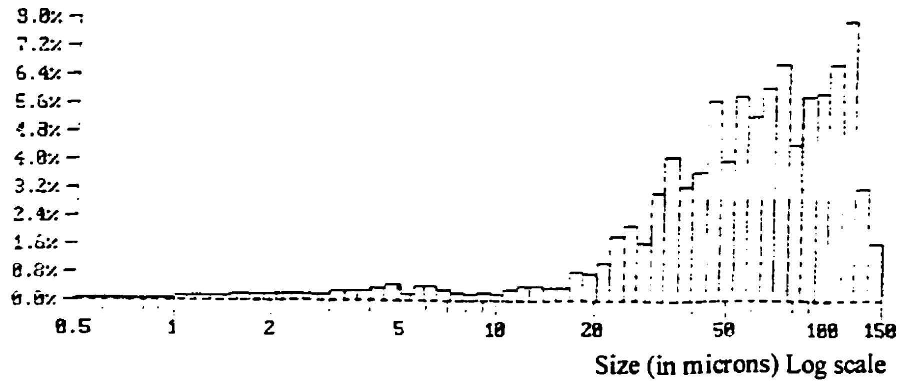

**Figure 4.40 a:** Density chart of the reference case formed with no impurities (temperature of 60°C, initial A/C ratio of 1.38 and precipitation time of 24h).

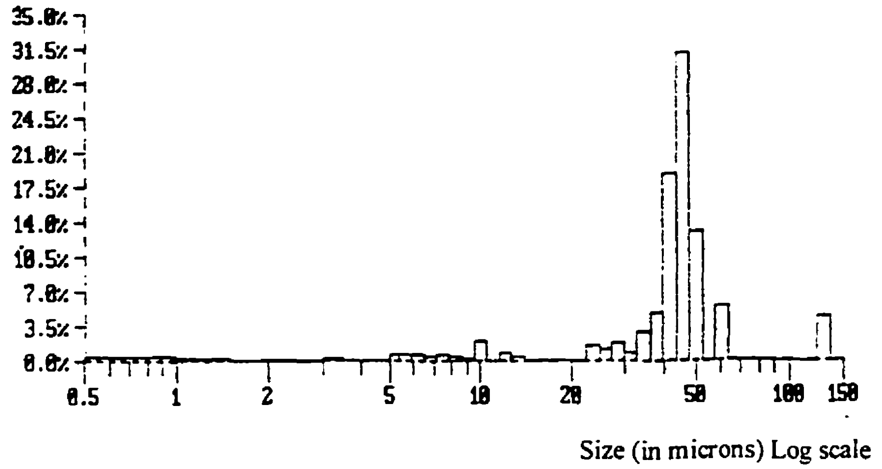

**Figure 4.40 b:** Density chart of the precipitate formed with 0.2 g/L of $Fe_2O_3$ (temperature of 60°C, initial A/C ratio of 1.15 and precipitation time of 24h).

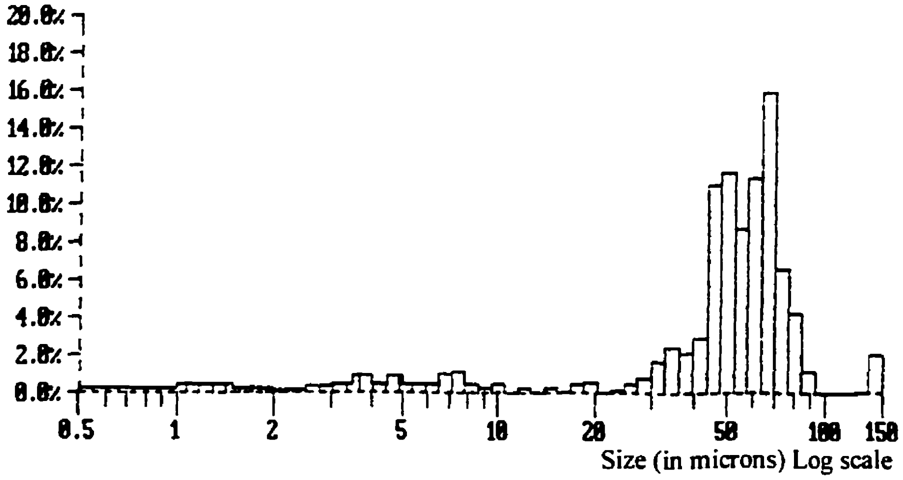

**Figure 4.40 c:** Density chart of the precipitate formed with 0.7 g/L of $Fe_2O_3$ (temperature of 60°C, initial A/C ratio of 1.23 and precipitation time of 24h).

for the particle concentration. In the case of 0.5 g/L and 1 g/L, the final slurry density was 33 g/L and 39 g/L respectively, while for 0.2 g/L and 0.7 g/L, the final slurry density was higher due to the lower weight ratio at the end of the experiment.

Figures 4.39 a and b show the typical SEM image of the precipitates formed in the presence of the ferric oxide. It was observed that small particles of ferric oxide impurity (confirmed by x-ray energy dispersive analysis) were stuck to the $Al(OH)_3$ crystals. However, while the ferric oxide did not have a significant influence on the precipitation of the crystal, the particle size analysis revealed a decrease of the size of the crystals with an increase of the amount of ferric oxide added. As observed in the Figures 4.40 a, b and c, the average size of the crystals decreased with the addition of ferric oxide and was:

- 65 μm for the reference.
- 43.5 μm for the solution with 0.2 g/L of ferric oxide.
- 50 μm for the solution with 0.7 g/L of ferric oxide.

### 4.5.4 Zeta-potential

In the previous sections (4.5.2 and 4.5.3), it was observed that the addition of $TiO_2$ or $Fe_2O_3$ as an impurity decreases the size of the $Al(OH)_3$ particles. However, while the addition of $TiO_2$ was also increasing the slurry density in the solution, the $Fe_2O_3$ had no effect. In order to elucidate the effect of $TiO_2$ and $Fe_2O_3$ on the crystals, the surface charges of the $Al(OH)_3$ under different concentrations of impurities were determined.

Figures 4.41 and 4.42 represent the variation in zeta-potential of an industrial $Al(OH)_3$ sample (obtained from Alcan) and $TiO_2$, as a function of pH, reported by Hunter (1987) and Singh *et al* (1999). The experiments in the present work confirmed this

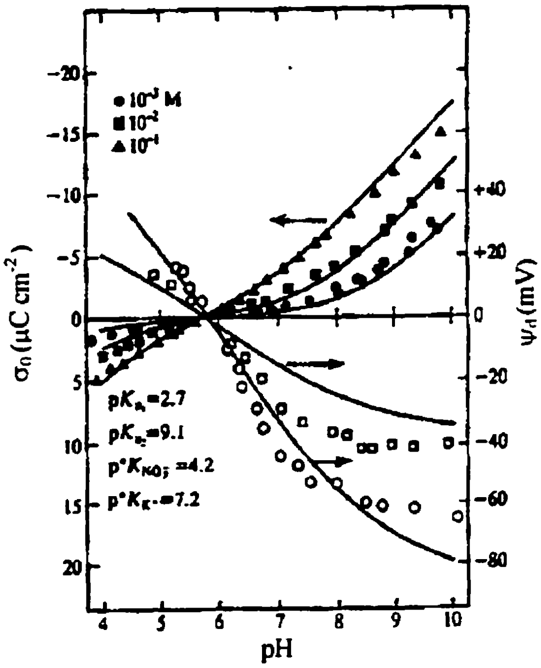

**Figure 4.41:** Surface charge density and zeta-potential of $TiO_2$ at 25°C (Hunter, 1987).

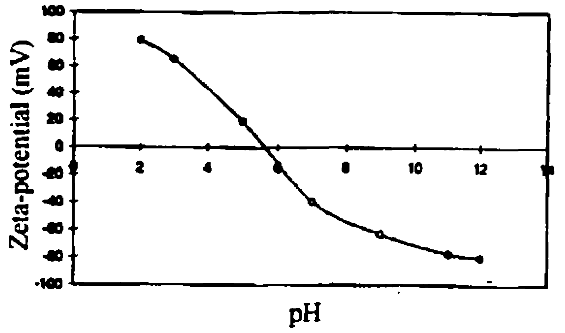

**Figure 4.42:** Zeta-potential of $Al(OH)_3$ (Singh *et al*, 1999).

**Table 4.2:** Experimental zeta potential of the aluminum trihydroxide and the impurities $TiO_2$ and $Fe_2O_3$ at 25°C.

| Compound | Zeta- Potential (mV) for pH 8.5 | Zeta- Potential (mV) for pH 12 (NaOH) |
|---|---|---|
| Aluminum trihydroxide | 43.7 | 0.5 |
| Titanium oxide | -32.5 | -38 |
| Ferric oxide | 15.1 | -42.2 |

dependence showing that the zeta-potential decreases with increasing the pH (Table 4.2). In the case of the ferric oxide and the aluminum trihydroxide, a significant decrease in the zeta-potential was observed in the experiments at the higher pH. The zeta-potential of the $Al(OH)_3$ was always higher than the zeta-potential of the two impurities. This may explain the attraction of $Al(OH)_3$ to $Fe_2O_3$ and $TiO_2$.

The main factors that govern the zeta potential appear to be the presence of the $H_3O^+$ and $OH^-$ ions. For a caustic mother solution, the potential-determining ions in the aqueous media are $OH^-$. As the pH increases, the aqueous solution becomes more conductive, reaching a limit for a pH greater than 12. The zeta-potential could not be determined for the strong caustic solution of these experiments (pH 14). By extrapolation, the zeta-potential of the three compounds seems to be negative for a pH 14. Thus, the measurements strongly suggest that both $TiO_2$ and $Fe_2O_3$ can be attracted to the surface of the precipitated particles of $Al(OH)_3$ and prevent their agglomeration (Figure 4.35).

### 4.5.5 Settling velocity

The settling velocity of a particle is related to its weight. Thus, an increase of the settling velocity of the aluminum trihydroxide will confirm the hypothesis of the attraction exercised by this latter on the ferric oxide and the titanium oxide.

Following the procedure developed by Vergouw (1998), about 2% v/v of solids were suspended in a cylinder. The pH was adjusted to 14 with sodium hydroxide to obtain the same experimental conditions (Section 3.2.6). 5, 10 and 20 grams of pure aluminum trihydroxide, ferric oxide and titanium oxide were suspended separately in the 300 mL cylinder and gave the same settling velocity. The settling velocity was thus not dependent on the amount of a same compound used. It was observed, however, that a minimum mixing time of 5 minutes before the settling measurement was necessary for the impurities to agglomerate and increase the settling velocity. If the impurities were left in the solution for a longer contact time, the size of the agglomerates stabilized and no effect on the settling velocity was observed.

Different concentrations of impurities mixed with aluminum trihydroxide were also tested as detailed in the Figure 4.43. 5 grams of aluminum trihydroxide were mixed with 1, 3 and 5 grams of $TiO_2$ or $Fe_2O_3$, corresponding respectively to 17, 37.5 and 50% of impurities. The settling velocity increased from 0.057 cm/s (pure $Al(OH)_3$) to a maximum of 0.11 cm/s for the mixture of $Al(OH)_3$-$Fe_2O_3$ and 0.16 cm/s for the mixture $Al(OH)_3$-$TiO_2$. These maxima corresponded to 37.5% of impurities. The settling velocity decreased above this amount of impurities to reach around 0.1 cm/s for the two impurities ($TiO_2$ and $Fe_2O_3$).

As observed on the graph, the curve of the mixture $Al(OH)_3$- $TiO_2$ decreased sharply for a higher amount of impurity. In contrast, the mixture $Al(OH)_3$-$Fe_2O_3$ showed a very small decrease above 37.5% of impurity. This can be explained by the effect of the pH on the settling velocity.

As observed in Figure 4.44, the settling velocity of the pure compounds and the mixtures decreased with increasing pH. The settling velocity of the $Al(OH)_3$ was lower

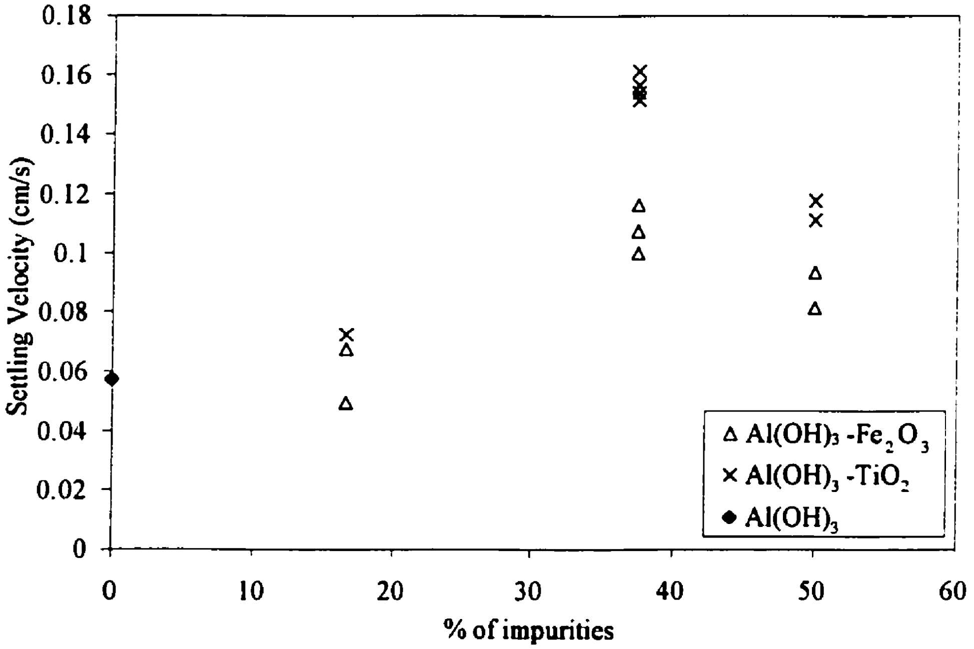

**Figure 4.43:** Effect of the amount of impurities on the settling velocity.

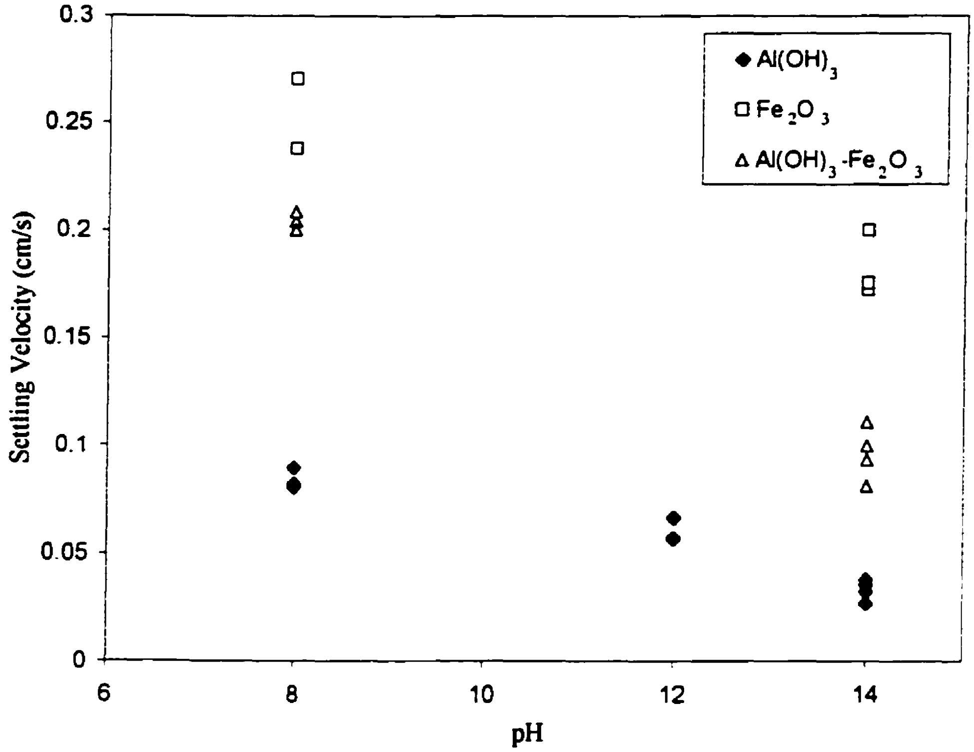

**Figure 4.44:** Effect of ferric oxide on the settling velocity of aluminum trihydroxide (5 g $Fe_2O_3$/ 5 g $Al(OH)_3$ ).

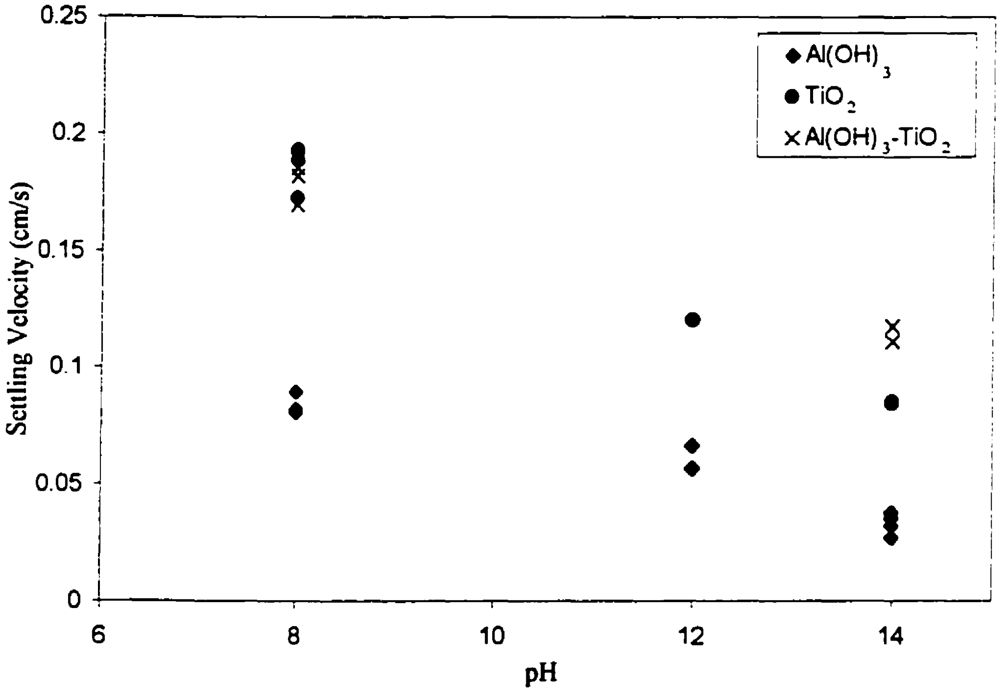

**Figure 4.45:** Effect of titanium oxide on the settling velocity of aluminum trihydroxide (5 g $TiO_2$/ 5 g $Al(OH)_3$).

than the settling velocity of the ferric oxide. When the two compounds were mixed, the settling velocity of the mixture was higher by around 50% than the settling velocity of $Al(OH)_3$ but lower by around 60% than pure ferric oxide. An explanation of this lower value can be that the particles of ferric oxide agglomerated to a greater extent than the aluminum trihydroxide. Due to a zeta-potential near zero, the aluminum trihydroxide when mixed with $Fe_2O_3$ attracted the particles of ferric oxide charged with a negative zeta-potential. Thus the settling velocity of the mixture is still higher than the settling velocity of $Al(OH)_3$ but lower than the settling velocity of the agglomerate formed by the ferric oxide. In the experiment, the amount of impurities is lower than 5% of the total amount of $Al(OH)_3$. Thus this percentage, lower than the limit of 37.5%, found previously in Figure 4.43, corresponds to a constant influence of the impurity on this compound.

In contrast, Figure 4.45 shows the decrease of the settling velocity of $TiO_2$ and $Al(OH)_3$ with an increase of the pH. The addition of $TiO_2$ increased the settling velocity of $Al(OH)_3$ by 65% at a pH 14 corresponding to the experimental conditions. When the pH increased, the settling velocity decreased constantly for the mixture and the pure compounds, due to the decrease of the zeta-potential with the pH. Thus the graph 4.43, on the effect of the amount of impurities on the settling velocity, shows that the attraction of the $Al(OH)_3$ affected by the $TiO_2$. The maximum was reached, in the case study, for a percentage of impurity of 37.5%.

## 4.6 Morphology and crystal habit of aluminum trihydroxide

In this section, some of the morphological features of the produced crystals are discussed. In the first section, the morphology of the $Al(OH)_3$ is presented in detail. In the last section, the growth mechanisms involved during the crystallization process of the $Al(OH)_3$ are discussed a related to the morphologies observed.

### 4.6.1 Particles and crystals

The aluminum trihydroxide agglomerates consist of small crystals of different shapes and sizes, oriented in all directions. In each set of experiments, the crystals appeared to have various morphologies. The regular external shape of these crystals suggests that the crystals grow slowly without impediment. The sizes are controlled by the environmental conditions within which they develop. However, under similar conditions, an observation under the SEM revealed different growth shapes on the faces of the crystals.

The typical morphology of the aluminum trihydroxide crystals observed in these experiments was various kinds of polygonal prisms (Figures 4.46 a and b). The crystal morphology can be classified into four categories: lozenges, hexagons, prisms and spheres (Figure 4.47). This latter was rare and may have been due to the attrition in the presence of impurities or very small particles. As shown in Figures 4.46 a and b, the crystal shapes slightly deviated from the perfectly shaped lozenges, hexagons and prisms structures. In these Figures (4.46 and 4.48), the x- ray diffraction analysis confirmed only the presence of pure gibbsite (synthetic and industrial as explained in section 4.1.2).

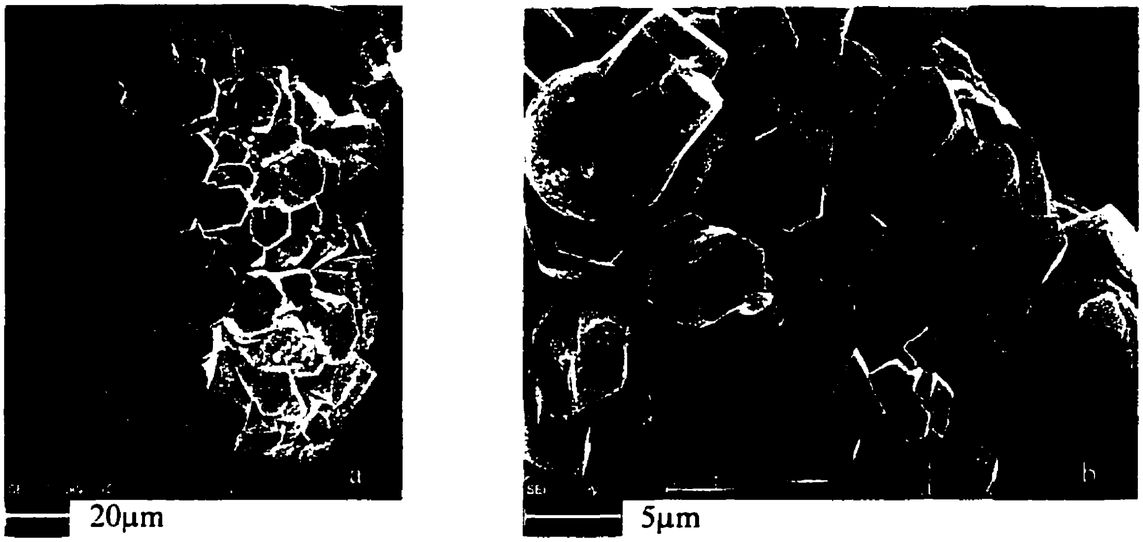

**Figure 4.46:** Examples of the aluminum trihydroxide crystal morphologies (temperature of 60°C and initial A/C ratio of 1.38).

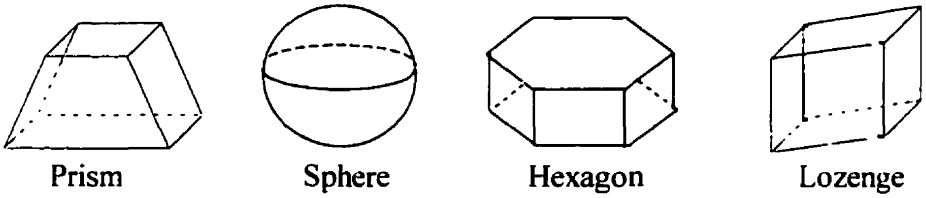

**Figure 4.47:** Schematics of different crystal morphologies.

**Figure 4.48:** Spherical and lozenge shapes formed under high attrition and low temperature (temperature of 35°C, initial A/C ratio of 1.65 and 0.5 g/L of $TiO_2$).

Results of SEM and optical microscopic observations indicated that the morphology of the crystals had a close relationship with the supersaturation level of the aluminum in the mother solution. At high supersaturation, nucleation and growth take place at the same time, the process is faster and the growth is thus more important. In contrast at a lower supersaturation, the growth process is favored compared to the nucleation process, but the process is significantly slow because of the small concentration of dissolved aluminum. Thus, at a low supersaturation, shorter hexagonal and prismatic crystals were observed compared to the ones obtained at a higher supersaturation level (Figure 4.49). Also, at the same condition of high supersaturation, it was observed that more hexagonal and prismatic (related to the hexagonal structure) shapes were obtained. The hexagons and the prisms were more stable than the other shapes because these crystals were relatively large (reaching 100 μm) and could appear in a single crystal structure (Figures 4.50 and 4.51). These single long crystals are the result of attrition and other breakage on polygonal shapes. No single crystals with a lozenge shape were observed in the experiments. In all the experiments, the size of the lozenge was always shorter than the hexagonal and the prism crystals formed. Single crystals with spherical shapes were rarely observed.

The shape of the overall $Al(OH)_3$ particles varied from very small polygonal plates to very large spheres. The particles built up by the agglomeration or growth of smaller particles tended to assume a more spherical shape as further precipitated particles were deposited on the surface. In a similar experiment, the average size of the final spherical shape was bigger than the single crystals formed during the same time. The tendency toward sphericity as the particle size increased was confirmed by SEM analysis (Figure 4.52).

**Figure 4.49:** Small single crystals formed at a low supersaturation (temperature of 60°C and initial A/C ratio of 0.8).

**Figure 4.50:** Single crystals shape (temperature of 60°C and initial A/C ratio of 1.38).

**Figure 4.51:** Single crystal formed in presence of 1 g/L of $Fe_2O_3$ (temperature of 60°C and initial A/C ratio of 1.38).

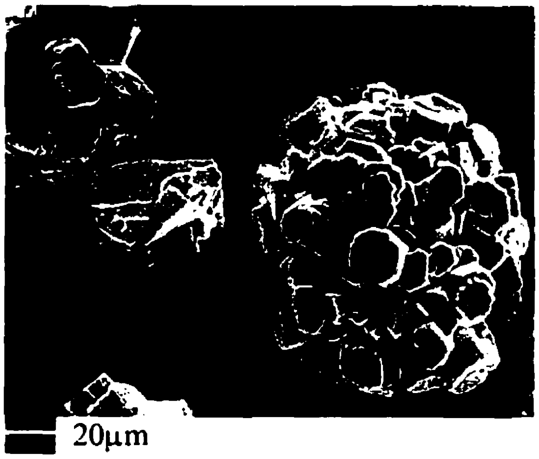

**Figure 4.52:** Spherical particles and single crystals formed at the same time (temperature of 60°C and initial A/C ratio of 1.38).

### 4.6.2 Mechanisms of growth

The growth of the aluminum trihydroxide crystals can be applied to the transfer of atoms on its surface. As explained in the section 2.3, the growth takes place at the crystal ambient phase interface. The different processes, discussed in this section, were observed during the growth of the aluminum trihydroxide crystals.

The typical morphology of the aluminum trihydroxide crystals formed in this study was various kinds of hexagonal prisms. These prisms were observed during all the process. It was noticed also that the growth of the (110) faces (as noted in Figure 2.1) was faster than the growth along the (001) faces, giving a long hexagonal prism. Different mechanisms were involved in the formation of these two faces.

Considering the overlapping principle (Figure 2.10), the growth of (110) faces can be assumed to be the result of one high translational velocity face, noted A, with 2 slow translational velocities on its side, noted B. Different theoretical evolutions of the growth are shown in Figures 4.53 and 4.54. In these Figures, following the notations in section

2.3, the high translational velocity faces and the slow translational velocity faces are denoted as A and B respectively. Thus the growth of the crystal under the overlapping principle can be decomposed into various mechanisms:

During the growth process as the faces B overlap the faces A, the hexagonal structure can be maintained only when the growth rates of the faces are the same, A or B (Figure 4.53 case 1). Otherwise, by a succession of the growth rates A and B, a polygonal shape can be obtained. In Figure 4.53 case 2, the formation of a triangular prism is shown. If the faces have different growth velocities A and B, pentagons and other prisms can also be formed. In Figure 4.54, to avoid the succession of the growth rates A and B, two identical translational velocities are located side by side. This scheme will lead to the formation of a lozenge (Figure 4.54 case 1) or a stretched hexagon (Figure 4.54 case 2). An example of $Al(OH)_3$ crystals formed during the experiment is shown in Figure 4.55.

The 2-D nucleus processes (section 2.3) were also noticed during the formation of the aluminum trihydroxide crystal on the (001) faces. In the experiments, the 2-D nucleus had various but not well defined shapes, as shown in the Figures 4.56 a and b. The 2D nucleus steps initially appeared randomly on the surface in theory. As observed on these examples (Figures 4.56 a and b), the new crystal formed was centered in the middle of the old face. The process of formation was believed to be an intermediate between a multinuclear layer-by-layer growth and a bilayer formation (Figures 2.6 and 2.7 of the layer by layer and the bilayer). However the initial step could be the result of a dislocation (as noticed later in Figure 4.60 a, the dislocation appears in the middle of the crystal surface). The 2-D process was not very commonly observed but still was more pronounced in the presence of impurities ($TiO_2$ and $Fe_2O_3$).

The SEM images of aluminum trihydroxide crystals show also the formation of multinuclear layer by layer growth and bilayer formation (section 2.3). In the case of a multinuclear layer by layer growth, the face restores the initial surface plane. The growth is a periodic process involving successive 2D-nucleation and a slow lateral growth. Thus, due to the nature of the growth, the multinuclear layer-by-layer growth (Figure 4.57) was more resistant than the bilayer growth (Figure 4.58). The formation of this latter was in

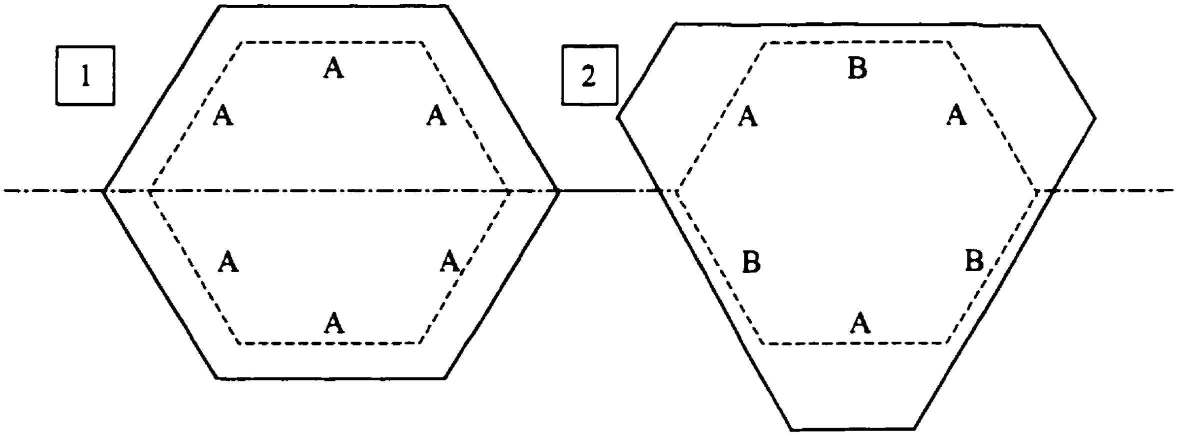

**Figure 4.53:** Growth of the aluminum trihydroxide under the overlapping principle, (1) Formation of a hexagon; (2) Formation of a prism.

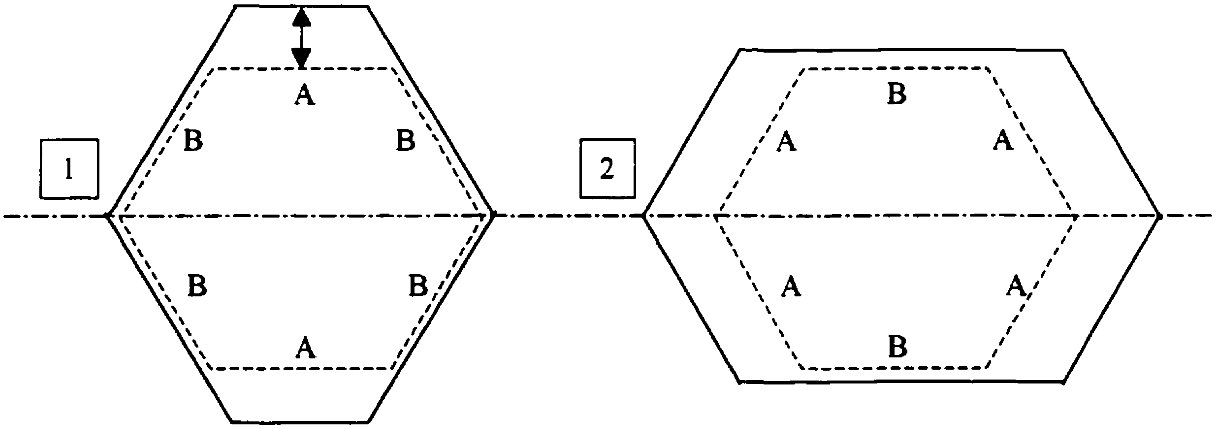

**Figure 4.54:** Growth of the aluminum trihydroxide under the overlapping principle, no A-B succession (1) Formation of a lozenge; (2) Formation of a stretch hexagonal.

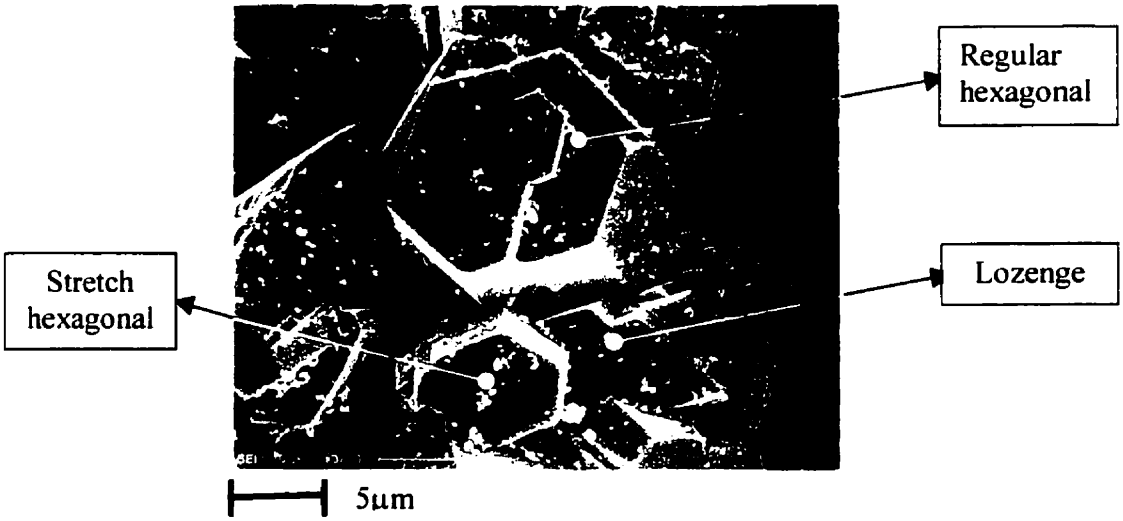

**Figure 4.55**: Shape of aluminum trihydroxide crystals produced with 0.5 g/L of iron oxide (temperature of 60°C and initial A/C ratio 1.38).

**Figure 4.56**: 2-D nucleus growth formed in a solution with respectively (a) 1 g/L and (b) 3 g/L of $TiO_2$ (temperature of 60°C and initial A/C ratio 1.38).

consequence less common. Furthermore, the thickness of the layer was a function of the supersaturation. At the beginning of the experiment, due to the high supersaturation, the layers were thicker and they decreased slowly with the supersaturation (Figure 4.57).

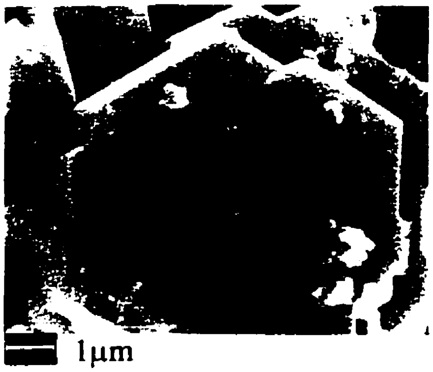

**Figure 4.57:** Experimental crystal formed by multinuclear layer-by-layer growth (temperature of 60°C and initial A/C ratio of 1.38).

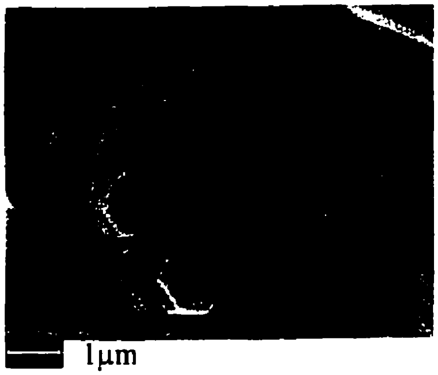

**Figure 4.58:** Experimental crystal formed by bilayer formation (temperature of 60°C and initial A/C ratio of 0.8).

Another mechanism, the spiral growth of (001) faces, was noticed during the formation of the aluminum trihydroxide crystals. As explained previously (Section 2.3), the spiral process results from a continuous growth at low supersaturation. Depending on the initial A/C ratio (which influences the speed of the "first nucleation"), the observation of this mechanism increases while the supersaturation decreases.

The typical SEM images of the spiral formation process, obtained in this study, exhibit the spirals forming only hexagonal or diamond shapes. As shown in the Figures 4.59 a and b, the spiral growth of hexagonal crystal was at higher angle than that of diamond shape crystals. Following the polygonal shape of the initial crystal, the angles were formed perfectly in the second and third steps of the spiral process. The hexagonal spiral shape was the most common compared to the diamond shape. This result from the fact that the aluminum trihydroxide has a hexagonal crystal shape. However, in presence of $Fe_2O_3$, the diamond spiral shape was formed on the hexagons following the mechanism described in Figure 4.54 case 1 (Figure 4.60). As explained above, this growth was believed to result to a diamond shape.

**Figure 4.59:** (a) Spiral growth on hexagonal and (b) diamond crystals formed at a temperature of 60°C and initial A/C ratio of 1.38.

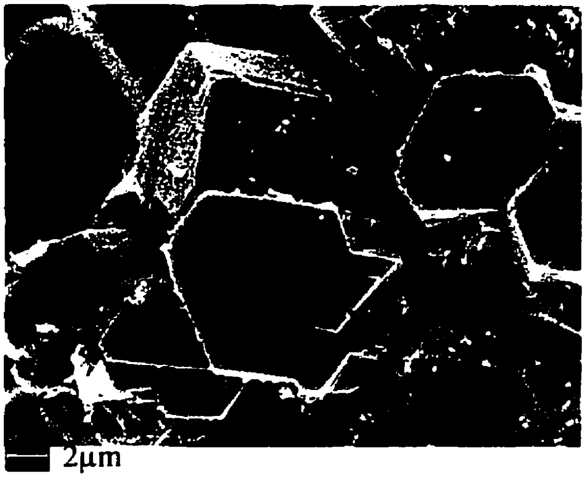

**Figure 4.60:** Diamond spiral growth formed in presence of 1 g/L of $Fe_2O_3$ at a temperature of 60°C and initial A/C ratio of 1.38.

Figures 4.61 a and b show different views of the spiral growth of aluminum trihydroxide crystals. It was observed that the development of the dislocation was more pronounced near the edge. The dislocation was then sloping with a lower thickness at the point of emergence on the (001) faces. It was also noticed that the side faces (110) of the pyramid formed were not vicinal surfaces. The spiral formation had effects on the side of the crystal. From the growth of the first dislocation on surface, dislocation appeared on the side of the hexagonal. Following the same evolution than a multinuclear layer-by-layer growth, the breakage on the side was smooth giving a constant thickness.

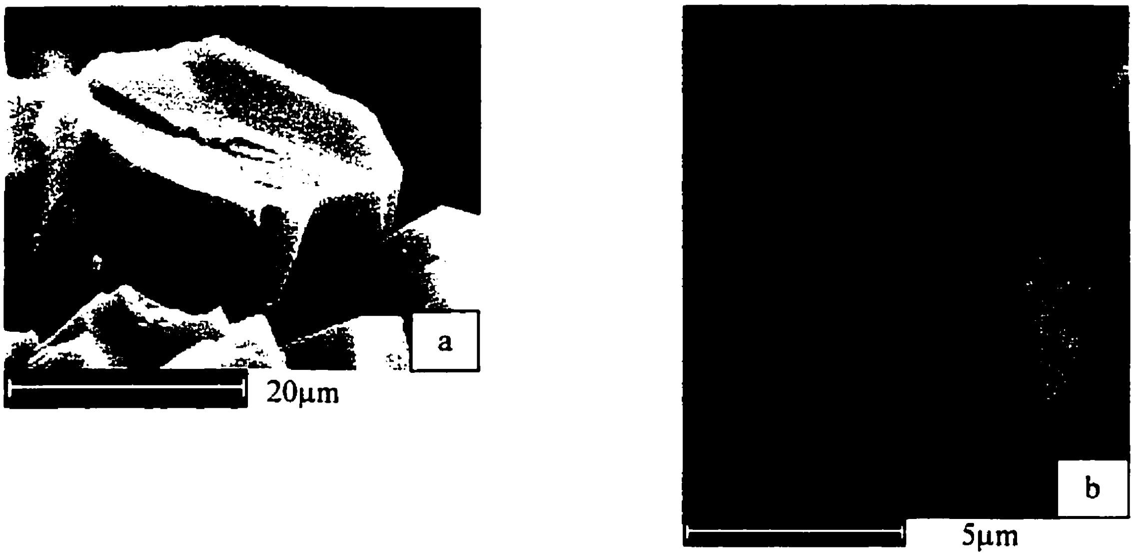

**Figures 4.61:** Different views of the spiral growth on aluminum trihydroxide crystals (temperature of 60°C and initial A/C ratio of 1.38).

# Chapter 5

# CONCLUSIONS AND RECOMMANDATIONS

## 5.1 Conclusions

The crystallization behavior of aluminum trihydroxide was studied as a function of temperature, the concentration ratio of aluminum to sodium and the presence of two particulate impurities, $TiO_2$ and $Fe_2O_3$. A batch reactor was designed to obtain homogeneous mixing and minimum attrition. The mother solution was prepared from different amount of sodium hydroxide and aluminum dissolved in the solution. All the experiments were carried out at atmospheric pressure and temperature varying between 40 to 80°C. X-ray diffraction analysis showed that the crystals of aluminum trihydroxide produced in these experiments were only gibbsite. The reference experiment performed at 60°C and an initial A/C ratio of 1.38 revealed that the mechanisms of the crystallization process consisted of an initial lag phase followed by an increase in the slurry density until the crystallization rate decreased to a level where the supersaturation was low. The initial lag phase was due to the fact that the amount of the seed used in the experiments was not sufficient enough to initiate the nucleation. Also the rate of precipitation depended strongly on the supersaturation acting as a driving force.

The effect of the reactor temperature on the crystallization of aluminum trihydroxide was also studied. The crystallization process, which was favorable at low temperature due to the high supersaturation, was kinetically limited. The increase in the temperature resulted in the production of coarser crystals and in an increase of the slurry density.

The A/C ratio had similar effect on the crystallization process as the reactor temperature. However, since the amount of seed introduced to the process was not sufficient, during the first hour of the crystallization process, either primary or secondary nucleation determined the precipitation rate. When the primary nucleation dominated, the reaction was slower than the one dominated by secondary nucleation. The equilibrium A/C ratio was not greatly influenced by the sodium concentration. The supersaturation level depended only on the initial A/C ratio. At a higher A/C ratio, the driving force was higher resulting in the faster nucleation and growth processes.

The presence of impurities had a strong effect on the size of the crystals. Titanium oxide in the mother liquor acts as a seed resulting in more abundant but small single crystals. The presence of ferric oxide did not have a strong effect on the precipitation rate, but still decreased the size of the particles and increased the slurry density.

The analysis of the surface charge measured by zeta-potential explained that the impurities, titanium and ferric oxides, adhered to the surface of aluminum trihydroxide crystals. The zeta-potential measurements made up to the pH of 12 agreed well with the literature values. At a pH greater than 12, the conductivity of the caustic solution was too high to be measured by the zeta-potential analysis. Thus, at a pH 14, the settling velocity measurements were performed to confirm the adhesion of titanium and ferric oxides on the aluminum trihydroxide crystals. This adhesion could explain the production of small single crystals. The settling velocities of crystals varied with pH and the concentration of titanium and ferric oxides.

The different evolutions of the crystal morphology were also described. A model of growth using the overlapping principle gave prismatic shapes such as diamond and hexagon as observed in the experiment. The other mechanisms of growth observed such as bilayer and layer by layer growth were illustrated and commented.

## 5.2 Recommendations

The study of the crystallization of aluminum trihydroxide can be further extended by the detailed study of the effect of other common impurities such as magnesium and calcium oxides on the settling velocity of the crystals. The design of a continuous process by operating the reactors in series is also recommended for the future work. The use of the pressured vessels may be of interest for a better control of the evaporation and to study the kinetics and the morphologies of the other aluminum hydroxides at elevated pressures and temperatures.

# Chapter 6

# REFERENCES

Addai-Mensah, J., A., Gerson, C. A., Prestidge, I., Ametov and J., Ralston, *"Interaction between Gibbsite Crystals in Supersaturated Caustic Aluminate Solutions"*, Light Metals, **1998,** 159-166.

Armstrong, L., J., Hunter, K., McCormick and H., Warren, *"Bound Soda Incorporation during Hydrate Precipitation- Effects of Caustic, Temperature and Organics"*, Light Metals, **1996**, 37-40.

Blankenship, S. L. L., *"Hydrate Quality Improvement"*, Light Metals, **1999**, 5-6.

Chan, V. A. and H. M., Ang, *"A Laboratory Continuous Crystallization System for Aluminium Hydroxide Precipitation Studies"*, Journal of Crystal Growth, **1996**, *166*, 1009-1014.

Chaubal, M. V., *"Physical chemistry considerations in aluminum hydroxide precipitation"*, Light Metals, **1990**, 85-95.

Coulson, J. M. and J. F., Richardson, Coulson & Richardson's Chemical Engineering, 5th ed., Butterworth-Heinemann, Boston, **1996**, *1*, 269-280.

Dianfeng, L., B., Shiwen, Y., Yihong and F., Gaofeng, *"A Kind of Activity Seed Used for the Precipitation of the Sodium-Aluminate Liquor"*, Light Metals, **1997**, 97-100.

Evans, K.A., "*The Manufacture of Alumina and its Use in Ceramics and Related Applications*", Key Engineering Materials, **1996**, *122-124*, 489-526.

Hiemenz, P. C. and R., Rajagopalan, Principles of Colloid and Surface Chemistry, 3rd ed., Marcel Dekker, New York, **1997**.

Hunter, R. J., Foundations of Colloid Science, Oxford University Press, New York, **1987**, *1*.

Lee, M. Y., G. M., Parkinson, P. G., Smith, F. J., Lincoln and M. M., Reyhani, "*Characterization of Aluminum Trihydroxide Crystals Precipitated from Caustic Solution*", Separation and Purification by Crystallization, G. D. Botsaris and K. Toyokura, ACS Symposium Series 667, **1997**, 123-133.

Markov, I. V., Crystal Growth for Beginners: Fundamentals of Nucleation, Crystal Growth, and Epitaxy, World Scientific, London, **1995**.

Matheson, Coleman and Bell, "*X-ray Diffraction Pattern 33-0018*", JCPDS-International Centre for Diffraction Data, **1998**.

Mei-Yin, L., A. L., Rohl, J. D., Gale, G. M., Parkinson and F. J., Lincoln, "*The Influence of Metal Ion Inclusion on the Morphology of Gibbsite*", Trans I ChemE, **1996**, *74A*, 739-743.

Misra, C., "*Solubility of Aluminium Trihydroxide in Sodium Hydroxide Solutions*", Chemistry and Industry, **1970**, 619-623.

Misra, C., Industrial Alumina Chemicals, American Chemical Society, Washington, DC, **1986**.

Patnaik, S. C. and P., Vidyasagar, "*Grain Size Distribution and Crystal Growth in Alumina Hydrate Precipitation Process*", Light Metals, **1998**, 179-185.

Perry, R. H. and D. W., Green, Perry's Chemical Engineers' Handbook, 7th ed., McGraw Hill, **1997**, section 19.

Roach, G. I. D., J. B., Cornell and B. J., Griffin, "*Gibbsite Growth History- Revelations of a New Scanning Electron Microscope Technique*", Light Metals, **1998**, 153-158.

Satapathy, B. K. and P., Vidyasagar, "*Effect of Temperature, Impurities, Retention Time and Seeding on the Rate of Crystal Growth, Nucleation and Quality of Alumina Hydrate during Precipitation*", Light Metals, **1990**, 105-113.

Scott, J., "*Effect of Seed and Temperature on the Particle Size of Bayer Hydrate*", Extractive Metallurgy of Aluminium, International Symposium, **1963**, 203-218.

Seyssiecq, I., S., Veesler, G., Pepe and R., Boistelle, "*The Influence of Additives on the Crystal Habit of Gibbsite*", Journal of Crystal Growth, **1999**, *196*, 174-180.

Seyssiecq, I., S. Veesler, R., Boistelle, and J.M., Lamérant, "*Agglomeration of Gibbsite* $Al(OH)_3$ *Crystals in Bayer Liquors. Influence of the Process Parameters*", Chemical Engineering Science, **1998**, *53 (12)*, 2177-2185.

Singh, B. P., L., Besra and A. R., Prasad, *"Role of Surface Effects in Improved Dewatering of Alumina Trihydrate"*, Mineral Processing and Extractive Metallurgy, **1999**, *108 (January- April)*, C27- C33.

Söhnel, O. and J., Garside, *Precipitation: Basic Principles and Industrial Applications*, Butterworth-Heinemann, Boston, **1992**.

Stumpf, H., *"X-ray Diffraction Pattern 12-0460"*, JCPDS- International Centre for Diffraction Data, **1998**.

Varley, P. C., *The Technology of Aluminium and its Alloys*, Newnes-Butterworths, Newnes International Monographs on Materials Science and Technology, London, **1970**.

Veesler, S. and R., Boistelle, *"About Supersaturation and Growth Rates of Hydrargillite $Al(OH)_3$ in Alumina Caustic Solutions"*, Journal of Crystal Growth, **1993**, *130*, 411-415.

Veesler, S., S., Roure and R., Boistelle, *"General Concepts of Hydrargillite $Al(OH)_3$ Agglomeration"*, Journal of Crystal Growth, **1994**, *135*, 505-512.

Vergouw, J. M., A., Difeo, Z., Xu and J. A., Finch, *" An Agglomeration Study of Sulphide Minerals Using Zeta-Potential and Settling Rate. Part II: Sphalerite/Pyrite and Sphalerite/Galena"*, Minerals Engineering, **1998**, *11 (7)*, 605-614.

Warren, H. and L., Armstrong, *"Effect of Process Conditions and Liquor Quality on Yield and Soda Impurity in Aluminium Hydroxide Crystallisation"*, 6th AusIMM extractive metallurgy conference, Brisban, **1994**, *July*, 3-6.

Weiss, N. L., *SME Mineral Processing Handbook*, Society of Mining Engineers of the American Institute of Mining, Metallurgical and Petroleum Engineers, Inc, New York, **1995**.

Yamada, K., T., Harato and H., Kato, *"Process for Producing Coarse Grains of Aluminum Hydroxide"*, U.S. Patent No. 4,311,486, **1982**, *January 19*.

Zaknich, A., *"Characterisation of Aluminium Hydroxide Particles from the Bayer Process Using Neural Network and Bayesian Classifiers"*, IEEE Transactions on neural networks, **1997**, *8 (4)*, 919-931.

Zettlemoyer, A. C., *Nucleation*, Dekker, M., New York, **1969**.

# APPENDIX A

# CALCULATIONS

From the AA analysis, we obtained a concentration X of [$Na^+$] in (g/L) and a concentration Y of [$Al^{3+}$] in (g/L). In the aluminum industry, the aluminum, $Al(OH)_3$ and NaOH concentrations are replaced by $Al_2O_3$ and $Na_2O$ concentrations (Veesler and Boistelle, 1994).

Following is defined the respective equivalent concentration of sodium hydroxide [Na(OH)], [$Na_2O$], and [$Al_2O_3$] :

- $$[\mathrm{NaOH}] = \left( \frac{X \dfrac{\mathrm{g}_{\mathrm{Na}^+}}{\mathrm{L}}}{23 \dfrac{\mathrm{g}_{\mathrm{Na}^+}}{\mathrm{mol}_{\mathrm{Na}^+}}} \right) \times \left( \frac{40\mathrm{g}_{\mathrm{NaOH}}}{\mathrm{mol}_{\mathrm{NaOH}}} \right) \times \left( \frac{1\,\mathrm{mol}_{\mathrm{NaOH}}}{1\,\mathrm{mol}_{\mathrm{Na}^+}} \right)$$

$$\boxed{[\mathrm{NaOH}] = \left( \frac{X}{23} \right) \times 40 \times \left( \frac{\mathrm{g}_{\mathrm{NaOH}}}{\mathrm{L}} \right)} \quad (1)$$

- $$[\mathrm{Na_2O}] = \left( \frac{X \dfrac{\mathrm{g}_{\mathrm{Na}^+}}{\mathrm{L}}}{23 \dfrac{\mathrm{g}_{\mathrm{Na}^+}}{\mathrm{mol}_{\mathrm{Na}^+}}} \right) \times \left( \frac{62\mathrm{g}_{\mathrm{Na_2O}}}{\mathrm{mol}_{\mathrm{Na_2O}}} \right) \times \left( \frac{1\,\mathrm{mol}_{\mathrm{Na_2O}}}{2\,\mathrm{mol}_{\mathrm{Na}^+}} \right)$$

$$\boxed{[\mathrm{Na_2O}] = \left( \frac{X}{23} \right) \times \left( \frac{62}{2} \right) \times \left( \frac{\mathrm{g}_{\mathrm{Na_2O}}}{\mathrm{L}} \right)} \quad (2)$$

- $$\left[Al_2O_3\right] = \left( \frac{Y \frac{g_{Al^{3+}}}{L}}{27 \frac{g_{Al^{3+}}}{mol_{Al^{3+}}}} \right) \times \left( \frac{102g_{Al_2O_3}}{mol_{Al_2O_3}} \right) \times \left( \frac{1\,mol_{Al_2O_3}}{2\,mol_{Al^{3+}}} \right)$$

$$\boxed{\left[Al_2O_3\right] = \left(\frac{Y}{27}\right) \times \frac{102}{2} \times \left(\frac{g_{Al_2O_3}}{L}\right)} \quad (3)$$

# APPENDIX B

# MASS BALANCE

It is assumed in these equations that the volume of the reactor was constant and that the evaporation rate was linear. The sodium introduced in the caustic solution was inert, i.e., it did not take part in the reaction. The dissolution of sodium in the crystal was negligible (X-ray analysis). Thus the sodium concentration was assumed to be constant throughout the process. However, due to the evaporation at the given temperature, the concentration of sodium increased as a function of time (Figure B1). The condensate of the water evaporated was taken for an AA analysis, and showed the same reading as distilled water (blank).

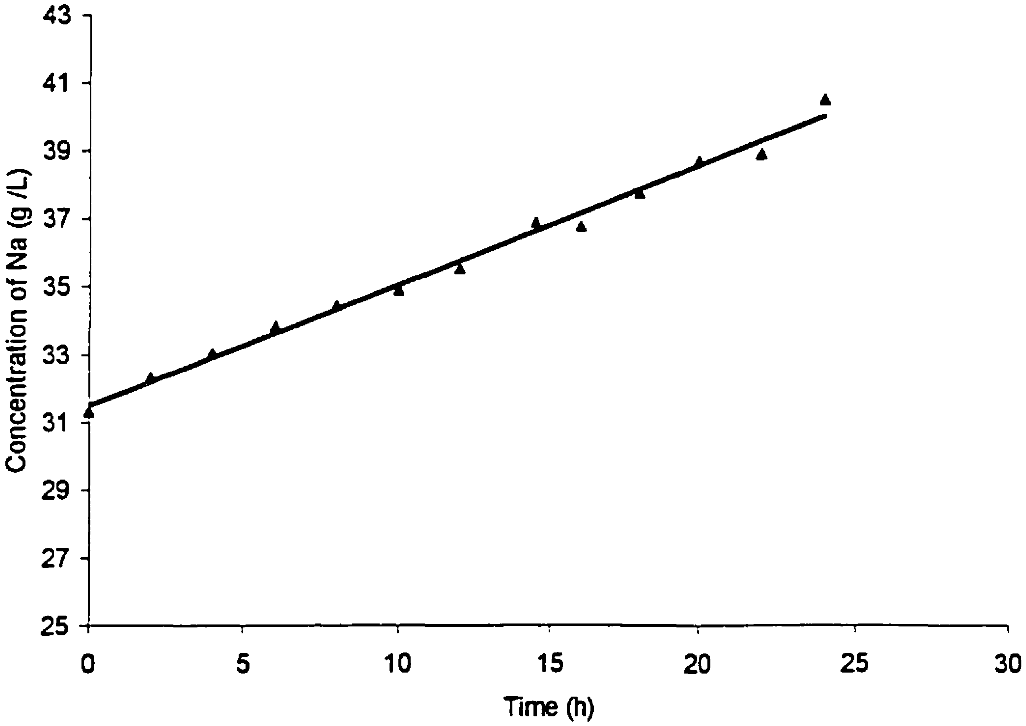

**Figure B1:** Effect of a non controlled evaporation on the sodium concentration for a minimal temperature of 45°C (initial A/C ratio 0.7, and an evaporation of 20% of the total volume)

In order to minimize the evaporation, the top of the reactor was sealed. However, the evaporation of water was still observed. Thus, the change in the liquid volume was measured periodically by noting the liquid level using a buoy. With and without the seal, the change in the liquid volume was measured to be approximately 15% and 45% respectively. These values varied slightly depending on the reactor temperature. Due to this evaporation effect, the aluminum concentration and the concentration of particle increased. Thus, a sodium mass balance was performed. The aluminum concentration measured by AA and the concentration of particle were corrected accordingly (Figure B2). The equations used in the calculations are shown as below.

- At the initial time $t = t_0$, the initial amount of sodium is:

$$m_{Na0} = V_0 \times C_0$$

- At $t = t_1$, $V_1$ is the volume after the first sampling of a volume $\Delta V_1$. Assuming that the concentration of Na is constant:

$$m_{Na0} = V_0 \times C_0 = m_{Na1} = (V_1 + \Delta V_1) \times C_1$$

$$\Longrightarrow \boxed{V_1 = \frac{V_0 C_0}{C_1} - \Delta V_1} \quad (1)$$

The evaporation can be estimated from this equation (1) knowing that:

$$V_{1evap} = V_0 - \left(V_1 + \Delta V_1\right)$$

$$V_{1evap} = V_0 - \left(\frac{V_0 C_0}{C_1}\right)$$

$$\Longrightarrow \boxed{V_{1evap} = V_0\left(1 - \frac{C_0}{C_1}\right)} \quad (2)$$

- At t = $t_2$ for the second sampling of a volume $\Delta V_2$, following the same procedure:

$$m_{Na1} = V_1 \times C_1 = m_{Na2} = (V_2 + \Delta V_2) \times C_2$$

$$\text{and } V_{2evap} = V_0 - (V_2 + \Delta V_2)$$

The new volumes are:

$$\Longrightarrow \boxed{V_2 = \frac{V_1 C_1}{C_2} - \Delta V_2} \quad (3)$$

$$\Longrightarrow \boxed{V_{2evap} = V_0\left(1 - \frac{C_0}{C_2}\right) + \Delta V_1 \frac{C_1}{C_2}} \quad (4)$$

From the calculation of these theoretical volumes, the theoretical amount of aluminum noted N can be deduced:

$$\text{At the time } t = t_1 \quad N = V_1 \times C_{Al}$$

Using the equation (1) and the real concentration of aluminum analyzed by the AA:

$$N = C_{Al1} \times V_1 = \left(\frac{V_0 C_0}{C_1} - \Delta V_1\right) \times C_{Al1}$$

$$C_{Al1}\text{corrected} = \frac{N}{V_0 - \Delta V_1} = \left(\frac{V_0 C_0}{C_1} - \Delta V_1\right) \times \frac{C_{Al1}}{V_0 - \Delta V_1}$$

with $V_0 = 1L$

$$\Longrightarrow \boxed{C_{Al1}\text{corrected} = \frac{N}{1 - \Delta V_1} = \frac{C_{Al1} \times V_1}{1 - \Delta V_1} = \left(\frac{C_0}{C_1} - \Delta V_1\right) \times \frac{C_{Al1}}{1 - \Delta V_1}} \quad (5)$$

In the equation of the corrected aluminum concentration (equation 5), $V_0 - \Delta V_1$ represents the volume without evaporation. The volume in the reactor decreases only due to the sampling.

For the other time n, the volume $V_n$ and the concentration $C_n$ are calculated in the same way following the equations 6 and 7. An example of correction of the evaporation is shown below (Figure B2).

$$\Longrightarrow \boxed{V_n = \frac{V_{n-1} C_{Na(n-1)}}{C_{Na(n)}} - \Delta V_n} \quad (6)$$

$$\Longrightarrow \boxed{C_{Aln}\text{corrected} = \frac{N}{1 - \Delta V_{total}} = \left(\frac{V_{n-1} C_{Na(n-1)}}{C_{Na(n)}} - \Delta V_n\right) \times \frac{C_{Aln}}{1 - \Delta V_{total}}} \quad (7)$$

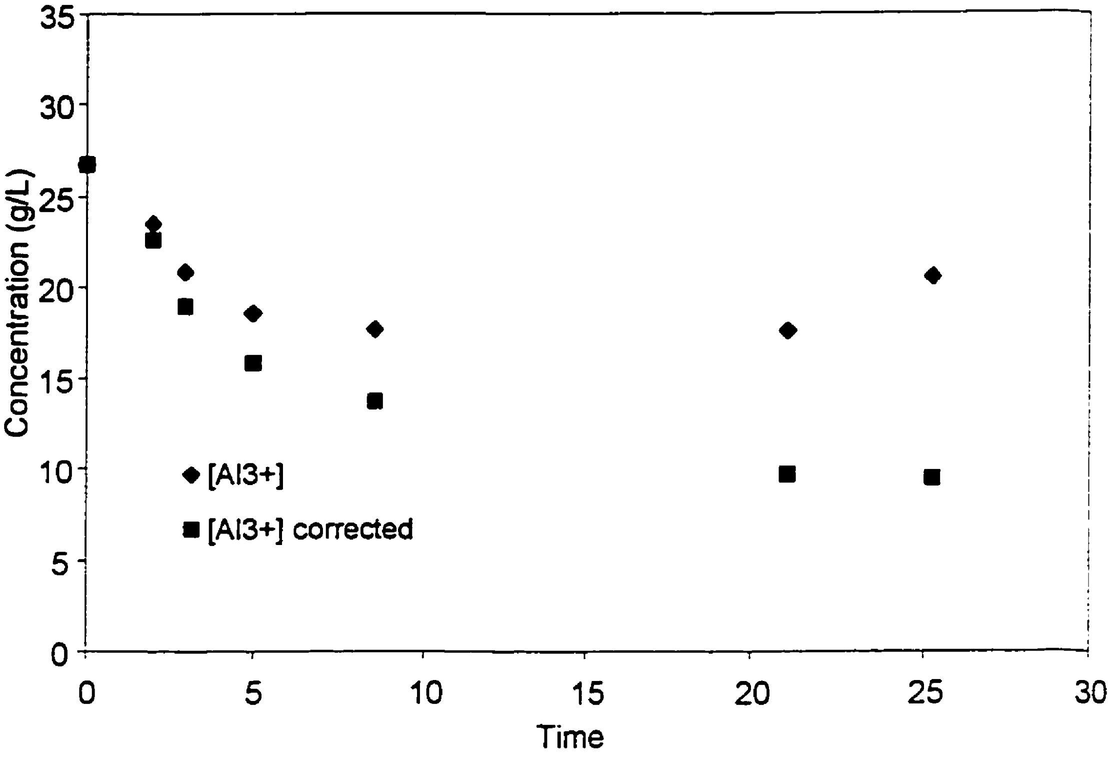

**Figure B2:** Compensation of the evaporation effect on the concentration of aluminum and sodium. (temperature 60°C, initial A/C ratio 1.3, and a theoretical evaporation of 45% of the total volume).

The slurry density is also affected by the evaporation (Figure B3). Following the same procedure, the evaporation is compensated using the theoretical volume defined in equation 6:

$$\boxed{C_{\text{Particle n}}\ \text{corrected} = C_{\text{Particle n}} \times \frac{V_n}{V_0 - \Delta V_{\text{total n}}}} \quad (8)$$

With $\Delta V_{\text{total n}}$ corresponding to the cumulated sampling volume from the beginning of the experiment to the time n.

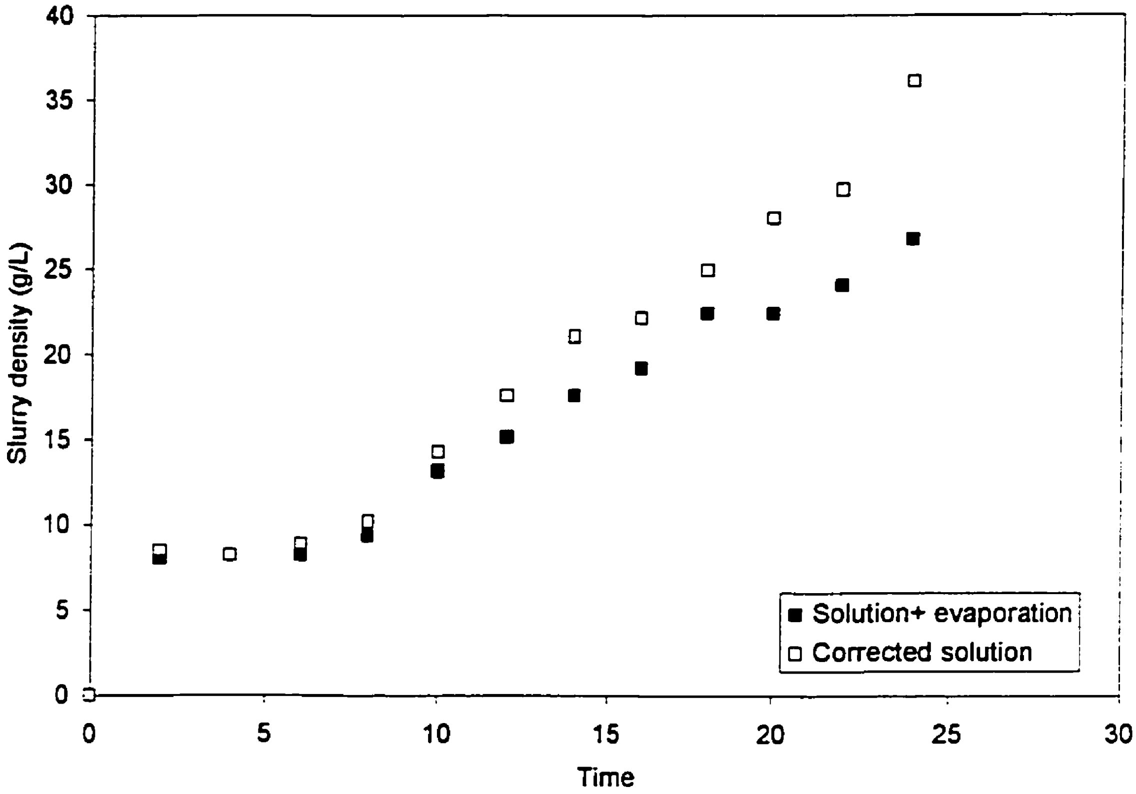

**Figure B3:** Compensation of the evaporation effect on the particle concentration (temperature 60°C, initial A/C ratio 1.3, and an evaporation of 13% of the total volume).

# APPENDIX C

## X-RAY PATTERNS

33-0018 Wavelength= 1.54060 i

**Al(OH)3**

**Aluminum Hydroxide**

**Gibbsite, syn**

Rad.: CuKa1λ: 1.54060 Filter: d-sp: Diff.

Cut off: Int.: Diffract. I/Icor.: 1.0

Ref: Cisar, A., Poulsen, K., Dow Chemical Company, Freeport, TX, USA, ICDD Grant-in-Aid, (1979)

---

Sys.: Monoclinic S.G.: $P2_1/n$ (14)

a: 8.6552 b: 5.0722 c: 9.7161 A: 1.7064 C: 1.9156

α: β: 94.607 γ: Z: 8 mp:

Ref: Ibid.

Dx: 2.437 Dm: 2.400 SS/FOM: $F_{30}$ = 10(0.025, 113 )

---

εα: 1.577 ηωβ: 1.577 εγ: 1.595 Sign: 2V: C

Ref: Dana's System of Mineralogy, 7th Ed., I, 663 (1944)

---

Color: White
Sample of reagent grade chemical from Matheson, Coleman, and Bell. Optical data on artificial material; measured density on crystals. C.D. Cell: a=9.716, b=5.072, c=8.655, β=94.61, a/b=1.9156, c/b=1.7064, S.G.=P21/n(14). Silicon used as an internal stand. PSC: mP56. To replace 1-263, 1-264, 1-265, 1-266, 7-324 and 12-460 and validated by calculated pattern 29-41. Mwt: 78.00. Volume[CD]: 425.17.

| 2θ | Int | h | k | l |
|---|---|---|---|---|
| 18.283 | 100 | 0 | 0 | 2 |
| 20.30 | 70 | 1 | 1 | 0 |
| 20.549 | 50 | 2 | 0 | 0 |
| 26.515 | 17 | 2 | 0 | $\bar{2}$ |
| 26.896 | 30 | 1 | 1 | $\bar{2}$ |
| 28.011 | 25 | 1 | 1 | 2 |
| 28.725 | 13 | 1 | 0 | $\bar{3}$ |
| 36.407 | 25 | 3 | 1 | $\bar{1}$ |
| 36.616 | 40 | 0 | 2 | 1 |
| 37.083 | 15 | 0 | 0 | 4 |
| 37.684 | 55 | 3 | 1 | 1 |
| 38.318 | 4 | 1 | 2 | 1 |
| 39.314 | 15 | 3 | 1 | $\bar{2}$ |
| 40.108 | 20 | 0 | 2 | 2 |
| 41.140 | 2 | 1 | 2 | $\bar{2}$ |
| 41.691 | 27 | 3 | 1 | 2 |
| 43.374 | 4 | 1 | 1 | 4 |
| 44.167 | 40 | 3 | 1 | $\bar{3}$ |
| 44.754 | 3 | 2 | 2 | $\bar{2}$ |
| 45.440 | 28 | 0 | 2 | 3 |
| 46.192 | 6 | 1 | 2 | $\bar{3}$ |
| 46.192 | 6 | 2 | 2 | 2 |
| 47.306 | 15 | 1 | 2 | 3 |
| 50.548 | 30 | 3 | 2 | $\bar{2}$ |
| 52.175 | 30 | 0 | 2 | 4 |
| 52.667 | 4 | 1 | 2 | $\bar{4}$ |
| 53.977 | 4 | 1 | 2 | 4 |
| 54.424 | 30 | 3 | 1 | 4 |
| 55.383 | 9 | 1 | 3 | 0 |
| 55.383 | 9 | 2 | 2 | $\bar{4}$ |
| 57.851 | 7 | 4 | 1 | $\bar{4}$ |
| 58.095 | 7 | 3 | 1 | $\bar{5}$ |
| 58.605 | 8 | 5 | 0 | $\bar{3}$ |
| 58.605 | 8 | 2 | 3 | 0 |
| 59.494 | 3 | 2 | 0 | $\bar{6}$ |
| 62.512 | 4 | 2 | 1 | $\bar{6}$ |
| 62.512 | 4 | 2 | 3 | 2 |
| 63.800 | 30 | 3 | 2 | 4 |
| 63.800 | 30 | 3 | 3 | 0 |
| 64.653 | 18 | 4 | 1 | 5 |
| 66.149 | 19 | 3 | 3 | $\bar{2}$ |
| 66.650 | 13 | 3 | 1 | $\bar{6}$ |
| 67.817 | 6 | 3 | 3 | 2 |
| 68.883 | 10 | 0 | 2 | $\bar{6}$ |
| 70.718 | 7 | 1 | 2 | 6 |
| 71.111 | 4 | 2 | 2 | $\bar{6}$ |
| 72.681 | 3 | 4 | 1 | $\bar{6}$ |
| 77.430 | 3 | 6 | 2 | $\bar{2}$ |
| 77.797 | 2 | 3 | 3 | 4 |
| 78.613 | 6 | 4 | 2 | 5 |
| 78.613 | 6 | 2 | 4 | 0 |
| 78.954 | 7 | 1 | 4 | 2 |
| 81.581 | 4 | 1 | 1 | $\bar{8}$ |
| 84.541 | 4 | 6 | 2 | $\bar{4}$ |
| 89.589 | 3 | 4 | 4 | 0 |
| 90.719 | 4 | 6 | 3 | $\bar{2}$ |

PCPDFWIN v. 2.01

12-0460 Wavelength= 1.5418

α-$Al(OH)_3$

**Aluminum Hydroxide**

**Gibbsite, syn**

Rad.: CuKa λ: 1.5418 Filter: Ni Beta d-sp: Diff.

Cut off: Int.: Diffract. I/Icor.:

Ref: Stumpf, H., Research Labs., Aluminum Co. of America, New Kensington, Pennsylvania, USA, Private Communication

Sys.: Monoclinic S.G.: $P2_1/c$ (14)

a: 8.641 b: 5.070 c: 9.719 A: 1.7043 C: 1.9170

α: β: 94.58 γ: Z: 8 mp:

Ref: Z. Kristallogr., Kristallgeom., Kristallphys., Kristallchem., 87, 185 (1934)

Dx: 2.441 Dm: SS/FOM: $F_{25}$ = 3:(0.080, 121 )

Sample precipitated from hot sodium aluminate solutions; contains up to 0.3% Na2 O. C.D. Cell: a=9.719, b=5.070, c=8.641, β=94.58, a/b=1.9170, c/b=1.7043, S.G.=P21/a(14). PSC: mP56. To replace 1-263, 1-264, 1-265 and 1-266. Deleted by 33-18. Mwt: 78.00. Volume[CD]: 424.43.

| 2θ | Int | h | k | l |
|---|---|---|---|---|
| 18.407 | 100 | 0 | 0 | 2 |
| 20.463 | 40 | 1 | 1 | 0 |
| 20.656 | 20 | 2 | 0 | 0 |
| 26.608 | 10 | $\bar{2}$ | 0 | 2 |
| 26.936 | 6 | $\bar{1}$ | 1 | 2 |
| 28.149 | 8 | $\bar{2}$ | 1 | 1 |
| 28.990 | 4 | 2 | 0 | 2 |
| 36.835 | 16 | 1 | 2 | 0 |
| 37.151 | 4 | 0 | 0 | 4 |
| 37.964 | 20 | $\bar{1}$ | 2 | 1 |
| 39.524 | 4 | 1 | 0 | 4 |
| 40.448 | 6 | 2 | 1 | 3 |
| 42.023 | 8 | $\bar{2}$ | 2 | 1 |
| 44.637 | 12 | $\bar{4}$ | 0 | 2 |
| 45.827 | 10 | 4 | 1 | 0 |
| 46.574 | 2 | 2 | 2 | 2 |
| 47.875 | 8 | $\bar{3}$ | 2 | 0 |
| 51.020 | 10 | 4 | 1 | 2 |
| 52.597 | 10 | 3 | 2 | 2 |
| 54.983 | 10 | $\bar{5}$ | 0 | 2 |
| 55.707 | 4 | $\bar{2}$ | 2 | 4 |
| 56.451 | 2 | 1 | 3 | 1 |
| 58.407 | 4 | $\bar{5}$ | 1 | 2 |
| 58.815 | 2 | 2 | 3 | 0 |
| 59.650 | 2 | 4 | 0 | 4 |

29-0041 Wavelength= 1.54050 C

---

$Al(OH)_3$

**Aluminum Hydroxide**

**Gibbsite**

---

Rad.: CuKa1λ: 1.54050 Filter: d-sp: Calculated

Cut off: Int.: Calculated I/Icor.: 1.58

Ref: Smith, D., Fausey, Penn State University, University Park, Pennsylvania, USA, ICDD Grant-in-Aid, (1977)

---

Sys.: Monoclinic S.G.: $P2_1/n$ (14)

a: 8.684 b: 5.078 c: 9.736 A: 1.7101 C: 1.9173

α: β: 94.54 γ: Z: 8 mp:

Ref: Saalfeld, H., Wedde, Z. Kristallogr., Kristallgeom., Kristallphys., Kristallchem., 139, 129 (1974)

Dx: 2.421 Dm: SS/FOM: $F_{30}$ = 87 (.0031 , 112 )

---

Peak height intensity. Specimen from Langesundfjord, Norway. C.D. Cell: a=9.736, b=5.078, c=8.684, β=94.54, a/b=1.9173, c/b=1.7101, S.G.=P21/n(14). PSC: mP56. Deleted by 33-18, calculated confirms experimental, MTG 5/92. Mwt: 78.00. Volume[CD]: 427.98.

| 2θ | Int | h | k | l |
|---|---|---|---|---|
| 18.265 | 100 | 0 | 0 | 2 |
| 20.257 | 36 | 1 | 1 | 0 |
| 20.503 | 18 | 2 | 0 | 0 |
| 26.465 | 5 | $\bar{2}$ | 0 | 2 |
| 26.847 | 9 | $\bar{1}$ | 1 | 2 |
| 27.954 | 7 | 1 | 1 | 2 |
| 28.679 | 3 | 2 | 0 | 2 |
| 36.325 | 7 | $\bar{3}$ | 1 | 1 |
| 36.555 | 12 | 0 | 2 | 1 |
| 37.023 | 4 | 0 | 0 | 4 |
| 37.618 | 16 | 3 | 1 | 1 |
| 39.238 | 4 | $\bar{3}$ | 1 | 2 |
| 40.038 | 6 | 0 | 2 | 2 |
| 40.169 | 4 | $\bar{3}$ | 0 | 3 |
| 41.601 | 7 | 3 | 1 | 2 |
| 41.803 | 5 | $\bar{1}$ | 1 | 4 |
| 44.094 | 12 | $\bar{3}$ | 1 | 3 |
| 44.436 | 8 | $\bar{4}$ | 0 | 2 |
| 45.368 | 8 | 0 | 2 | 3 |
| 45.522 | 6 | 4 | 1 | 0 |
| 46.109 | 2 | 2 | 2 | 2 |
| 47.313 | 5 | 3 | 1 | 3 |
| 50.449 | 10 | $\bar{3}$ | 1 | 4 |
| 50.774 | 6 | 4 | 1 | 2 |
| 52.092 | 9 | 0 | 2 | 4 |
| 54.330 | 7 | 3 | 1 | 4 |

| 2θ | Int | h | k | l |
|---|---|---|---|---|
| 54.487 | 5 | $\bar{4}$ | 0 | 4 |
| 55.324 | 2 | $\bar{2}$ | 2 | 4 |
| 57.780 | 2 | 2 | 2 | 4 |
| 57.987 | 2 | $\bar{5}$ | 1 | 2 |
| 58.499 | 2 | 2 | 3 | 0 |
| 63.683 | 5 | $\bar{3}$ | 3 | 0 |
| 64.533 | 3 | 6 | 0 | 0 |
| 66.023 | 4 | $\bar{3}$ | 3 | 2 |
| 66.341 | 2 | $\bar{5}$ | 1 | 4 |
| 66.533 | 4 | $\bar{3}$ | 1 | 6 |
| 66.915 | 2 | $\bar{5}$ | 2 | 2 |
| 68.746 | 2 | 0 | 2 | 6 |
| 68.930 | 2 | 1 | 3 | 4 |

---

07-0324 Wavelength= 1.5418 i

$Al(OH)_3$

Aluminum Hydroxide

Gibbsite

Rad.: CuKa λ: 1.5418 Filter: Ni Beta d-sp:

Cut off: Int.: Diffract. I/Icor.:

Ref: Gillery, Min. Ind., Penn State University, University Park, Pennsylvania, USA, Private Communication

Sys.: Monoclinic S.G.: $P2_1/n$ (14)

a: 8.659 b: 5.077 c: 9.703 A: 1.7055 C: 1.9112

α: β: 94.2 γ: Z: 8 mp:

Ref: Ibid.

Dx: 2.436 Dm: 2.400 SS/FOM: $F_{30}$ = 7:(0.031, 146 )

εα: 1.568 ηωβ: 1.568 εγ: 1.587 Sign:+ 2V: C

Ref: Dana's System of Mineralogy, 7th Ed.

Color: Colorless
Specimen from Cheener mine, Richmond, Massachusettes, USA. C.D. Cell: a=9.703, b=5.077, c=8.659, β=94.20, a/b=1.9112, c/b=1.7055, S.G.=P21/n(14). PSC: mP56. To replace 1-263, 1-264, 1-265 and 1-266. Deleted by 33-18, lower FN, MTG 5/92. Mwt: 78.00. Volume[CD]: 425.42.

| 2θ | Int | h | k | l |
|---|---|---|---|---|
| 18.292 | 100 | 0 | 0 | 2 |
| 20.321 | 16 | 1 | 1 | 0 |
| 20.559 | 8 | 2 | 0 | 0 |
| 26.969 | 5 | $\bar{1}$ | 1 | 2 |
| 27.996 | 4 | 1 | 1 | 2 |
| 28.685 | 3 | 2 | 0 | 2 |
| 36.618 | 8 | 0 | 2 | 1 |
| 37.151 | 6 | 0 | 0 | 4 |
| 37.667 | 8 | 3 | 1 | 1 |
| 39.434 | 2 | $\bar{3}$ | 1 | 2 |
| 40.185 | 3 | 2 | 1 | 3 |
| 41.658 | 3 | 3 | 1 | 2 |
| 43.399 | 1 | 1 | 1 | 4 |
| 44.338 | 6 | $\bar{3}$ | 1 | 3 |
| 45.512 | 4 | 0 | 2 | 3 |
| 46.322 | 1 | $\bar{1}$ | 2 | 3 |
| 47.319 | 4 | 4 | 1 | 1 |
| 50.747 | 4 | $\bar{3}$ | 1 | 4 |
| 52.273 | 5 | 0 | 2 | 4 |
| 54.313 | 4 | 3 | 1 | 4 |
| 55.561 | 1 | $\bar{2}$ | 2 | 4 |
| 56.151 | 1 | $\bar{4}$ | 2 | 1 |
| 57.885 | 1 | 2 | 2 | 4 |
| 58.245 | 1 | $\bar{4}$ | 2 | 2 |
| 58.692 | 1 | $\bar{5}$ | 0 | 3 |
| 59.439 | 1 | 4 | 0 | 4 |
| 59.608 | 1 | 2 | 3 | 1 |
| 62.500 | 1 | 3 | 1 | 5 |
| 62.924 | 1 | $\bar{2}$ | 2 | 5 |
| 63.889 | 3 | 3 | 3 | 0 |
| 64.685 | 2 | 6 | 0 | 0 |
| 66.340 | 2 | $\bar{6}$ | 0 | 2 |
| 66.930 | 2 | $\bar{3}$ | 1 | 6 |
| 67.921 | 1 | $\bar{1}$ | 0 | 7 |
| 69.002 | 1 | 0 | 2 | 6 |
| 70.241 | 1 | $\bar{4}$ | 0 | 6 |
| 70.848 | 1 | $\bar{4}$ | 3 | 0 |
| 71.467 | 1 | 3 | 1 | 6 |
| 76.443 | 1 | $\bar{1}$ | 4 | 1 |
| 78.841 | 1 | 0 | 2 | 7 |

$Al(OH)_3$

Aluminum Hydroxide

Bayerite, syn

Rad.: CuKa λ: 1.5418 Filter: Ni Beta d-sp:

Cut off: Int.: Diffract. I/Icor.:

Ref: Rothbauer, Zigan, O'Daniel, Z. Kristallogr., Kristallgeom., Kristallphys., Kristallchem., 125, 317 (1967)

Sys.: Monoclinic S.G.: $P2_1/a$ (14)

a: 5.062 b: 8.671 c: 4.713 A: 0.5838 C: 0.5435

α: β: 90.27 γ: Z: 4 mp:

Ref: Ibid.

Dx: 2.505 Dm: SS/FOM: $F_{30}$ = 29 (0.022, 46 )

Color: White
Synthetic. Reflections calculated from cell dimensions, averaged for reflections with multiple indices (hkl). PSC: mP28. To replace 15-136. Plus 16 additional reflections to 1.084. Mwt: 78.00. Volume[CD]: 206.86.

| 2θ | Int | h | k | l | 2θ | Int | h | k | l |
|---|---|---|---|---|---|---|---|---|---|
| 18.840 | 90 | 0 | 0 | 1 | 51.796 | 2 | 2 | 3 | 1 |
| 20.416 | 70 | 0 | 2 | 0 | 53.156 | 40 | 2 | 0 | 2 |
| 21.463 | 2 | 0 | 1 | 1 | 54.105 | 2 | $\bar{2}$ | 1 | 2 |
| 27.103 | 2 | $\bar{1}$ | 2 | 0 | 54.348 | 2 | 2 | 1 | 2 |
| 27.880 | 30 | 1 | 1 | 1 | 55.488 | 2 | 3 | 1 | 0 |
| 33.192 | 4 | 1 | 2 | 1 | 55.854 | 2 | $\bar{2}$ | 4 | 0 |
| 35.466 | 2 | 2 | 0 | 0 | 56.039 | 2 | 1 | 5 | 0 |
| 35.773 | 2 | 1 | 3 | 0 | 56.527 | 2 | 0 | 5 | 1 |
| 36.464 | 2 | 0 | 3 | 1 | 57.608 | 10 | 2 | 2 | 2 |
| 36.993 | 2 | $\bar{2}$ | 1 | 0 | 58.733 | 2 | 3 | 2 | 0 |
| 38.199 | 4 | 0 | 0 | 2 | 59.481 | 8 | 2 | 4 | 1 |
| 39.633 | 2 | 0 | 1 | 2 | 60.818 | 2 | $\bar{1}$ | 4 | 2 |
| 40.601 | 100 | 2 | 0 | 1 | 60.951 | 2 | 1 | 4 | 2 |
| 41.299 | 2 | 2 | 2 | 0 | 62.221 | 2 | $\bar{3}$ | 2 | 1 |
| 41.658 | 2 | 0 | 4 | 0 | 62.594 | 2 | $\bar{2}$ | 3 | 2 |
| 41.739 | 2 | $\bar{2}$ | 1 | 1 | 62.877 | 2 | 2 | 3 | 2 |
| 41.901 | 2 | 2 | 1 | 1 | 63.889 | 12 | 3 | 3 | 0 |
| 43.663 | 2 | 1 | 1 | 2 | 64.484 | 8 | 0 | 6 | 0 |
| 45.512 | 2 | $\bar{1}$ | 4 | 0 | 65.192 | 2 | 2 | 5 | 0 |
| 45.754 | 4 | $\bar{2}$ | 2 | 1 | 65.761 | 2 | $\bar{1}$ | 2 | 3 |
| 46.098 | 2 | 0 | 4 | 1 | 65.970 | 2 | 1 | 2 | 3 |
| 47.424 | 2 | $\bar{1}$ | 2 | 2 | 66.985 | 2 | 0 | 5 | 2 |
| 47.768 | 2 | $\bar{2}$ | 3 | 0 | 67.257 | 6 | 3 | 3 | 1 |
| 49.683 | 2 | 1 | 4 | 1 | 67.865 | 2 | 0 | 6 | 1 |
| 49.945 | 2 | 0 | 3 | 2 | 68.486 | 2 | $\bar{2}$ | 5 | 1 |

| 2θ | Int | h | k | l |
|---|---|---|---|---|
| 68.600 | 2 | 2 | 5 | 1 |
| 69.176 | 2 | $\bar{3}$ | 1 | 2 |
| 69.763 | 2 | 2 | 4 | 2 |
| 70.665 | 18 | $\bar{1}$ | 3 | 3 |
| 71.467 | 2 | $\bar{2}$ | 1 | 3 |
| 72.034 | 2 | $\bar{3}$ | 2 | 2 |
| 72.417 | 2 | 3 | 2 | 2 |
| 74.268 | 2 | $\bar{2}$ | 2 | 3 |
| 75.093 | 2 | 4 | 0 | 0 |
| 75.868 | 2 | 2 | 6 | 0 |
| 76.733 | 2 | $\bar{3}$ | 3 | 2 |
| 77.101 | 2 | 3 | 3 | 2 |
| 77.249 | 2 | $\bar{1}$ | 4 | 3 |
| 77.397 | 2 | 1 | 4 | 3 |
| 77.472 | 2 | 0 | 6 | 2 |
| 78.150 | 2 | $\bar{4}$ | 0 | 1 |
| 78.997 | 8 | 2 | 6 | 1 |
| 80.025 | 2 | 0 | 7 | 1 |
| 82.430 | 6 | 3 | 5 | 1 |
| 83.211 | 2 | $\bar{3}$ | 4 | 2 |
| 83.387 | 2 | 4 | 3 | 0 |
| 83.563 | 2 | 3 | 4 | 2 |
| 85.377 | 2 | 0 | 2 | 4 |
| 86.319 | 2 | $\bar{4}$ | 3 | 1 |
| 86.510 | 2 | 4 | 3 | 1 |

PCPDFWIN v. 2.01

21-1276 Wavelength= 1.54056 •

**TiO2**

Titanium Oxide

Rutile, syn

Rad.: CuKa1λ: 1.54056 Filter: Mono d-sp:

Cut off: Int.: Diffract. I/Icor.: 3.40

Ref: Natl. Bur. Stand. (U.S.) Monogr. 25, 7, 83 (1969)

---

Sys.: Tetragonal S.G.: P4$_2$/mnm (136)

a: 4.5933 b: c: 2.9592 A: C: 0.6442

α: β: γ: Z: 2 mp:

Ref: Ibid.

Dx: 4.250 Dm: 4.230 SS/FOM: $F_{30}$ = 107(.0088 , 32 )

---

εα: 2.9467 ηωβ: 2.6505 εγ: Sign:+ 2V:

Ref: Dana's System of Mineralogy, 7th Ed., I, 575

---

Color: White
Pattern taken at 25 C. Sample obtained from National Lead Co., South Amboy, NJ, USA. No impurity over 0.001%. Two other polymorphs, anatase (tetragonal) and brookite (orthorhombic), converted to rutile on heating above 700 C. Optical data on specimen from Dana's System of Mineralogy, 7th Ed., I 555. Opaque mineral optical data on specimen from Sweden: R3R%=20.3, Disp.=Std., VHN100=1132-1187, Ref.: IMA Commission on Ore Microscopy QDF. Pattern reviewed by Syvinski, W., McCarthy, G., North Dakota State Univ, Fargo, ND, USA, ICDD Grant-in-Aid (1990). Agrees well with experimental and calculated patterns. Additional weak reflections [indicated by brackets] were observed. Naturally occurring material may be reddish brown. O2 Ti type. Rutile group, rutile subgroup. Also called: titania.Tungsten used as an internal stand. PSC: tP6. Validated by calculated pattern. Mwt: 79.90. Volume[CD]: 62.43.

| 2θ | Int | h | k | l |
|---|---|---|---|---|
| 27.446 | 100 | 1 | 1 | 0 |
| 36.085 | 50 | 1 | 0 | 1 |
| 39.187 | 8 | 2 | 0 | 0 |
| 41.225 | 25 | 1 | 1 | 1 |
| 44.050 | 10 | 2 | 1 | 0 |
| 54.322 | 60 | 2 | 1 | 1 |
| 56.640 | 20 | 2 | 2 | 0 |
| 62.740 | 10 | 0 | 0 | 2 |
| 64.038 | 10 | 3 | 1 | 0 |
| 65.478 | 2 | 2 | 2 | 1 |
| 69.008 | 20 | 3 | 0 | 1 |
| 69.788 | 12 | 1 | 1 | 2 |
| 72.408 | 2 | 3 | 1 | 1 |
| 74.409 | 1 | [ 3 | 2 | 0 ] |
| 76.508 | 4 | 2 | 0 | 2 |
| 79.819 | 2 | 2 | 1 | 2 |
| 82.333 | 6 | 3 | 2 | 1 |
| 84.258 | 4 | 4 | 0 | 0 |
| 87.461 | 2 | 4 | 1 | 0 |
| 89.555 | 8 | 2 | 2 | 2 |
| 90.705 | 4 | 3 | 3 | 0 |
| 95.272 | 6 | 4 | 1 | 1 |
| 96.014 | 6 | 3 | 1 | 2 |
| 97.173 | 4 | 4 | 2 | 0 |
| 98.511 | <1 | [ 3 | 3 | 1 ] |
| 105.095 | 2 | 4 | 2 | 1 |
| 106.015 | 2 | 1 | 0 | 3 |
| 109.402 | 2 | 1 | 1 | 3 |
| 116.222 | 4 | 4 | 0 | 2 |
| 117.522 | 4 | 5 | 1 | 0 |
| 120.054 | 8 | 2 | 1 | 3 |
| 122.783 | 8 | 4 | 3 | 1 |
| 123.655 | 8 | 3 | 3 | 2 |
| 131.841 | 6 | 4 | 2 | 2 |
| 136.542 | 8 | 3 | 0 | 3 |
| 140.044 | 12 | 5 | 2 | 1 |
| 143.107 | 2 | 4 | 4 | 0 |
| 155.856 | 2 | 5 | 3 | 0 |

24-0072 Wavelength= 1.54050 C

**Fe2O3**

Iron Oxide

Hematite

Rad.: CuKa1λ: 1.54050 Filter: d-sp: Calculated

Cut off: Int.: Calculated I/Icor.:

Ref: Smith et al., ICDD Grant-in-Aid, (1973)

Sys.: Rhombohedral S.G.: R$\bar{3}$ (148)

a: 5.038 b: c: 13.772 A: C: 2.7336

α: β: γ: Z: 6 mp:

Ref: Ibid.

Dx: 5.256 Dm: SS/FOM: $F_{27}$ = 17 (.0196, 79 )

Integrated intensities. PSC: hR10. Deleted by 33-664. Mwt: 159.69. Volume[CD]: 302.72.

| 2θ | Int | h | k | l |
|---|---|---|---|---|
| 24.124 | 33 | 0 | 1 | 2 |
| 33.113 | 100 | 1 | 0 | 4 |
| 35.610 | 70 | 1 | 1 | 0 |
| 39.221 | 2 | 0 | 0 | 6 |
| 40.833 | 17 | 1 | 1 | 3 |
| 43.470 | 2 | 2 | 0 | 2 |
| 49.414 | 31 | 0 | 2 | 4 |
| 54.001 | 36 | 1 | 1 | 6 |
| 57.504 | 8 | 1 | 2 | 2 |
| 57.504 | 8 | 0 | 1 | 8 |
| 62.381 | 22 | 2 | 1 | 4 |
| 63.962 | 21 | 3 | 0 | 0 |
| 69.496 | 2 | 2 | 0 | 8 |
| 71.818 | 7 | 1 | 0 | 10 |
| 72.167 | 4 | 1 | 1 | 9 |
| 75.404 | 4 | 2 | 2 | 0 |
| 77.656 | 2 | 3 | 0 | 6 |
| 80.607 | 3 | 3 | 1 | 2 |
| 80.607 | 3 | 1 | 2 | 8 |
| 82.820 | 3 | 0 | 2 | 10 |
| 84.863 | 4 | 1 | 3 | 4 |
| 88.464 | 4 | 2 | 2 | 6 |
| 93.546 | 4 | 2 | 1 | 10 |
| 106.533 | 3 | 3 | 2 | 4 |
| 106.773 | 3 | 0 | 1 | 14 |
| 107.997 | 2 | 4 | 1 | 0 |
| 115.851 | 2 | 1 | 3 | 10 |
| 122.299 | 2 | 4 | 1 | 6 |
| 131.498 | 2 | 1 | 2 | 14 |
| 131.498 | 2 | 0 | 5 | 4 |

PCPDFWIN v. 2.01

33-0664 Wavelength= 1.540598

**Fe2O3**

**Iron Oxide**

**Hematite, syn**

Rad.: CuKa1λ: 1.540598Filter: Mono d-sp: Diff.

Cut off: Int.: Diffract. I/Icor.: 2.4

Ref: Natl. Bur. Stand. (U.S.) Monogr. 25, 18, 37 (1981)

---

Sys.: Rhombohedral S.G.: $R\bar{3}c$ (167)

a: 5.0356(1) b: c: 13.7489(7) A: C: 2.7303

α: β: γ: Z: 6 mp: 1350-136(

Ref: Ibid.

Dx: 5.270 Dm: 5.260 SS/FOM: $F_{30}$ = 69 (.0111 , 39 )

---

εα: 2.94 ηωβ: 3.22 εγ: Sign:- 2V:

Ref: Dana's System of Mineralogy, 7th Ed., I, 529 (1944)

---

Color: Dark reddish brown
Pattern taken at 25 C. Sample from Pfizer, Inc., NY, USA, heated at 800 C for 3 days. CAS #: 1309-37-1. Opaque mineral optical data on specimen from Elba, R1R0=30.2, RR2Re=26.1, Disp.=16, VHN=1038 (mean at 100, 200, 300), Color values=1 .299, .309, 29.8, 2 .299, .309, 25.7, Ref.: IMA Commission on Ore Microscopy QDF. Pattern reviewed by Syvinski, W., McCarthy, G., North Dakota State Univ., Fargo, ND, USA, ICDD Grant-in-Aid (1990). Agress well with experimental and calculated patterns. Additional weak reflection [indicated by brackets] was observed. Also called: crocus mantis. Also called: venetian red. Also called: ferrite. Also called: indian red. Also called: crocus. Al2 O3 type. Corundum group, corundum subgroup. Also called: burnt ochre.Also called: rouge.Silver used as an internal stand. PSC: hR10. To replace 13-534 and validated by calculated pattern 24-72. Mwt: 159.69. Volume[CD]: 301.93.

| 2θ | Int | h | k | l |
|---|---|---|---|---|
| 24.138 | 30 | 0 | 1 | 2 |
| 33.153 | 100 | 1 | 0 | 4 |
| 35.612 | 70 | 1 | 1 | 0 |
| 39.277 | 3 | 0 | 0 | 6 |
| 40.855 | 20 | 1 | 1 | 3 |
| 43.519 | 3 | 2 | 0 | 2 |
| 49.480 | 40 | 0 | 2 | 4 |
| 54.091 | 45 | 1 | 1 | 6 |
| 56.152 | 1 | 2 | 1 | 1 |
| 57.429 | 5 | 1 | 2 | 2 |
| 57.590 | 10 | 0 | 1 | 8 |
| 62.451 | 30 | 2 | 1 | 4 |
| 63.991 | 30 | 3 | 0 | 0 |
| 66.028 | <1 | [ 1 | 2 | 5 ] |
| 69.601 | 3 | 2 | 0 | 8 |
| 71.937 | 10 | 1 | 0 | 10 |
| 72.262 | 6 | 1 | 1 | 9 |
| 75.430 | 8 | 2 | 2 | 0 |
| 77.729 | 4 | 3 | 0 | 6 |
| 78.760 | 2 | 2 | 2 | 3 |
| 80.711 | 5 | 1 | 2 | 8 |
| 82.939 | 5 | 0 | 2 | 10 |
| 84.916 | 7 | 1 | 3 | 4 |
| 88.542 | 7 | 2 | 2 | 6 |
| 91.345 | 2 | 0 | 4 | 2 |
| 93.715 | 7 | 2 | 1 | 10 |
| 95.239 | <1 | 1 | 1 | 12 |
| 95.663 | 3 | 4 | 0 | 4 |
| 102.285 | 4 | 3 | 1 | 8 |
| 104.914 | <1 | 2 | 2 | 9 |
| 106.623 | 5 | 3 | 2 | 4 |
| 107.025 | 4 | 0 | 1 | 14 |
| 108.090 | 5 | 4 | 1 | 0 |
| 111.518 | 2 | 4 | 1 | 3 |
| 113.594 | 2 | 0 | 4 | 8 |
| 116.044 | 5 | 1 | 3 | 10 |
| 117.758 | 1 | 3 | 0 | 12 |
| 118.697 | 3 | 2 | 0 | 14 |
| 122.431 | 6 | 4 | 1 | 6 |
| 125.929 | 1 | 2 | 3 | 8 |
| 128.758 | 3 | 4 | 0 | 10 |
| 131.877 | 5 | 1 | 2 | 14 |
| 133.241 | 3 | 3 | 3 | 0 |
| 144.456 | 4 | 3 | 2 | 10 |
| 147.971 | 4 | 2 | 4 | 4 |

Wavelength= 1.54056 C

**Na**

**Sodium**

Rad.: CuKa1λ: 1.54056 Filter: d-sp: Calculated
Cut off: Int.: Calculated I/Icor.:
Ref: Natl. Bur. Stand. (U.S.) Monogr. 25, 9, 105 (1971)

Sys.: Cubic S.G.: Im3m (229)
a: 4.2908(5) b: c: A: C:
α: β: γ: Z: 2 mp:
Ref: Aruja, Perlitz, Z. Kristallogr., Kristallgeom., Kristallphys., Kristallchem., 100, 195 (1939)

Dx: 0.966 Dm: SS/FOM: $F_{11}$ = 143(.0055, 14)

| 2θ | Int | h | k | l |
|---|---|---|---|---|
| 29.420 | 100 | 1 | 1 | 0 |
| 42.080 | 15 | 2 | 0 | 0 |
| 52.180 | 23 | 2 | 1 | 1 |
| 61.021 | 5 | 2 | 2 | 0 |
| 69.183 | 6 | 3 | 1 | 0 |
| 76.902 | 1 | 2 | 2 | 2 |
| 84.402 | 4 | 3 | 2 | 1 |
| 99.224 | 2 | 3 | 3 | 0 |
| 106.795 | 1 | 4 | 2 | 0 |
| 132.515 | 1 | 5 | 1 | 0 |
| 158.999 | 1 | 5 | 2 | 1 |

Peak height intensity. CAS #: 7440-23-5. Published value of a=4.2906(0.0005). PSC: cI2. Mwt: 22.99. Volume[CD]: 79.00.

09-0188 Wavelength= 1.5418

**Na**

**Sodium**

Rad.: CuKa λ: 1.5418 Filter: Ni Beta d-sp:

Cut off: Int.: Diffract. I/Icor.:

Ref: Barrett, Acta Crystallogr., 9, 671 (1956)

Sys.: Hexagonal S.G.: $P6_3/mmc$ (194)

a: 3.767 b: c: 6.154 A: C: 1.6337

α: β: γ: Z: 2 mp:

Ref: Ibid.

Dx: 1.010 Dm: SS/FOM: $F_{12}$ = 7:(0.106, 16 )

CAS #: 7440-23-5. Low temperature structure. Na partially transforms on cooling (below 36 K) or on deforming (below 51 K) to a c.p.h. structure with stacking faults coexisting with body-centered cubic a=4.225. Mg type. PSC: hP2. Mwt: 22.99. Volume[CD]: 75.63.

| 2θ | Int | h | k | l |
|---|---|---|---|---|
| 27.443 | 80 | 1 | 0 | 0 |
| 29.086 | 80 | 0 | 0 | 2 |
| 31.387 | 100 | 1 | 0 | 1 |
| 48.334 | 80 | 1 | 1 | 0 |
| 52.402 | 10 | 1 | 0 | 3 |
| 56.489 | 10 | 2 | 0 | 0 |
| 57.372 | 60 | 1 | 1 | 2 |
| 58.488 | 10 | 2 | 0 | 1 |
| 60.164 | 10 | 0 | 0 | 4 |
| 77.472 | 30 | 2 | 1 | 0 |
| 79.389 | 30 | 2 | 1 | 1 |
| 80.623 | 30 | 1 | 1 | 4 |

05-0565 Wavelength= 1.5405

**Si**

**Silicon**

Silicon, syn [NR]

Rad.: CuKa1λ: 1.5405 Filter: Ni Beta d-sp:

Cut off: Int.: Diffract. I/Icor.: 4.7

Ref: Swanson, Fuyat, Natl. Bur. Stand. (U.S.), Circ. 539, II, 6 (1953)

---

Sys.: Cubic S.G.: Fd3m (227)

a: 5.4301 b: c: A: C:

α: β: γ: Z: 8 mp:

Ref: Ibid.

Dx: 2.330 Dm: SS/FOM: $F_{11}$ = 63(.0135, 13 )

---

Color: Black, gray
X-ray pattern at 26 C. Sample from Johnson Matthey Company. CAS #: 7440-21-3. Spectroscopic analysis: <0.001% Cu, Ag, Zn, Sn, Mg, Fe. C type. PSC: cF8. Deleted by 27-1402, has higher Fn. Mwt: 28.09. Volume[CD]: 160.11.

| 2θ | Int | h | k | l |
|---|---|---|---|---|
| 28.418 | 100 | 1 | 1 | 1 |
| 47.303 | 60 | 2 | 2 | 0 |
| 56.10 | 35 | 3 | 1 | 1 |
| 69.168 | 8 | 4 | 0 | 0 |
| 76.366 | 13 | 3 | 3 | 1 |
| 88.052 | 17 | 4 | 2 | 2 |
| 94.967 | 9 | 5 | 1 | 1 |
| 106.725 | 5 | 4 | 4 | 0 |
| 114.119 | 11 | 5 | 3 | 1 |
| 127.559 | 9 | 6 | 2 | 0 |
| 136.914 | 5 | 5 | 3 | 3 |

---